

# **Modeling the mesoscopic and macroscopic deformation behavior of the ferritic stainless steel DC04**

Zur Erlangung des akademischen Grades  
**Doktor der Ingenieurwissenschaften**

der Fakultät für Maschinenbau

Karlsruher Institut für Technologie (KIT)

genehmigte

**Dissertation**

von

**M.Sc. Tung Phan Van**

Tag der mündlichen Prüfung

Hauptreferent:

Korreferent:

22.02.2012

Prof. Dr.-Ing. Thomas Böhlke

Prof. Dr. rer. nat. Peter Gumbsch

# Contents

<b>Zusammenfassung</b>	<b>4</b>
<b>Summary</b>	<b>5</b>
<b>Acknowledgements</b>	<b>6</b>
<b>1 Introduction</b>	<b>7</b>
List of Frequently Used Symbols . . . . .	10
<b>2 Constitutive Models for Single Crystals and Polycrystals</b>	<b>12</b>
2.1 Large Strain Single Crystal Plasticity Material Model . . . . .	12
2.2 Polycrystal Model . . . . .	15
<b>3 The Crystallite Orientation Distribution Function (CODF)</b>	<b>18</b>
3.1 Basic Properties of the CODF . . . . .	18
3.2 Experimental Identification of the CODF based on Electron Backscatter Diffraction Data (EBSD) . . . . .	20
3.2.1 Cold Formed and Heat Treated Specimens . . . . .	22
3.2.2 EBSD Measurement for Subsequent Tensile Deformations . . . . .	26
3.3 Identification of Texture Components based on EBSD Data . . . . .	31
<b>4 Estimation of Material Parameters</b>	<b>40</b>
4.1 Estimation of Material Parameters based on Tensile Test Experiments . .	40
4.1.1 Experimental Data of Tensile Tests . . . . .	40
4.1.2 FE Modeling and Simulation of Tensile Tests . . . . .	41
4.2 Estimation of Material Parameters based on Micro-pillar Experiments .	47
4.2.1 Micro-pillar Compression Tests . . . . .	47

4.2.2	Experimental Micro-pillar Compression Tests performed in Project A6 . . . . .	48
4.2.3	FE Modeling and Simulation of Micro-pillar Tests . . . . .	49
4.2.4	Estimation of Material Parameters . . . . .	54
<b>5</b>	<b>Simulation of the Deformation Behavior on the Grain Scale</b>	<b>57</b>
5.1	FE-Modeling and Full Field Simulation for EBSD Data . . . . .	57
5.2	Comparison between Grain Scale Simulations and Experiments . . . . .	65
<b>6</b>	<b>Application of the Polycrystal Model for Metal Forming Operation</b>	<b>72</b>
6.1	Deep Drawing Experiment at IFU . . . . .	72
6.2	FE-Modeling and Simulation of Deep Drawing . . . . .	74
6.2.1	Deep Drawing Simulation for a Single Crystal . . . . .	74
6.2.2	Deep Drawing Simulation with Crystal Orientations extracted from EBSD Texture Data . . . . .	79
6.2.3	Deep Drawing Simulation with Texture Components . . . . .	80
<b>7</b>	<b>Texture-based Modeling of Strain Localization</b>	<b>84</b>
7.1	Finite Element Approximation and Localization Criteria . . . . .	84
7.2	Comparison between FE Simulations and Experiments . . . . .	87
<b>8</b>	<b>Summary</b>	<b>90</b>
	<b>Appendix</b>	<b>93</b>
	<b>Bibliography</b>	<b>95</b>
	<b>List of Figures</b>	<b>102</b>
	<b>List of Tables</b>	<b>107</b>

# Zusammenfassung

Umformprozesse, wie Ausbauchen, Streckformen und Tiefziehen, sind für die Herstellung von Bauteilen für den Automobilbau sowie Blechbauteilen im Allgemeinen äußerst wichtig. In dieser Arbeit wird ein ferritischer rostfreier Stahl (DC04) auf der Meso- und Makroskala numerisch untersucht. Im ersten Schritt werden Mikrokomppressionsversuche und makroskopische Zugversuche genutzt, um die Materialparameter des Stahls unter Verwendung eines geometrisch nichtlinearen Einkristall- und Polykristallmodells zu bestimmen. Zweidimensionale Daten aus Messungen mittels Elektronenrückstrahlbeugung (EBSD) werden durch finite Elemente diskretisiert und homogenen Verschiebungsrandbedingungen unterworfen, um im zweiten Schritt lokale Simulationen des Kornverbunds durchzuführen. Im dritten Schritt wird ein zweiskaliges Taylormodell an den Integrationspunkten der finiten Elemente angewendet, um einen Tiefziehprozess unter Berücksichtigung experimenteller Texturdaten zu simulieren. Die gemessene kristallographische Textur wird dafür mit einer Texturkomponentenmethode reduziert, um in das Polykristallmodell Eingang zu finden. Abschließend wird die Grenzformänderung basierend auf dem zuvor genannten Zweiskalenmodell unter Anwendung zweier klassischer Lokalisierungskriterien für verschiedene Belastungspfade analysiert.

# Summary

Metal forming processes such as bulge and stretch forming as well as deep drawing are required for the manufacturing of automotive parts and steel sheet panels. In this thesis, a ferritic stainless steel (DC04) is investigated numerically on the meso and the macro scale. In a first step, micro-pillar compression and macro tensile tests are used to estimate the material parameters using large strain single crystal and polycrystal plasticity models. Two-dimensional electron backscatter diffraction (EBSD) data are discretized by finite elements and subjected to homogeneous displacement boundary conditions for grain scale simulations in the second step. In the third step, a two-scale Taylor type model is applied at the integration points of the finite elements to simulate a deep drawing process based on the experimental crystallographic texture data. The texture data required for the specification of the two-scale polycrystal model are determined via a texture component method. Finally, a formability prediction based on the aforementioned two-scale model is analyzed by applying two classical localization criteria for different strain paths.

# Acknowledgements

First of all, I would like to express my deepest gratitude to my supervisor, Prof. Dr.-Ing. Thomas Böhlke, for giving me the opportunity to write my PhD thesis at his Chair for Continuum Mechanics. His encouragement, guidance and support from the initial to the final level enabled me to develop a more profound understanding of the subject of continuum mechanics. Honestly, I thank him for the excellent and friendly working conditions. Furthermore, I would like to sincerely thank Prof. Dr. rer. nat. Peter Gumbsch, Institute of Applied Materials, Chair for Reliability of Components and Systems, for his support and for reviewing the work.

With a special note I would like to deeply thank the Research Training Group GraKo 1483, and especially the German Research Foundation (Deutsche Forschungsgemeinschaft - DFG) for their financial support. This program offered many opportunities to learn a lot about research skills and team working.

I would also like to extend my thanks to the staff at Steinbuch Centre for Computing (SCC), to the Information Technology Centre of KIT, for their support in high performance computing throughout the numerical implementation of my research project.

Besides my supervisors, I have had the opportunity to benefit from the expertise and support of the members of the Chair for Continuum Mechanics. In this respect, it is my pleasure to thank Katja Jöchen, Felix Fritzen, Barthel Brylka, Johannes Wippler, Rumena Tsotsova, Tom-Alexander Langhoff, Vedran Glavas, Stephan Wulfinghoff, Viktor Müller and Song Lin. They gave me a lot of useful hints and showed interest in the progress of my work. I cannot forget to express my appreciation to Helga Betsarkis and Ute Schlumberger-Maas who are working as institute secretaries for their support and enthusiasm during the time of my studies and work at the Institute of Engineering Mechanics.

I would also like to extend my thanks to all of those who are not mentioned by name, however, who supported me in any respect while writing my thesis.

Finally, I would like to express my deepest gratitude from the bottom of my heart to my parents, my sister, my brother and my girlfriend for their support and all their love during all this time.

# Chapter 1

## Introduction

**Introduction.** Most of the metals used in industrial processes are polycrystalline materials. They are aggregates of approximately single crystals in grains with different crystal orientations. The anisotropic plasticity of polycrystalline materials is mainly caused by non-uniform distributions of crystal orientations (Bunge, 1982, 1987, 1993; Böhlke, 2000). Therefore, the analysis of the crystallographic texture, i.e. preferred crystal orientations, plays an important role in the large strain plasticity theory. Crystallographic texture data allow for the characterization and prediction of the anisotropic plasticity in heterogeneous materials by using statistical models. Some representative studies of different polycrystalline materials with focus on the texture evolution are given, e.g., by Asaro and Needleman (1985); Mathur and Dawson (1989); Bronkhorst et al. (1992); Raabe (1995); Böhlke (2000); Böhlke et al. (2005, 2007); Roters et al. (2010).

Ferritic stainless steels are currently of important interest since they are widely used in automotive systems due to their formability and high corrosion resistance. In the vehicle construction, they could offer a prospective alternative to the austenitic stainless steel grades. The study of microscopic and macroscopic material behavior (Gumbsch, 2003, 2005; Helm et al., 2011) is a key to the successful application of these steels in the modern structural design. Therefore, in close cooperation with other research projects within Research Area A, the main purpose of the thesis is to understand the relation between microstructural properties and the macroscopic behavior of a ferritic stainless steel. As material model, the steel DC04 is considered. A numerical homogenization method will be applied in conjunction with the large strain crystal plasticity law and experimental texture data to account for the microscale information in macroscopic finite element simulations.

The aforementioned crystal plasticity model will be identified based on different experimental data. To validate the model, locally resolved simulations of the polycrystalline DC04 steel sample in a tensile specimen have been carried out. The

experimentally observed local grain reorientations in the polycrystalline sample will be predicted and evaluated at different deformation states. Furthermore, the validated constitutive model will be applied at the integration points of finite elements in a deep drawing simulation. The macroscopic anisotropic material response is evaluated and compared to the experimental data. Finally, the same micro-macro model will be used for a prediction of diffuse necking for different strain paths.

The thesis is organized as follows:

**Chapter 2** describes the constitutive equations of the finite elastoviscoplasticity theory on the grain scale. The continuum mechanical description is established via the large deformation context of non-linear solid mechanics. In order to perform numerical simulations, the constitutive models are integrated in time by means of the implicit Euler integration scheme. A Taylor type polycrystal model is used for the homogenization of the mechanical response. The Taylor model provides a reasonable qualitative approximation of the crystallographic texture evolution in many single-phase cubic materials.

In **Chapter 3** the crystallite orientation distribution function (CODF) is used to characterize statistically the crystal orientations. In particular, mathematical approaches are discussed which allow for a low-dimensional description of crystallographic textures based on texture components. Two different techniques are applied to the crystallographic texture data of a heat treated DC04 steel. The experimental texture data via EBSD measurements have been provided by Project A6.

**Chapter 4** aims to estimate the material parameters in the large strain crystal plasticity model by using uniaxial tensile tests and the crystallographic texture based on experimental EBSD data of a heat treated DC04 steel. The single crystal orientations extracted from 2D EBSD data of the DC04 steel are used. Computational tensile stress-strain curves of tensile tests are compared with experimental results for different tensile directions in the sheet plane to estimate the material parameters. The tensile test data are provided by Project A6 and the Institute of Forming Technology and Lightweight Construction (IUL, Technical University of Dortmund). In addition, the simulation of micro-pillar compression tests is applied to estimate the aforementioned material parameters in a different way. These numerical results are compared to the experimental compression tests for load-displacement, load-time, displacement-time and stress-stretch curves. The experimental micro-pillar test data are provided by Project A6.

**Chapter 5** aims to validate the material model for the DC04 steel by performing a full field FE simulation based on 2D EBSD data under a macroscopic tensile load. The EBSD data set is discretized by finite elements and is subjected to homogeneous displacement boundary conditions approximately describing a large strain uniaxial tensile test. The simulated lattice orientation fields are compared to experimental

measurements of the specimen after the tensile test at different deformation levels. The texture data for different deformation states are provided by Project A6.

**Chapter 6** concentrates on the FE simulation of a deep drawing process similar to industrial metal forming operations. Such a process is simulated by applying the aforementioned two-scale Taylor type model at the integration points of the finite elements. The initial crystallographic texture is reduced by applying a texture component method to the EBSD data. By applying the micro-macro transition method, the earing profile is predicted and compared to experimental data provided by the Institute for Metal Forming Technology (IFU, University of Stuttgart).

**Chapter 7** analyzes two methods to determine the diffuse necking of the rolled DC04 steel sheet for different strain paths. Two classical localization criteria are applied to predict forming limit diagrams (FLDs). The material behaviour at the microscopic level is described based on the aforementioned polycrystal plasticity model. The texture data of heat treated DC04 steel are again assigned to the integration points of finite elements. The computed FLD is compared to experimental results. The experimental data are provided by the Institute for Metal Forming Technology (IFU, University of Stuttgart).

**Chapter 8** summarizes the results. Possible topics of future research are outlined.

**Notation.** Throughout the text, a 2nd-order tensor and a 4th-order tensor are  $\mathbf{A} = A_{ij}\mathbf{e}_i \otimes \mathbf{e}_j$  and  $\mathbb{A} = A_{ijkl}\mathbf{e}_i \otimes \mathbf{e}_j \otimes \mathbf{e}_k \otimes \mathbf{e}_l$ , respectively, where  $\{\mathbf{e}_i\}$  represents an orthonormal basis of the three-dimensional Euclidean space. The symmetric and the skew part of a 2nd-order tensor  $\mathbf{A}$  are denoted by  $\text{sym}(\mathbf{A})$  and  $\text{skw}(\mathbf{A})$ . Symmetric and traceless tensors are designated by a prime, e.g.,  $\mathbf{A}'$ . The set of proper orthogonal 2nd-order tensors is specified by  $SO(3)$ . The scalar product, the dyadic product and the Frobenius norm are denoted by  $\mathbf{A} \cdot \mathbf{B} = \text{tr}(\mathbf{A}^\top \mathbf{B}) = \text{tr}(\mathbf{A}\mathbf{B}^\top)$ ,  $\mathbf{A} \otimes \mathbf{B}$  and  $\|\mathbf{A}\| = (\mathbf{A} \cdot \mathbf{A})^{1/2}$ , respectively. Here,  $\text{tr}(\cdot)$  represents the trace of a 2nd-order tensor.  $\mathbf{I} = \mathbf{e}_i \otimes \mathbf{e}_i$  denotes the 2nd-order identity tensor. In addition,  $\mathbb{I}^S = \frac{1}{2}(\delta_{ik}\delta_{jl} + \delta_{il}\delta_{jk})\mathbf{e}_i \otimes \mathbf{e}_j \otimes \mathbf{e}_k \otimes \mathbf{e}_l$  denotes the 4th-order identity tensor on symmetric 2nd-order tensors. A linear mapping of 2nd-order tensors is written as  $\mathbf{A} = \mathbb{C}[\mathbf{B}]$ . The Rayleigh products of the 2nd-order tensor  $\mathbf{A}$  and a 2nd-order tensor  $\mathbf{C} = C_{ij}\mathbf{e}_i \otimes \mathbf{e}_j$  and a 4th-order tensor  $\mathbb{C} = C_{ijkl}\mathbf{e}_i \otimes \mathbf{e}_j \otimes \mathbf{e}_k \otimes \mathbf{e}_l$  are given by  $\mathbf{A} \star \mathbf{C} = C_{ij}(\mathbf{A}\mathbf{e}_i) \otimes (\mathbf{A}\mathbf{e}_j)$  and  $\mathbf{A} \star \mathbb{C} = C_{ijkl}(\mathbf{A}\mathbf{e}_i) \otimes (\mathbf{A}\mathbf{e}_j) \otimes (\mathbf{A}\mathbf{e}_k) \otimes (\mathbf{A}\mathbf{e}_l)$ , respectively. In the following, a list of symbols frequently used in this thesis is given.

## List of Frequently Used Symbols

Name	Symbol
Young's modulus	$E$
Crystallite orientation distribution function	$f$
Shear modulus	$G$
Bulk modulus	$K$
Strain rate sensitivity	$m$
Plastic strain ratio	$r$
Volume in the reference placement	$V$
Reference shear rate	$\dot{\gamma}_0$
Slip rate of the slip system $\alpha$	$\dot{\gamma}_\alpha$
Poisson ratio	$\nu$
Drag stress	$\sigma_D$
Flow stress	$\sigma_F$
Critical resolved shear stress	$\tau^C$
Initial critical resolved shear stress	$\tau_0^C$
Asymptotic resolved shear stress	$\tau_{V0}^C$
Shear stress of the slip system $\alpha$	$\tau_\alpha$
Volume fraction of a crystal or a grain $\beta$	$v_\beta$
Hardening modulus	$\Theta_0$
Slip direction of the slip system $\alpha$	$\mathbf{d}_\alpha$
Orthonormal basis	$\{\mathbf{e}_i\}$
Lattice vector	$\{\mathbf{g}_i\}$
Deformation gradient	$\mathbf{F}$
Velocity gradient	$\mathbf{L}$
Slip plane normal of the slip system $\alpha$	$\mathbf{n}_\alpha$
Kirchhoff stress tensor	$\boldsymbol{\tau}$
Right Cauchy-Green tensor	$\mathbf{C}$
Green strain tensor	$\mathbf{E}$
2nd-order identity tensor	$\mathbf{I}$
Flow rule	$\tilde{\mathbf{k}}$
Schmid tensor of the slip system $\alpha$	$M_\alpha$
Proper orthogonal tensor describing a crystal orientation	$\mathbf{Q}$
Proper orthogonal part of the deformation gradient	$\mathbf{R}$
Mandel stress tensor	$\mathbf{T}_e$
4th-order stiffness tensor	$\mathbb{C}$
4th-order symmetric identity tensor on 2nd-order tensors	$\mathbb{I}^S$

<b>Name</b>	<b>Symbol</b>
Set of 2nd-order tensors	$Lin$
Set of invertible 2nd-order tensors	$Inv$
Set of symmetric 2nd-order tensors	$Sym$
Set of symmetric and positive definite 2nd-order tensors	$Psym$
Set of skew-symmetric 2nd-order tensors	$Skw$
Set of all symmetric transformations	$S$
Set of all real number	$R$
Material gradient operator	$Grad$
Spatial gradient operator	$grad$
Full set of equivalent planes	$\{hkl\}$
Full set of equivalent directions	$\langle uvw \rangle$
Set of slip systems	$\{hkl\}\langle uvw \rangle$
Dyadic product	$(\cdot) \otimes (\cdot)$
Quantity with respect to the undistorted configuration	$(\tilde{\cdot})$
Homogenized, i.e., effective quantity	$(\bar{\cdot})$
Material time derivative	$(\dot{\cdot})$
Frobenius norm	$\ \cdot\ $
<b>Tensor components and products</b>	
Kronecker symbol: $\delta_{ij}$	$(\mathbf{I})_{ij}$
$\frac{1}{2}(\delta_{ik}\delta_{jl} + \delta_{il}\delta_{kj})$	$(\mathbb{I})_{ijkl}$
$A_{ij}b_j$	$(\mathbf{A}\mathbf{b})_i$
$A_{ij}B_{jk}$	$(\mathbf{A}\mathbf{B})_{ik}$
$A_{ijkl}B_{klmn}$	$(\mathbb{A}\mathbb{B})_{ijmn}$
$a_ib_i$	$\mathbf{a} \cdot \mathbf{b}$
$A_{ij}B_{ij}$	$\mathbf{A} \cdot \mathbf{B}$
$A_{ijkl}B_{ijkl}$	$\mathbb{A} \cdot \mathbb{B}$
$a_ib_j$	$(\mathbf{a} \otimes \mathbf{b})_{ij}$
$A_{ij}B_{kl}$	$(\mathbf{A} \otimes \mathbf{B})_{ijkl}$
$C_{ijkl}A_{kl}$	$(\mathbf{C}[\mathbf{A}])_{ij}$
$\epsilon_{ijk}n_k$	$(\epsilon[\mathbf{n}])_{ij}$

## Chapter 2

# Constitutive Models for Single Crystals and Polycrystals

### 2.1 Large Strain Single Crystal Plasticity Material Model

**Elastic law.** In this section, an elastoviscoplastic single crystal constitutive model in the large strain crystal plasticity theory is introduced. Conceptually, the model is based upon the assumptions of small elastic strains and finite plastic strains and rotations. Plastic deformation is assumed to be the result of distinct slip mechanisms on specific crystallographic planes. The theory was developed in works of Asaro and Needleman (1985); Bronkhorst et al. (1992).

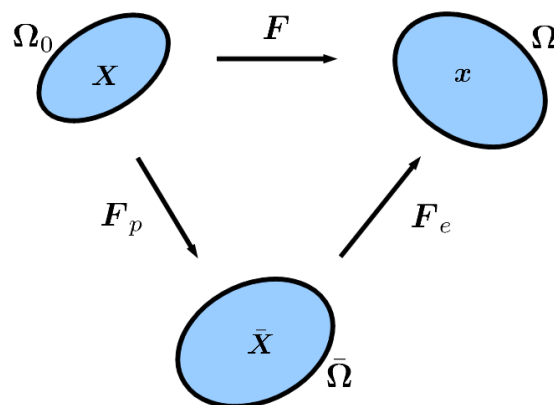


Figure 2.1: The deformation gradient  $F$  maps a material point  $X$  in the reference configuration  $\Omega_0$  to  $\bar{X}$  in the intermediate configuration  $\bar{\Omega}$  by  $F_p$ , and to  $x$  in the spatial configuration  $\Omega$  by  $F_e$ .

The deformation gradient can be decomposed multiplicatively into an elastic part  $F_e$

and a plastic part  $\mathbf{F}_p$ , as shown in Fig. 2.1 (Lee, 1969; Asaro and Rice, 1977)

$$\mathbf{F} = \mathbf{F}_e \mathbf{F}_p. \quad (2.1)$$

The plastic deformation  $\mathbf{F}_p$  is the plastic contribution from crystallographic slips. The elastic deformation  $\mathbf{F}_e$  accounts for the lattice distortion, which is inherently elastic. As the elastic strains are assumed to be small, a linearized relation between a conjugate pair of stress and strain measures is applicable for the description of the elastic behavior. Here, the elastic law is assumed to be given by

$$\boldsymbol{\tau} = \mathbf{F}_e \tilde{\mathbb{C}}[\mathbf{E}_e] \mathbf{F}_e^T. \quad (2.2)$$

The Kirchhoff stress tensor is given by  $\boldsymbol{\tau} = \det(\mathbf{F})\boldsymbol{\sigma}$ , with  $\boldsymbol{\sigma}$  being the Cauchy stress tensor. Green's strain tensor is defined by

$$\mathbf{E}_e = (\mathbf{C}_e - \mathbf{I})/2, \quad (2.3)$$

with  $\mathbf{I}$  being the 2nd-order unit tensor and the right (elastic) Cauchy-Green tensor

$$\mathbf{C}_e = \mathbf{F}_e^T \mathbf{F}_e. \quad (2.4)$$

The reference stiffness tensor  $\tilde{\mathbb{C}}$  with respect to the orthonormal basis  $\mathbf{B}_\alpha$ , is given by

$$\tilde{\mathbb{C}} = \tilde{C}_{\alpha\beta} \mathbf{B}_\alpha \otimes \mathbf{B}_\beta = \begin{bmatrix} C_{1111} & C_{1122} & C_{1122} & 0 & 0 & 0 \\ & C_{1111} & C_{1122} & 0 & 0 & 0 \\ & & C_{1111} & 0 & 0 & 0 \\ & & & 2C_{1212} & 0 & 0 \\ \text{sym.} & & & & 2C_{1212} & 0 \\ & & & & & 2C_{1212} \end{bmatrix} \mathbf{B}_\alpha \otimes \mathbf{B}_\beta. \quad (2.5)$$

The components  $\tilde{C}_{\alpha\beta}$  are defined by  $\tilde{C}_{\alpha\beta} = \mathbf{B}_\alpha \cdot \tilde{\mathbb{C}}[\mathbf{B}_\beta]$ . The following orthonormal base tensors  $\mathbf{B}_\alpha$  are used

$$\begin{aligned} \mathbf{B}_1 &= \mathbf{e}_1 \otimes \mathbf{e}_1 \\ \mathbf{B}_2 &= \mathbf{e}_2 \otimes \mathbf{e}_2 \\ \mathbf{B}_3 &= \mathbf{e}_3 \otimes \mathbf{e}_3 \\ \mathbf{B}_4 &= \frac{\sqrt{2}}{2}(\mathbf{e}_2 \otimes \mathbf{e}_3 + \mathbf{e}_3 \otimes \mathbf{e}_2) \\ \mathbf{B}_5 &= \frac{\sqrt{2}}{2}(\mathbf{e}_1 \otimes \mathbf{e}_3 + \mathbf{e}_3 \otimes \mathbf{e}_1) \\ \mathbf{B}_6 &= \frac{\sqrt{2}}{2}(\mathbf{e}_1 \otimes \mathbf{e}_2 + \mathbf{e}_2 \otimes \mathbf{e}_1). \end{aligned} \quad (2.6)$$

Due to the cubic material under consideration, the stiffness tensor  $\tilde{\mathbb{C}}$  has three independent elastic constants and 9 planes of symmetry, see, e.g., Böhlke (2000).

**Flow rule and hardening law.** A rate-dependent flow rule specifies the time evolution of the plastic part  $F_p$  of  $F$

$$\dot{F}_p F_p^{-1} = \sum_{\alpha} \dot{\gamma}_{\alpha} \tilde{M}_{\alpha}, \quad \dot{\gamma}_{\alpha} = \dot{\gamma}_0 \operatorname{sgn}(\tau_{\alpha}) \left| \frac{\tau_{\alpha}}{\tau^C} \right|^m, \quad (2.7)$$

where the exponent  $m$  quantifies the strain-rate sensitivity of the material,  $\dot{\gamma}_0$  is a reference rate, and  $\tilde{M}_{\alpha}$  the Schmid tensor.  $\tau^C$  denotes the critical resolved shear stress. A rate-dependent Kocks-Mecking hardening model (Kocks and Mecking, 2003; Böhlke et al., 2005)

$$\dot{\tau}^C(\tau_{\alpha}, \tau^C) = \Theta_0 \left( 1 - \frac{\tau^C}{\tau_V^C(\tau_{\alpha}, \tau^C)} \right) \dot{\gamma}(\tau_{\alpha}, \tau^C) \quad (2.8)$$

is used, where the critical Voce stress is specified by

$$\tau_V^C(\tau_{\alpha}, \tau^C) = \tau_{V0}^C \left| \frac{\dot{\gamma}(\tau_{\alpha}, \tau^C)}{\dot{\gamma}_0} \right|^{\frac{1}{n}}. \quad (2.9)$$

with the asymptotic critical resolved shear stress  $\tau_{V0}^C$  and the initial hardening modulus  $\Theta_0$ . The rate of the accumulated plastic slip is computed by

$$\dot{\gamma} = \sum_{\alpha} |\dot{\gamma}_{\alpha}(\tau_{\alpha}, \tau^C)|. \quad (2.10)$$

The resolved shear stress is defined by

$$\tau_{\alpha} = \mathbf{T}'_e \cdot \tilde{M}_{\alpha}, \quad (2.11)$$

where

$$\mathbf{T}'_e = \mathbf{C}_e \mathbf{S}_e^{2PK} \quad (2.12)$$

denotes the Mandel stress tensor. The second Piola-Kirchhoff in the undistorted state is given by  $\mathbf{S}_e^{2PK} = J \mathbf{F}_e^{-1} \boldsymbol{\tau} \mathbf{F}_e^{-T}$ .  $J = \det(\mathbf{F}_e)$  is the determinant of  $\mathbf{F}_e$ . The Schmid or slip system tensors are rank-one tensors, which are defined in terms of the slip direction  $\tilde{\mathbf{d}}_{\alpha}$  and slip plane normal  $\tilde{\mathbf{n}}_{\alpha}$  in the undistorted configuration

$$\tilde{M}_{\alpha} = \tilde{\mathbf{d}}_{\alpha} \otimes \tilde{\mathbf{n}}_{\alpha}. \quad (2.13)$$

The initial conditions for the ordinary differential equation are  $\mathbf{F}_e(0) = \mathbf{Q}(t=0) \in SO(3)$  and the initial critical resolved shear stress  $\tau^C(0) = \tau_0^C$ . Considering a cubic symmetry, the crystal orientation is given by a proper orthogonal tensor  $\mathbf{Q}(t) = \mathbf{g}_i(t) \otimes \mathbf{e}_i$ , where the vectors  $\mathbf{g}_i$  and  $\mathbf{e}_i$  denote the orthonormal lattice vectors and the fixed orthonormal basis, respectively. The initial orientation of the single crystal  $\mathbf{Q}(t=0) = \mathbf{g}_i(0) \otimes \mathbf{e}_i$  is defined in terms of the orthonormal lattice vectors  $\mathbf{g}_i(0)$  at the time  $t=0$ . The definition of the crystal orientation characterized by  $\mathbf{Q}$  is discussed further in the next chapter.

**Slip mechanisms in BCC metals.** Gambin (2001) states that  $\{110\}$ ,  $\{112\}$  and  $\{123\}$  families of slip systems contain the crystallographic slip planes for inelastic deformations of BCC materials. Different BCC slip planes commonly share the main diagonal direction  $\langle 111 \rangle$  (Fig. 2.2). The slip systems  $\tilde{\mathbf{d}}_\alpha \otimes \tilde{\mathbf{n}}_\alpha$  are specified from Tables 2.1–2.3 with respect to the orthonormal basis  $\mathbf{e}_i$  for the three different types of BCC slip systems. The combination of a slip plane and a slip direction forms a slip system  $\tilde{\mathbf{M}}_\alpha = \tilde{\mathbf{d}}_\alpha \otimes \tilde{\mathbf{n}}_\alpha$ . The slip systems are divided into 4 families, each family possessing a common slip direction. Their directions are:  $[1, 1, 1]$ ,  $[-1, 1, 1]$ ,  $[1, -1, 1]$  and  $[1, 1, -1]$ . Hence, twelve slip systems belong to each direction. The slip plane normals,  $\tilde{\mathbf{n}}_\alpha$ , of slip systems of each family lie on the plane which is perpendicular to the corresponding slip direction.

In the work of Yalcinkaya et al. (2008), intrinsic characteristics of BCC crystals are revealed by using a proper parameter identification method. The authors applied a BCC crystal plasticity model to perform uniaxial tension simulations at the material point level for different types of BCC single crystals and compare these with experiments. The results indicate that  $\{110\}$  and  $\{112\}$  planes are identified as intrinsic slip systems of BCC crystals, but not the  $\{123\}$  plane. Therefore, in this thesis the attention is focused on a combination of  $\{110\}\langle 111 \rangle$  and  $\{112\}\langle 111 \rangle$  slip system families. There are two slip directions in each of these slip planes along the main diagonals of the cube (see Fig. 2.2). In total, there are 24 slip systems, see Tables 2.1 and 2.2.

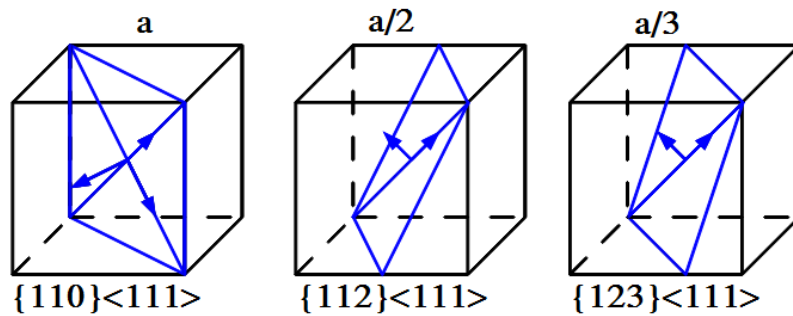


Figure 2.2: BCC slip systems.

## 2.2 Polycrystal Model

The crystallographic texture of polycrystalline materials is known to be of significant importance for the sheet metal behaviour. If the crystallographic texture is taken into account at the integration point level, Taylor type polycrystal models are numerically

## Constitutive Models for Single Crystals and Polycrystals

$\alpha$	1	2	3	4	5	6
$\sqrt{2}[\tilde{n}_i^\alpha]$	[1, -1, 0]	[1, -1, 0]	[1, 0, -1]	[1, 0, -1]	[0, 1, -1]	[0, 1, -1]
$\sqrt{3}[\tilde{d}_i^\alpha]$	[1, 1, 1]	[1, 1, -1]	[1, 1, 1]	[1, -1, 1]	[1, 1, 1]	[-1, 1, 1]
$\alpha$	7	8	9	10	11	12
$\sqrt{2}[\tilde{n}_i^\alpha]$	[1, 1, 0]	[1, 1, 0]	[1, 0, 1]	[1, 0, 1]	[0, 1, 1]	[0, 1, 1]
$\sqrt{3}[\tilde{d}_i^\alpha]$	[-1, 1, 1]	[1, -1, 1]	[-1, 1, 1]	[1, 1, -1]	[1, -1, 1]	[1, 1, -1]

Table 2.1: 12 BCC slip systems of  $\{110\}\langle 111 \rangle$  (Paquin et al., 2001).

$\alpha$	1	2	3	4	5	6
$\sqrt{6}[\tilde{n}_i^\alpha]$	[1, 1, 2]	[-1, 1, 2]	[1, -1, 2]	[1, 1, -2]	[1, 2, 1]	[-1, 2, 1]
$\sqrt{3}[\tilde{d}_i^\alpha]$	[1, 1, -1]	[1, -1, 1]	[-1, 1, 1]	[1, 1, 1]	[1, -1, 1]	[1, 1, -1]
$\alpha$	7	8	9	10	11	12
$\sqrt{6}[\tilde{n}_i^\alpha]$	[1, -2, 1]	[1, 2, -1]	[2, 1, 1]	[-2, 1, 1]	[2, -1, 1]	[2, 1, -1]
$\sqrt{3}[\tilde{d}_i^\alpha]$	[1, 1, 1]	[-1, 1, 1]	[-1, 1, 1]	[1, 1, 1]	[1, 1, -1]	[1, -1, 1]

Table 2.2: 12 BCC slip systems of  $\{112\}\langle 111 \rangle$  (Yalcinkaya et al., 2008).

$\alpha$	1	2	3	4	5	6
$\sqrt{14}[\tilde{n}_i^\alpha]$	[1, 2, 3]	[-1, 2, 3]	[1, -2, 3]	[1, 2, -3]	[1, 3, 2]	[-1, 3, 2]
$\sqrt{3}[\tilde{d}_i^\alpha]$	[1, 1, -1]	[1, -1, 1]	[-1, 1, 1]	[1, 1, 1]	[1, -1, 1]	[1, 1, -1]
$\alpha$	7	8	9	10	11	12
$\sqrt{14}[\tilde{n}_i^\alpha]$	[1, -3, 2]	[1, 3, -2]	[2, 1, 3]	[-2, 1, 3]	[2, -1, 3]	[2, 1, -3]
$\sqrt{3}[\tilde{d}_i^\alpha]$	[1, 1, 1]	[-1, 1, 1]	[1, 1, -1]	[1, -1, 1]	[-1, 1, 1]	[1, 1, 1]
$\alpha$	13	14	15	16	17	18
$\sqrt{14}[\tilde{n}_i^\alpha]$	[2, 3, 1]	[-2, 3, 1]	[2, -3, 1]	[2, 3, -1]	[3, 1, 2]	[-3, 1, 2]
$\sqrt{3}[\tilde{d}_i^\alpha]$	[1, -1, 1]	[1, 1, -1]	[1, 1, 1]	[-1, 1, 1]	[-1, 1, 1]	[1, 1, 1]
$\alpha$	19	20	21	22	23	24
$\sqrt{14}[\tilde{n}_i^\alpha]$	[3, -1, 2]	[3, 1, -2]	[3, 2, 1]	[-3, 2, 1]	[3, -2, 1]	[3, 2, -1]
$\sqrt{3}[\tilde{d}_i^\alpha]$	[1, 1, -1]	[1, -1, 1]	[-1, 1, 1]	[1, 1, 1]	[1, 1, -1]	[1, -1, 1]

Table 2.3: 24 BCC slip systems of  $\{123\}\langle 111 \rangle$  (Nemat-Nasser, 2002).

the most effective two-scale models. Taylor models, (Taylor, 1938; Van Houtte, 1988; Mathur and Dawson, 1989; Raabe, 1995; Miehe et al., 1999; Böhlke et al., 2006, 2007; Raabe et al., 2007; Jöchen and Böhlke, 2010), assume a homogeneous deformation field through the microstructure of the polycrystal. The trivial localization assumption of a homogeneous deformation field can be formulated as follows

$$\mathbf{L} = \bar{\mathbf{L}}, \quad (2.14)$$

where  $\mathbf{L}$  and  $\bar{\mathbf{L}}$  are mesoscopic and macroscopic velocity gradients, respectively. The resulting macroscopic deformation gradient is equal to the volume average of the microscopic deformation gradient

$$\bar{\mathbf{F}} = \frac{1}{V} \int_V \mathbf{F} \, dV \quad (2.15)$$

with respect to the reference configuration. The effective Kirchhoff stress tensor is computed as the volume average of crystal stress with respect to the current configuration

$$\bar{\boldsymbol{\tau}} = \frac{1}{V} \int_V \boldsymbol{\tau} \, dV = \frac{1}{v} \int_v \boldsymbol{\sigma} \, dv = \sum_{\beta}^M \nu_{\beta} \boldsymbol{\tau}_{\beta}, \quad (2.16)$$

where  $\nu_{\beta}$  is the volume fraction of the grain  $\beta$  and  $\boldsymbol{\tau}_{\beta}$  is the corresponding Kirchhoff stress tensor.  $M$  is the total number of grains in the discretized crystallographic texture.

# Chapter 3

## The Crystallite Orientation Distribution Function (CODF)

### 3.1 Basic Properties of the CODF

In this section, an effective method is introduced for the selection of representative grain orientations based on texture data. The orientation distribution must reproduce the overall crystallographic texture of the experimental DC04 steel material in a statistical as well as mechanical sense. Such technique has been recently studied and applied for several important applications, see, e.g., Kanetake et al. (1985); Mathur and Dawson (1989); Miehe et al. (1999); Paquin et al. (2001); Nemat-Nasser (2002); Dawson et al. (2004); Habraken (2004); Böhlke et al. (2005, 2006); Raabe et al. (2007); Phan et al. (2011c).

The crystal orientation distribution function (CODF) represents the crystallographic texture by a volume fraction description of crystal orientations. Mathematically, it represents the volume fraction of crystals with orientation  $\mathbf{Q}$ , i.e.

$$\frac{dV}{V} = f(\mathbf{Q})d\mathbf{Q}. \quad (3.1)$$

For a random texture  $f(\mathbf{Q}) \equiv 1$  holds. The orientation of a single crystal (see Fig. 3.1) in a polycrystalline structure can be uniquely determined by the specification of the rotation  $\mathbf{Q} \in Orth$  which maps the sample fixed basis vectors  $e_i$  onto the lattice vectors  $g_i$  by  $g_i = \mathbf{Q}e_i$ . According to Bunge's convention (Bunge, 1982), firstly the crystal coordinate system is rotated about the  $g_3$ -axis via the angle  $\phi_1$ , then about the  $g_1$ -axis in its new orientation via the angle  $\Phi$  and, finally, about the  $g_3$ -axis in its new orientation via the angle  $\phi_2$ . In particular, the rotation  $\mathbf{Q}$  is commonly parameterized by a triple of Euler angles  $\phi_1, \Phi, \phi_2$  and is described through a  $3 \times 3$  orthogonal matrix

## The Crystallite Orientation Distribution Function (CODF)

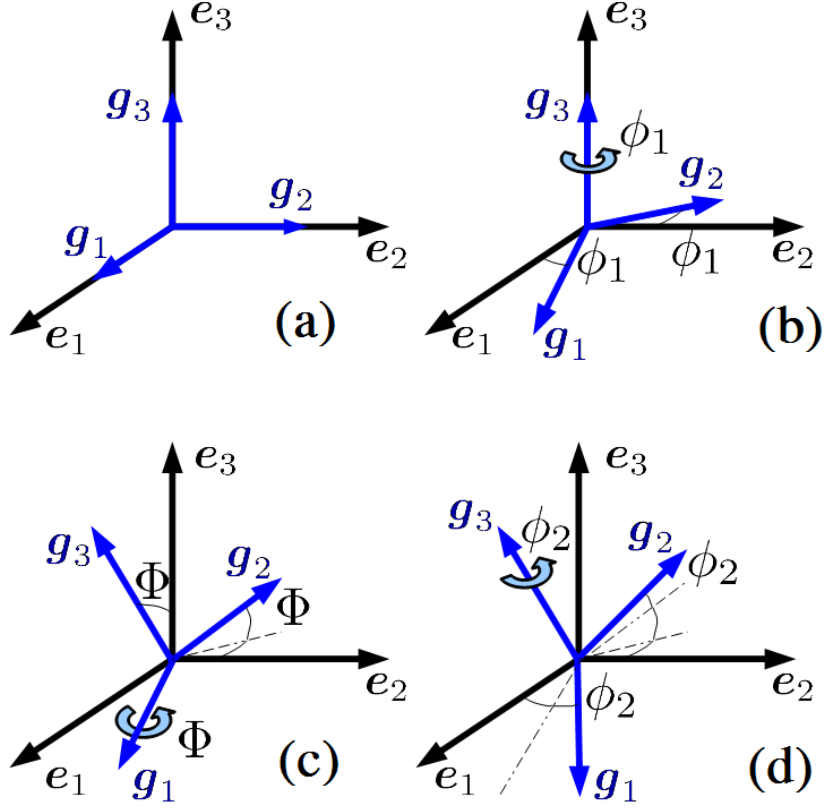


Figure 3.1: Definition of a crystal orientation by three Euler angles: (a) initial state, (b) angle  $\phi_1$ , (c) angle  $\Phi$ , and (d) angle  $\phi_2$ .

given by

$$Q_{ij} = \begin{bmatrix} \cos\phi_1 & -\sin\phi_1 & 0 \\ \sin\phi_1 & \cos\phi_1 & 0 \\ 0 & 0 & 1 \end{bmatrix} \begin{bmatrix} 1 & 0 & 0 \\ 0 & \cos\Phi & -\sin\Phi \\ 0 & \sin\Phi & \cos\Phi \end{bmatrix} \begin{bmatrix} \cos\phi_2 & -\sin\phi_2 & 0 \\ \sin\phi_2 & \cos\phi_2 & 0 \\ 0 & 0 & 1 \end{bmatrix} \quad (3.2)$$

$$= \begin{bmatrix} \cos\phi_1\cos\phi_2 - \sin\phi_1\cos\Phi\sin\phi_2 & -\cos\phi_1\sin\phi_2 - \sin\phi_1\cos\Phi\cos\phi_2 & \sin\Phi\sin\phi_1 \\ \sin\phi_1\cos\phi_2 + \cos\phi_1\cos\Phi\sin\phi_2 & -\sin\phi_1\sin\phi_2 + \cos\phi_1\cos\Phi\cos\phi_2 & -\sin\Phi\cos\phi_1 \\ \sin\Phi\sin\phi_2 & \sin\Phi\cos\phi_2 & \cos\Phi \end{bmatrix} \quad (3.3)$$

The properties of the rotational matrices can be found in detail in Morawiec (2004). The infinitesimal volume element  $dQ$  on the orientation space  $SO(3)$  is given by

$$dQ = \frac{1}{8\pi^2} \sin(\Phi) d\phi_1 d\phi_2 d\Phi. \quad (3.4)$$

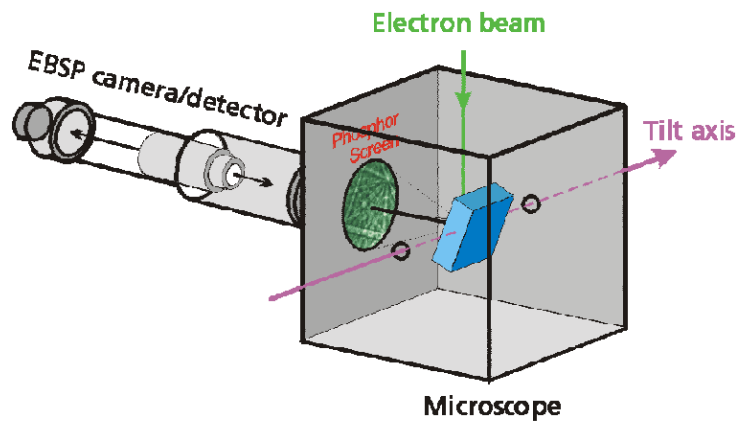


Figure 3.2: Experimental set-up for EBSD measurements (provided by Project A6).

### 3.2 Experimental Identification of the CODF based on Electron Backscatter Diffraction Data (EBSD)

In recent years, the EBSD technique (Fig. 3.2) has become an increasingly popular characterization technique. EBSD has been employed as an important technique for the quantitative characterization of different microstructural properties such as the grain size, the grain boundary structure, and the orientation distribution (see, e.g., Maitland (2004); Maitland and Sitzman (2006); Schwartz et al. (2009)). The main objective of the technique is to obtain space resolved crystallographic information by a Scanning Electron Microscope (SEM).



Figure 3.3: EBSD microstructural image of DC04 steel before tensile test (experiment by Project A6).

For every point analyzed on a sample, the position, the phase, the orientation and some data quality information are stored. The stored data set is a database of measurements produced by scanning the beam in a regular grid over the sample. The data format is shown in Table 3.1 for the tensile experiment performed by Project A6. Each row

## The Crystallite Orientation Distribution Function (CODF)

Phase	X	Y	Euler1	Euler2	Euler3	MAD	BC	BS	Bands	Error	Index
1	0	0	31.850	50.647	51.302	0.6995	100	157	8	0	0.0000
1	1.3	0	31.902	50.507	51.458	0.5294	99	150	8	0	0.0000
1	2.6	0	32.094	50.351	51.110	0.7732	98	151	8	0	0.0000
⋮	⋮	⋮	⋮	⋮	⋮	⋮	⋮	⋮	⋮	⋮	⋮
⋮	⋮	⋮	⋮	⋮	⋮	⋮	⋮	⋮	⋮	⋮	⋮
1	24.7	0	351.28	46.522	67.917	0.9090	101	152	8	0	0.0000
0	26	0	0.0000	0.0000	0.0000	0.0000	99	184	0	3	1.0000
1	27.3	0	351.13	46.380	67.323	0.5893	108	179	8	0	0.0000
⋮	⋮	⋮	⋮	⋮	⋮	⋮	⋮	⋮	⋮	⋮	⋮
⋮	⋮	⋮	⋮	⋮	⋮	⋮	⋮	⋮	⋮	⋮	⋮
1	230.1	191.1	51.971	14.733	18.106	0.4829	102	87	8	0	0.0000
1	231.4	191.1	51.950	14.549	18.531	0.6734	106	91	8	0	0.0000
1	232.7	191.1	51.149	14.898	18.912	0.7215	99	93	8	0	0.0000

Table 3.1: The EBSD data set of the tensile experiment before tensile test including 22641 rows and 12 columns (experiment by Project A6).

is a measurement point in the map and each column is one of the several measured parameters. The parameters are explained shortly as follows.

In the first column, each match unit contains the information necessary to model the EBSD pattern produced by the expected phase in the sample. The best fit between each match unit and the experimental EBSD pattern determines the phase and the orientation of the point on the sample under the beam. The phase values 1 indicate the expected phases of ferrite while the phase values 0 correspond to measurement errors. The second and third column are the X- and Y-position of the measurement points. Their dimensional unit is  $\mu\text{m}$ . The orientation is recorded by using the aforementioned Euler angle convention. Three Euler angles (in degrees), shown schematically in Fig. 3.1, are used to describe the crystallographic orientation of the crystals in relation to a reference coordinate system. The mean angular deviation (MAD) is given in degree in the fourth column and specifies the averaged angular misfit between detected and simulated Kikuchi bands. Furthermore, some additional features in the experimental database could be taken into account. For example, the band contrast (BC) is a quality factor of EBSD pattern obtained from the Hough transform that describes the average intensity of the Kikuchi bands with respect to the overall intensity. Band slope (BS) is an image quality factor derived from the Hough transform that describes the maximum intensity gradient at the margins of the Kikuchi bands. The values of both BC and BS are scaled to a byte range from 0 to 255, i.e. from low to high contrast for BC and from

## The Crystallite Orientation Distribution Function (CODF)

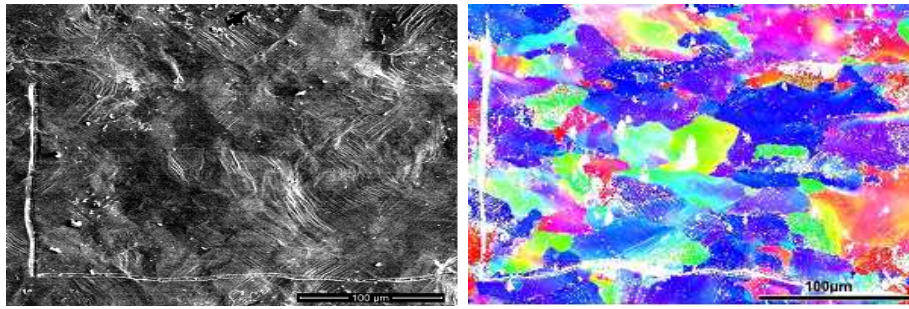


Figure 3.4: EBSD microstructural images of DC04 steel after tensile test (experiment by Project A6): (left) Image of the rough surface and (right) grains with different orientations.

low to high maximum contrast difference for BS; the higher the value of BS, the sharper the band (Maitland and Sitzman, 2006). These scales of BC or BS are mapped to a gray scale from black to white. In Fig. 3.3, an orientation map of the polycrystal structure before tensile test is shown. Different colors indicate individual crystal orientations. Fig. 3.4 (left) shows a roughening surface based on the band contrast (BC) and band slope (BS). Additionally, a related orientation map of the experimental tensile test for 20% elongation is shown in Fig. 3.4 (right) in order to identify glide bands in different grains.

### 3.2.1 Cold Formed and Heat Treated Specimens

The specimen of DC04 steel has been investigated for the cold formed and the heat treated process by using the aforementioned EBSD technique within Project A6 to obtain a corresponding database and to simultaneously identify a two-dimensional grain structure. The heat treated process often implies the development of a new microstructure and the formation of a new crystallographic texture. A new structure of grain boundaries and a new microstructure at the micro scale are formed during the heat treated process. Furthermore, the crystal orientations of new grains can be different from those in the deformed microstructure. Some detailed descriptions of these phenomena can be found in Cotterill and Mould (1976); Wilbrandt (1985). An experimental texture database related to the heat treated process is considered and shown in Table 3.2. The total number of rows and columns are 192266 and 12, respectively. MTEX, a Matlab toolbox recently developed by Hielscher (2010), is used for the quantitative analysis of experimental textures. MTEX allows to import the EBSD database under different data formats and to obtain a two-dimensional grain structure with corresponding crystal orientations. The heat treated EBSD database shown in Table 3.2, has been imported into the MTEX toolbox to identify the

## The Crystallite Orientation Distribution Function (CODF)

Phase	X	Y	Euler1	Euler2	Euler3	MAD	BC	BS	Bands	Error	Index
0	0	0	0.0000	0.0000	0.0000	0.0000	89	153	0	3	1.0000
1	2	0	57.574	9.9495	30.985	0.2763	89	253	7	0	0.0000
1	4	0	58.866	10.229	29.698	0.3906	93	242	7	0	0.0000
⋮	⋮	⋮	⋮	⋮	⋮	⋮	⋮	⋮	⋮	⋮	⋮
⋮	⋮	⋮	⋮	⋮	⋮	⋮	⋮	⋮	⋮	⋮	⋮
1	926	468	246.20	43.831	44.345	0.3089	118	238	7	0	0.0000
1	928	468	246.12	43.781	44.340	0.4902	118	238	7	0	0.0000
1	930	468	246.15	43.786	44.487	0.4097	116	241	7	0	0.0000
⋮	⋮	⋮	⋮	⋮	⋮	⋮	⋮	⋮	⋮	⋮	⋮
⋮	⋮	⋮	⋮	⋮	⋮	⋮	⋮	⋮	⋮	⋮	⋮
1	998	764	329.37	41.729	34.829	0.4954	102	255	7	0	0.0000
1	1000	764	329.34	41.658	34.866	0.5155	98	249	7	0	0.0000
1	1002	764	329.40	41.797	34.753	0.4293	107	255	7	0	0.0000

Table 3.2: File format of the EBSD data set of the heat treated DC04 steel sample (experiment by Project A6).

grains and their boundaries. The imported data could be corrected according to the MAD values, the grain size or the specimen alignment. For the detection of grains, MTEX offers a fully automatic procedure to identify all different grains in the EBSD database. In MTEX, this algorithm can be applied to two-dimensional or three-dimensional measurements. The main steps are the determination of the misorientation between neighbouring measurement points, followed by a cluster analysis, where the neighbouring measurement points are grouped into sets with a misorientation lower than a given threshold (Morawiec, 2003) defined orthogonal mapping. In order to identify a grain from the EBSD measurement, it is necessary to determine its grain boundary and the average orientation inside the grain. These identifications can be handled by the open-source texture toolbox MTEX in terms of the misorientation over the set of all measurement points inside a grain. The misorientation  $\Delta Q$  calculated from orientations  $Q$  of the neighbourhood grains, for example, the misorientation  $\Delta Q_{12}$  between grain 1,  $Q_1$ , and grain 2,  $Q_2$ , is given by

$$\Delta Q_{12} = Q_1^{-1} Q_2. \quad (3.5)$$

The heat treated EBSD microstructure and the clustered heat treated EBSD microstructure are shown in Fig. 3.5. In the raw database, the total number of measurement points is 192266. The size of this heat treated EBSD microstructure is  $1002 \times 764 \mu\text{m}$ . The area of a measurement point is  $4 \mu\text{m}^2$ . The number of the erroneous measurement points is 4151, approximately 2.15% of the area fraction.

## The Crystallite Orientation Distribution Function (CODF)

After the clustering process in MTEX, grain boundaries have been identified and the total number of the identified grains has been found to be 2554. An output database is shown in Table 3.3, including three Euler angles of clustered grains and their corresponding pixels.

Grain	Euler1	Euler2	Euler3	Pixels
1	83.32	47.374	23.528	3
2	117.36	47.152	37.653	4
3	-92.53	38.297	82.924	1
4	25.048	127.55	158.2	1
5	-15.257	46.542	37.09	6
⋮	⋮	⋮	⋮	⋮
⋮	⋮	⋮	⋮	⋮
⋮	⋮	⋮	⋮	⋮
2550	0.74703	14.359	11.114	71
2551	-113.42	43.691	47.862	443
2552	-151.99	44.525	71.867	7
2553	-157.13	42.302	62.368	21
2554	-30.854	41.545	34.8	72

Table 3.3: The data set for identification of grains in the clustered heat treated specimen of DC04 steel.

It has been found that there are approximately 2554 grains. For the time-consuming numerical finite element computations, the number of grains needs to be reduced, simultaneously representing the crystallographic texture data accurately. Here, two important characteristics for the graphical representation of the texture data are to be evaluated. The first is the pole figure which is used to plot a set of poles for corresponding grain orientations based on stereographic projections in 3D space. The second is the aforementioned CODF. A reduced crystallographic texture including only 200 grains with the largest volume fractions is used for the numerical homogenization. The  $\{111\}$ ,  $\{100\}$  and  $\{110\}$  pole figures and the CODF of 2554 grains and 200 grains, respectively, are represented in Fig. 3.6 and Fig. 3.7. In Figure 3.6, the CODFs are determined based on the kernel distribution of von Mises Fisher in the MTEX algorithm. It can be seen that the pole figures and the CODF of 2554 and 200 grains, respectively, are approximately similar.

In the following, considering the case of a cubic crystal symmetry, an orthotropic orientation data set is obtained by rotating counterclockwise the grain orientation data set 180 degrees in turn about the orthonormal axes in the lattice system. The orthogonal

## The Crystallite Orientation Distribution Function (CODF)

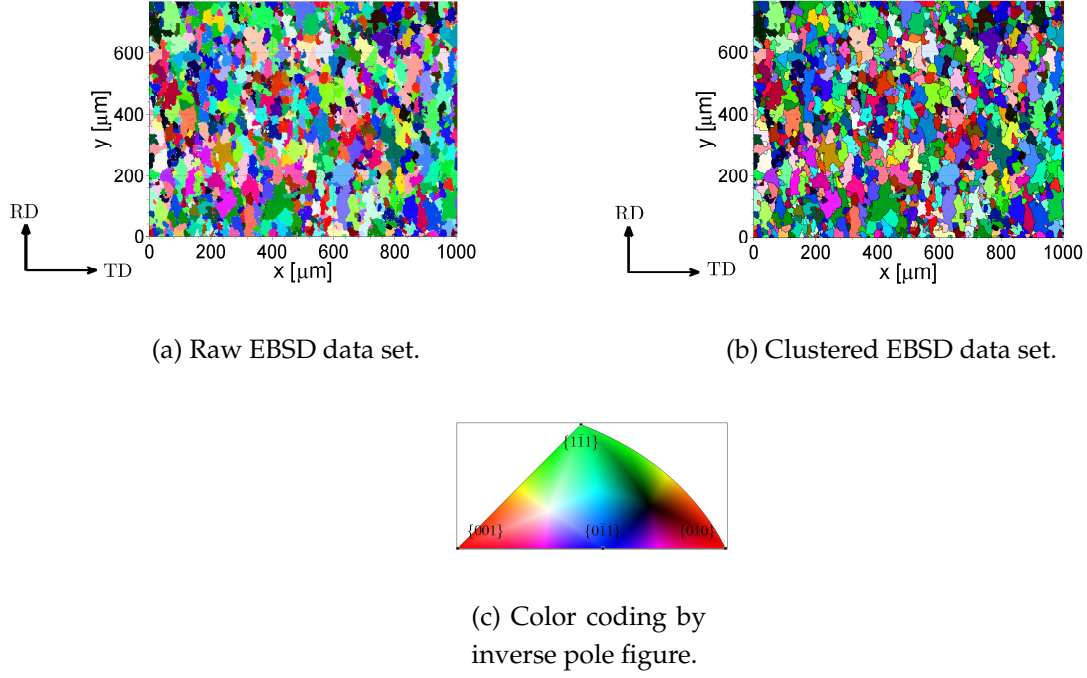


Figure 3.5: Microstructural EBSD images of the heat treated DC04 steel.

rotations characterized by three orthogonal matrices with respect to the orthonormal crystal lattice vectors  $\{g_i\}$  ( $i = 1 \dots 3$ ) are given by

$$\mathbf{R}_1(180^\circ) = \begin{bmatrix} 1 & 0 & 0 \\ 0 & -1 & 0 \\ 0 & 0 & -1 \end{bmatrix}, \quad (3.6)$$

$$\mathbf{R}_2(180^\circ) = \begin{bmatrix} -1 & 0 & 0 \\ 0 & 1 & 0 \\ 0 & 0 & -1 \end{bmatrix}, \quad (3.7)$$

$$\mathbf{R}_3(180^\circ) = \begin{bmatrix} -1 & 0 & 0 \\ 0 & -1 & 0 \\ 0 & 0 & 1 \end{bmatrix}. \quad (3.8)$$

Each multiplication of an orthogonal rotation matrix  $\mathbf{R}_i$  ( $i = 1 \dots 3$ ) and each grain orientation  $\mathbf{Q}$ , given by  $\mathbf{R}_i\mathbf{Q}$  ( $i = 1 \dots 3$ ), generates an additional grain orientation. This means that the orthotropic orientation data set is four times larger than the initial set. Therefore, the orthotropic orientation data sets of the raw data (2554 grains) and the reduced data (200 grains) consist of 10216 and 800 orientations, respectively. The  $\{111\}$ ,  $\{100\}$  and  $\{110\}$  pole figures and the CODF of the orthotropic orientation data sets are shown in Figures 3.8 and 3.9. It can be observed that there is no significant difference between the original and reduced data sets.

## The Crystallite Orientation Distribution Function (CODF)

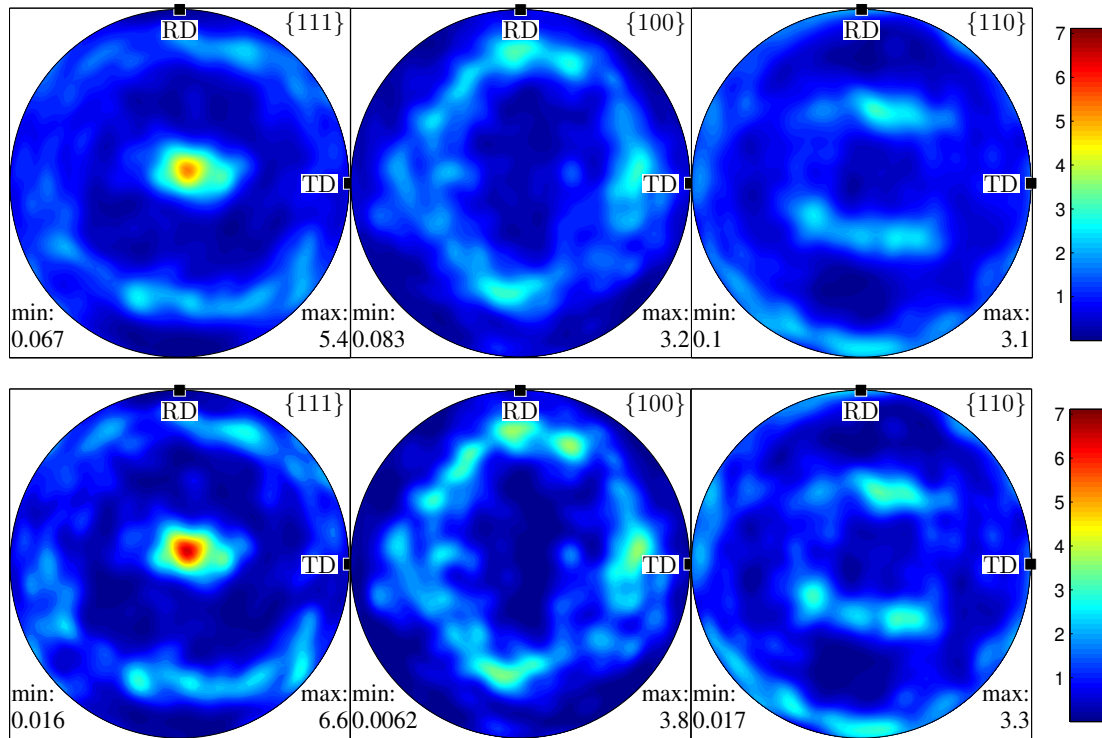


Figure 3.6: Comparison between pole figures of 2554 grains (above) and 200 grains (below).

### 3.2.2 EBSD Measurement for Subsequent Tensile Deformations

In this subsection, an experimental tensile specimen of heat treated DC04 steel by Project A6 is discussed. The specimen geometry is  $w = 5$  mm width,  $L_0 = 15$  mm gauge length and  $t = 1$  mm thickness. From such specimen, a tiny sample was cut by laser rays with the same thickness. Through the EBSD technique in the scanning electron microscope, an initial raw database of such a sample is obtained and shown in Table 3.4. The EBSD sample database is then imported into the MTEX toolbox to identify the corresponding microstructure. Figure 3.10 shows an EBSD sample microstructure considered at the initial state. A strain rate of  $10^{-3} \text{ s}^{-1}$  is applied to the tensile specimen in loading direction. During the tensile test, several EBSD databases have been determined experimentally and, thereby, the evolution of the crystallographic texture is measured at different elongation states (5%, 10%, 15%, 20%).

By using the MTEX toolbox, these raw EBSD databases are imported to obtain two-dimensional images of grain structures. Two microstructural images of both the raw EBSD data and the clustered EBSD data are shown in Fig. 3.11a and 3.11b, respectively, for the initial state of the sample. The grains consisting only of one pixel are eliminated in the clustering process of the MTEX toolbox. A clustered EBSD

### The Crystallite Orientation Distribution Function (CODF)

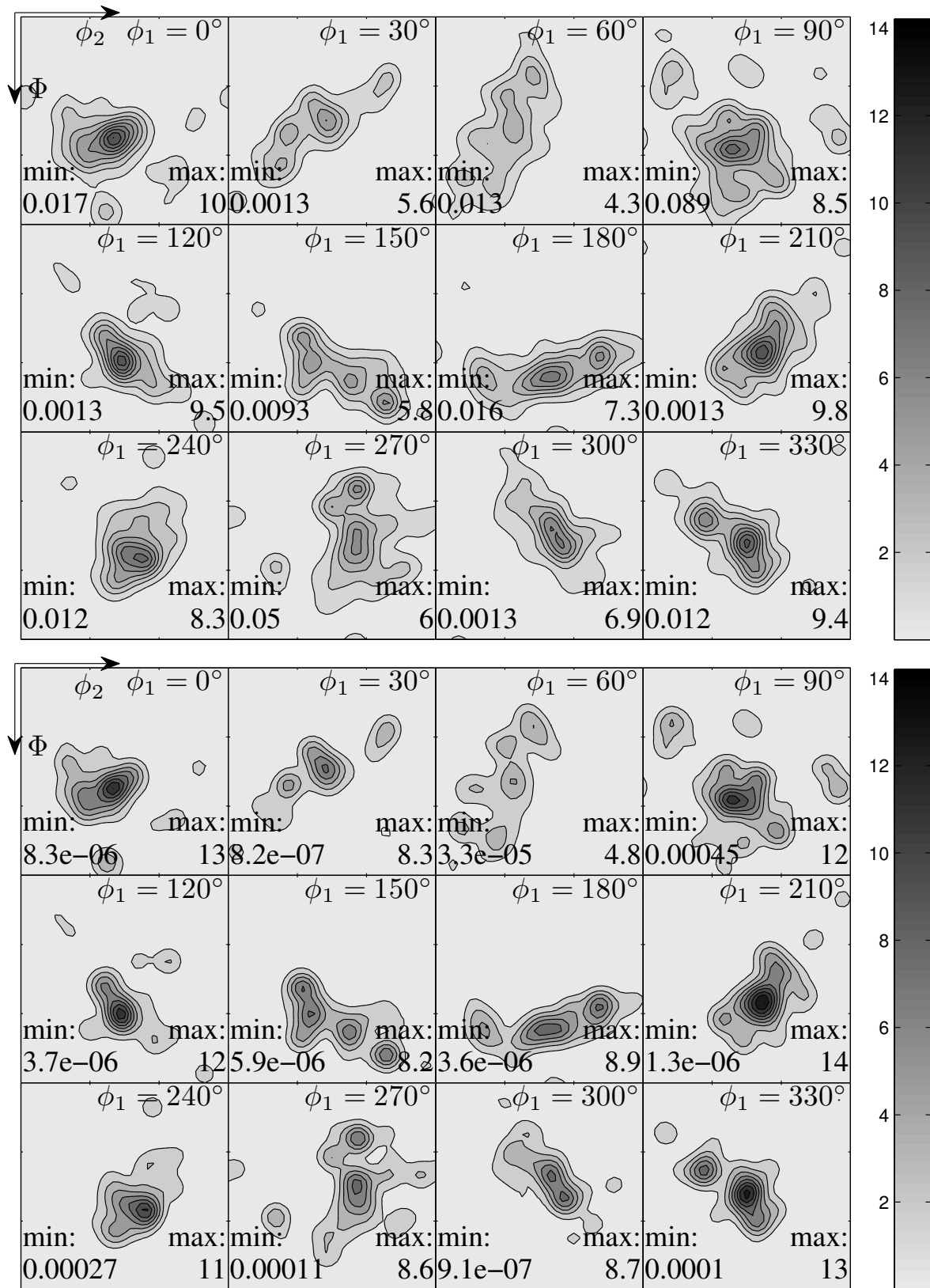


Figure 3.7: Crystallite orientation distribution function: (above) 254 grains and (below) 200 grains.

## The Crystallite Orientation Distribution Function (CODF)

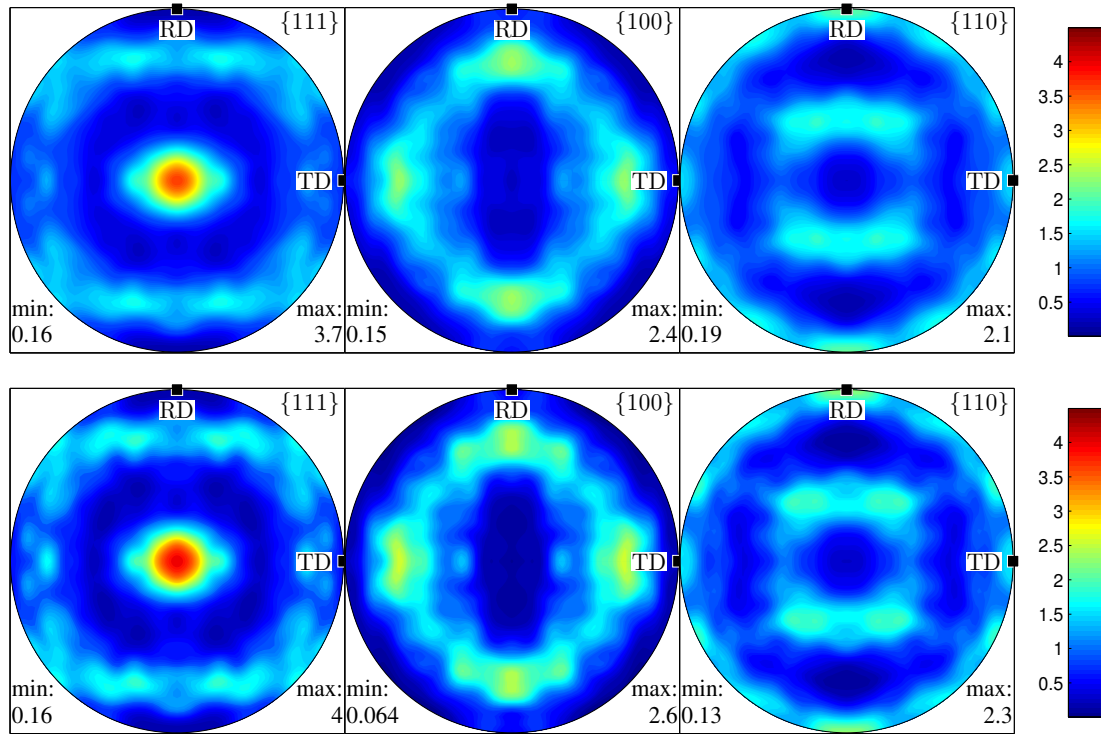


Figure 3.8: Comparison between pole figures of 2554 grains (above), 200 grains (below) additionally assuming orthotropic sample symmetry.

database consists of identified grains and corresponding point sets (Table 3.5). The first and second column are the X- and Y-position of the measurement points in  $\mu\text{m}$ . Three Euler angles are given by the third, fourth and fifth column, respectively in degree. The sixth column indicates the grain to which the measurement points belong. The order numbering of grains and the identification of 574 grains are shown in Fig. 3.12 at the initial state. Additionally, two-dimensional images of the raw EBSD data at different strain states (5%, 10%, 15% and 20%) are shown in Fig. 3.13. Based on the inverse pole figure (Figure 3.11c), each color indicates the lattice orientation in each grain at different states.

Some conclusive descriptions of the raw EBSD data are summarized. In the raw EBSD database of the initial state, the total number of columns and rows is 7 and 105000, respectively. After neglecting measurement errors, in such an EBSD database remain 103671 rows (or the number of pixels) and 7 columns. The number of measurement errors is 1329 pixels, i.e. approximately 1.26% of the area fraction. The map size of the raw grain structure in Fig. 3.11a is  $349 \times 299 \mu\text{m}$ . The area of one measurement point is  $1 \mu\text{m}^2$ . For the subsequent strain states, the measurement errors correspond to area fractions of 3.6%, 8.5%, 9.4% and 18.5%, respectively.

### The Crystallite Orientation Distribution Function (CODF)

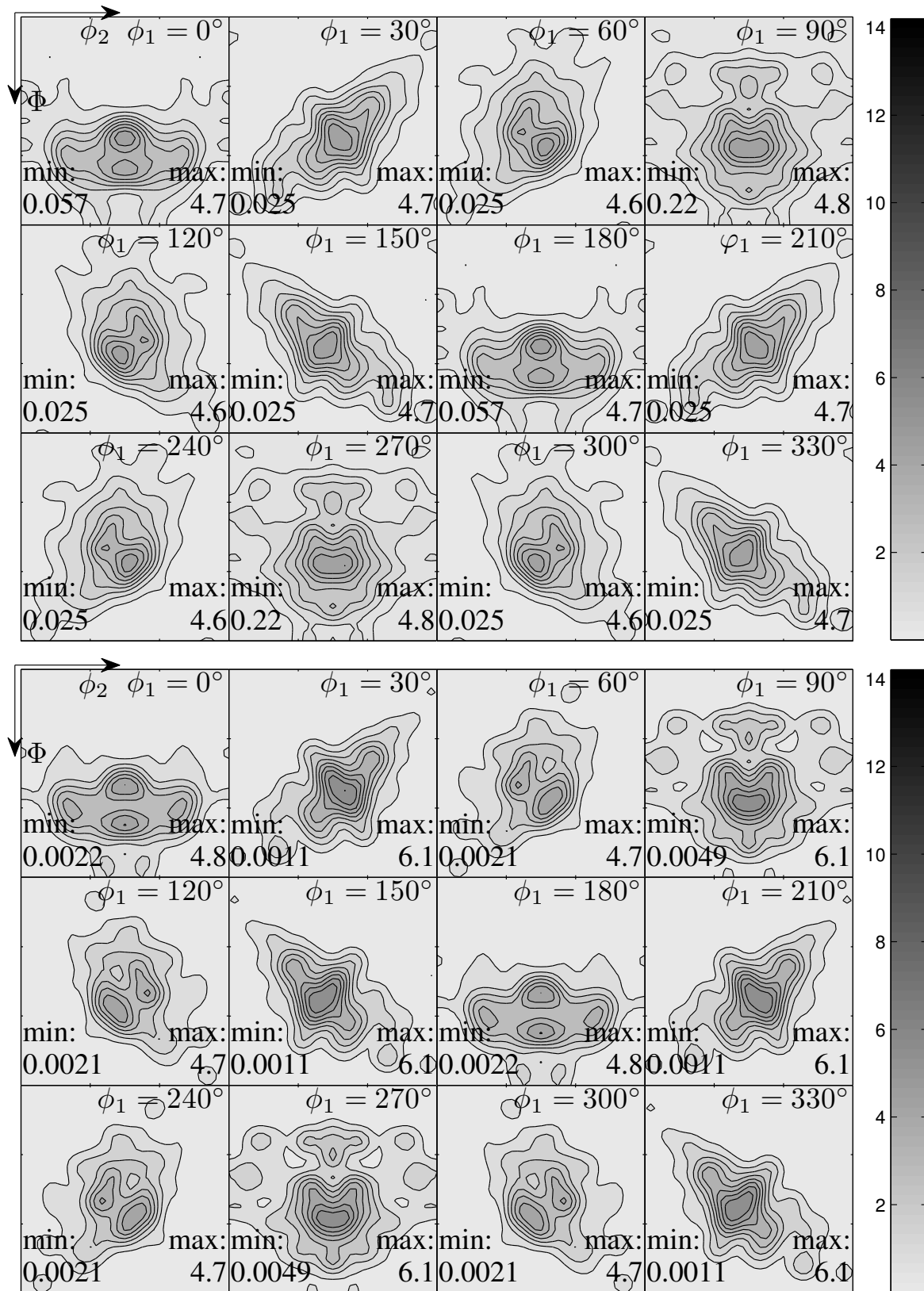


Figure 3.9: Crystallite orientation distribution function: (above) 2554 grains, (below) 200 grains additionally assuming orthotropic sample symmetry.

## The Crystallite Orientation Distribution Function (CODF)

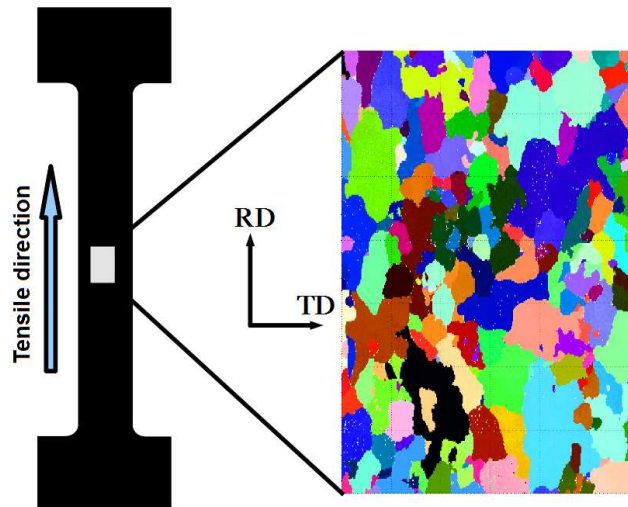
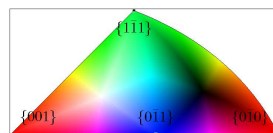
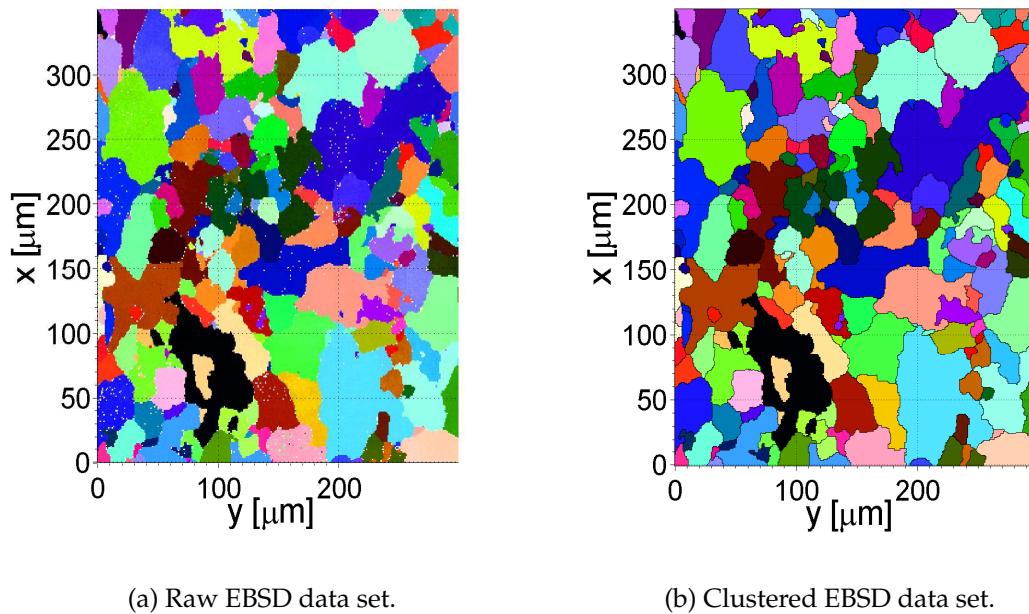


Figure 3.10: Raw EBSD microstructural image of a heterogeneous sample cut parallel to rolling direction from a DC04 steel specimen at the initial state.



(c) Color coding by inverse pole figure.

Figure 3.11: Microstructural images at the initial state.

## The Crystallite Orientation Distribution Function (CODF)

Phase	X	Y	Euler1	Euler2	Euler3	MAD
1	0	0	184.51	22.500	16.151	0.4142
1	1	0	184.81	22.407	16.002	0.1691
1	2	0	184.99	22.424	15.822	0.2642
1	3	0	184.82	22.371	16.024	0.2763
1	4	0	184.84	22.457	15.944	0.1761
⋮	⋮	⋮	⋮	⋮	⋮	⋮
⋮	⋮	⋮	⋮	⋮	⋮	⋮
⋮	⋮	⋮	⋮	⋮	⋮	⋮
1	34	166	202.47	48.141	56.847	0.5488
1	35	166	202.00	47.884	57.172	0.3646
1	36	166	202.65	48.037	56.935	0.5320
⋮	⋮	⋮	⋮	⋮	⋮	⋮
⋮	⋮	⋮	⋮	⋮	⋮	⋮
⋮	⋮	⋮	⋮	⋮	⋮	⋮
1	347	299	202.91	40.299	63.507	0.4714
1	348	299	202.76	40.259	63.498	0.2761
1	349	299	203.03	40.184	63.403	0.5137

Table 3.4: File format of the raw EBSD data set of the experimental sample at the initial state including 105000 rows and 7 columns (experiment by Project A6).

### 3.3 Identification of Texture Components based on EBSD Data

A general technique to significantly reduce the number of crystal orientations is presented in this section. In several studies (see, e.g., Nakamachi et al. (2001); Zhao et al. (2001); Xie and Nakamachi (2002); Raabe et al. (2002); Böhlke et al. (2006); Gao et al. (2006)), special techniques have been developed to determine the number of texture components based on experimental data.

Nakamachi et al. (2001); Xie and Nakamachi (2002) investigated three kinds of BCC steel sheets, mild steel, dual phase steel and high strength steel. Their crystal orientations were obtained by X-ray diffraction. The crystal orientations were assigned into a FE-model by using the orientation probability assignment method. One FE integration point corresponds to one orientation, which can reorientate individually during the deformation. This method emphasized that if sufficient numbers of FE integration points are used to represent real textures of the sheet metals, it can automatically identify the initial and evolutionary plastic anisotropy. However, the

### The Crystallite Orientation Distribution Function (CODF)

X	Y	Euler1	Euler2	Euler3	Grain
0	0	-175.23	22.552	16.012	60
1	0	-175.23	22.552	16.012	60
2	0	-175.23	22.552	16.012	60
⋮	⋮	⋮	⋮	⋮	⋮
⋮	⋮	⋮	⋮	⋮	⋮
⋮	⋮	⋮	⋮	⋮	⋮
9	0	-1.5371	34.919	41.736	129
10	0	-1.5371	34.919	41.736	129
11	0	-1.5371	34.919	41.736	129
⋮	⋮	⋮	⋮	⋮	⋮
⋮	⋮	⋮	⋮	⋮	⋮
⋮	⋮	⋮	⋮	⋮	⋮
59	0	-12.043	33.24	17.91	148
60	0	-12.043	33.24	17.91	148
61	0	-12.043	33.24	17.91	148
⋮	⋮	⋮	⋮	⋮	⋮
⋮	⋮	⋮	⋮	⋮	⋮
⋮	⋮	⋮	⋮	⋮	⋮
347	299	-157.02	40.197	63.434	574
348	299	-157.02	40.197	63.434	574
349	299	-157.02	40.197	63.434	574

Table 3.5: The clustered EBSD data set (without erroneous measurement points) of the experimental sample at the initial state, including 103671 rows and 6 columns.

main drawback of the approach is the extensive calculation time.

Therefore, a general way to reduce the degrees of freedom of crystal plasticity FE-models is the use of texture components, introduced by Zhao et al. (2001); Raabe et al. (2002); Böhlke et al. (2006); Schulze et al. (2009) based on the basic researches of Bunge (1993) and Helming (1996).

Instead of using large sets of discrete grain orientations, Zhao et al. (2001); Raabe et al. (2002) used small sets of discrete texture components. Only a few texture components are required to represent the complete texture. The approach constitutes a significant improvement with respect to the computation time. In addition, Raabe et al. (2002) suggested another approach using the crystal orientations by scattering around the mean orientations of the texture components in order to take into account the scattering of the crystallites around the ideal components. However, if the texture components

### The Crystallite Orientation Distribution Function (CODF)

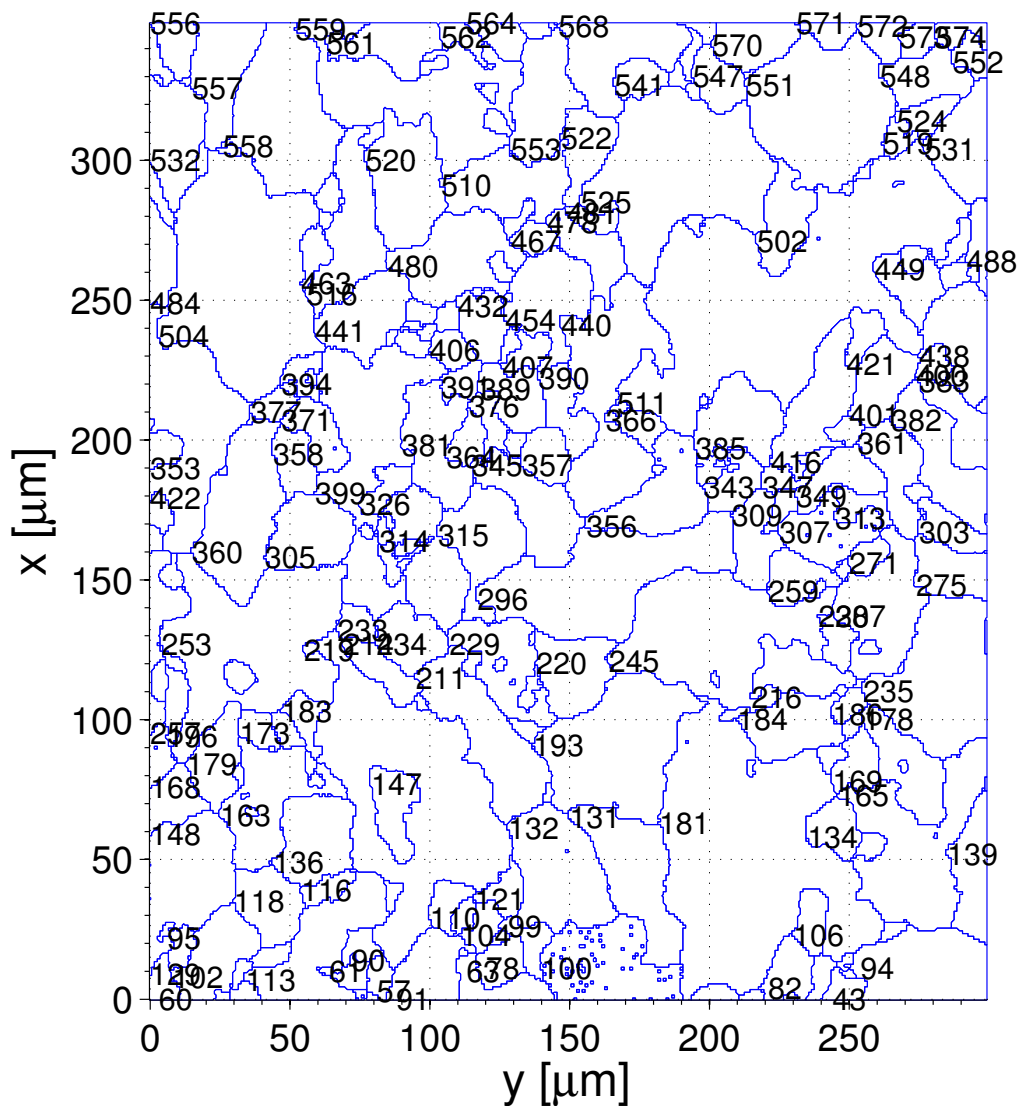


Figure 3.12: Identification and numbering of 574 grains in the microstructural image of clustered data set at the initial state.

were modeled in such suggested way, the prediction of the plastic anisotropy is significantly overestimated.

In contrast, Böhlke et al. (2005) presented an approach allowing for significant reduction of the number of crystal orientations. The approach takes into account the half-width of the texture components which are described by Mises-Fischer distributions during the computation of the stresses. Another approach by Böhlke et al. (2006) suggested to model the gray texture by an isotropic texture component given by the isotropic plasticity model and a related volume fraction. The approach gave good results, but the evolution of the volume fraction of the isotropic texture component is difficult to model.

In the work of Schulze et al. (2009), the Taylor assumption is combined with a

## The Crystallite Orientation Distribution Function (CODF)

rate-independent pencil glide deformation model on the micro-scale. By a combination of a texture approximation procedure and a conventional parameter identification scheme, a low-dimensional description of the texture is obtained. The hardening on the micro-scale is described by a phenomenological hardening law. Nevertheless, the limitation is figured out that a small group of crystals with volume fractions is used, which are not equally distributed. This issue can lead to an overestimation of the influence of certain crystals on the overall behavior. Generally, FE computations based on polycrystal models are numerically too expensive if the applied crystallographic texture is approximated by several thousand discrete crystal orientations at the integration points. Additionally, the polycrystal models based on a small number of discrete crystal orientations have the disadvantage that the anisotropy may be significantly overestimated. This section aims to apply an effective method, see, e.g. Gao et al. (2006), Jöchen and Böhlke (2011), to create a low-dimensional description for the arbitrary texture.

Conceptually, if the grain orientation is known in the form of a rotational matrix  $\mathbf{Q}$ , the angle of rotation  $\omega$  and the corresponding normalized vector  $\mathbf{n}$  specifying the rotational axis can be determined. The angle of rotation is computed by

$$\cos(\omega) = \frac{\text{tr}(\mathbf{Q}) - 1}{2}, \quad (3.9)$$

and the normalized vector is given by

$$\mathbf{n} = \frac{(Q_{23} - Q_{32})\mathbf{e}_1 + (Q_{31} - Q_{13})\mathbf{e}_2 + (Q_{12} - Q_{21})\mathbf{e}_3}{\sqrt{(Q_{23} - Q_{32})^2 + (Q_{31} - Q_{13})^2 + (Q_{12} - Q_{21})^2}}. \quad (3.10)$$

The orientation space or Euler space is conventionally limited:

$$\begin{aligned} \mathbf{Q} : [K_A \rightarrow K_B] \text{ or } \mathbf{Q}^{-1} = \mathbf{Q}^T : [K_B \rightarrow K_A] \\ \text{Space } \mathcal{G} : 0 \leq \phi_1, \phi_2 \leq 2\pi; \quad 0 \leq \Phi \leq \pi \\ (\mathbf{Q} = \{\phi_1, \Phi, \phi_2\}); \text{ in Bunge's Euler angles.} \end{aligned} \quad (3.11)$$

Considering the cubic crystal symmetry, there are 24 different ways in which a crystal could be arranged using proper rotational symmetry operators. Therefore, there are 24 crystallographically equivalent solutions for an orientation (Randle, 2000; Cho et al., 2005). In this case of a triclinic lattice, a family including 24 rotations with respect to 24 triples  $(\phi_1, \Phi, \phi_2)$  is given by Humbert et al. (1992); Bradley and Cracknell (1972), and summarized in Appendix A. Due to the crystal symmetry, only a triple is taken into account in the reduced Euler space named the fundamental zone (FZ) and described by Gao et al. (2006) (see Fig. 3.14).

## The Crystallite Orientation Distribution Function (CODF)

The limits of the cubic fundamental zone are given by

$$\phi_1 \in [0, 2\pi) \quad (3.12)$$

$$\Phi \in [f(\phi_2), \pi/2] \quad (3.13)$$

$$\phi_2 \in [0, \pi/4) \quad (3.14)$$

$$f(\phi_2) = \arccos \left( \frac{\cos(\phi_2)}{\sqrt{1 + \cos(\phi_2)^2}} \right). \quad (3.15)$$

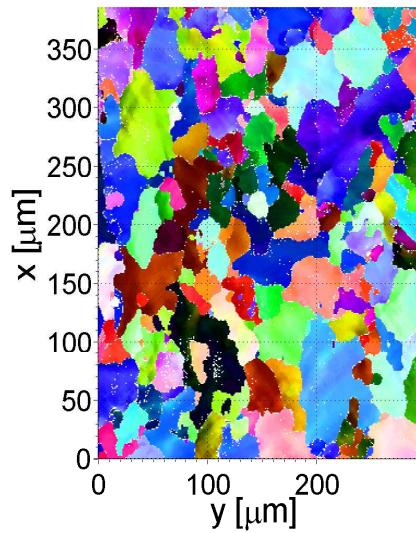
As explained in the work of Gao et al. (2006) and extended in an algorithm by Jöchen and Böhlke (2011), the cubic fundamental zone is partitioned by a discrete number of boxes  $B_i$  ( $i = 1 \dots N$ ). The volume fraction of one box can be defined as follows

$$V(B_i) = \frac{1}{8\pi^2 N} \iiint_{FZ} \sin(\Phi) d\phi_1 d\Phi d\phi_2, \quad \text{for } 1 \leq i \leq N. \quad (3.16)$$

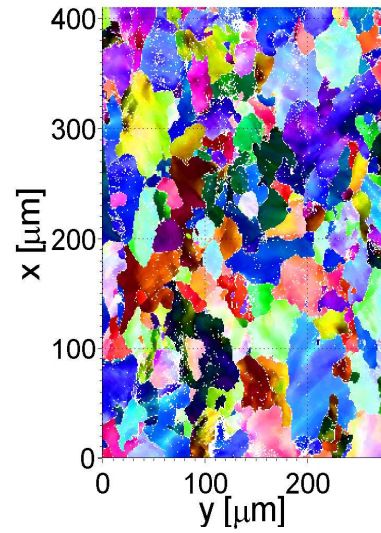
In this mathematical technique, Euler angle ranges are subdivided in the fundamental zone, by  $\mathcal{I}$ ,  $\mathcal{J}$  and  $\mathcal{K}$  subdivisions, respectively. The product  $N = \mathcal{I}\mathcal{J}\mathcal{K}$  is the total number of boxes in the fundamental zone. By using the reduction algorithm, the scheme for the aforementioned heat treated EBSD data set of DC04 steel specimen (Table 3.3), including 2554 grains, is reduced to 216 boxes, shown in Fig. 3.15, where the  $\phi_1$ -range is divided into 24 subdivisions ( $\mathcal{I} = 24$ ) and the  $\Phi$ - and the  $\phi_2$ -range are each divided into 3 subdivisions ( $\mathcal{J} = \mathcal{K} = 3$ ). Finally, the total number of texture components remains 212, since four boxes are empty and do not contain any orientation data. In order to verify the texture component data set, their pole figures should be compared to the ones of the original (2554 grains) and reduced (200 grains) orientation data sets. A comparison of pole figures with respect to these different grain orientation data sets is shown in Fig. 3.16. All pole figures are evaluated by the Matlab toolbox MTEX. It can be noticed that the difference between pole figures is not significant. In addition, the orthotropic data set of the texture component data is obtained by using the aforementioned symmetrization technique in Section 3.2.1.

As observed in Fig. 3.17, the pole figures of the orthotropic texture component data set (848 texture components) are quite similar to the ones of the orthotropic raw orientation data set ( $2554 \times 4$  grains) and the orthotropic reduced orientation data set ( $200 \times 4$  grains).

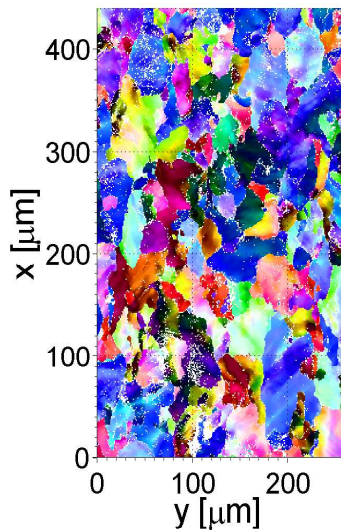
## The Crystallite Orientation Distribution Function (CODF)



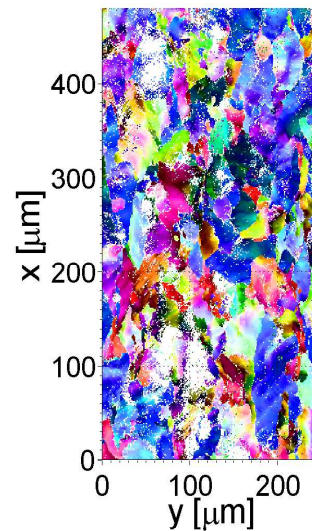
(a) 5% elongation.



(b) 10% elongation.



(c) 15% elongation.



(d) 20% elongation.

Figure 3.13: Microstructural images of raw EBSD data sets (experiment by Project A6, GRK1483) at different states.

## The Crystallite Orientation Distribution Function (CODF)

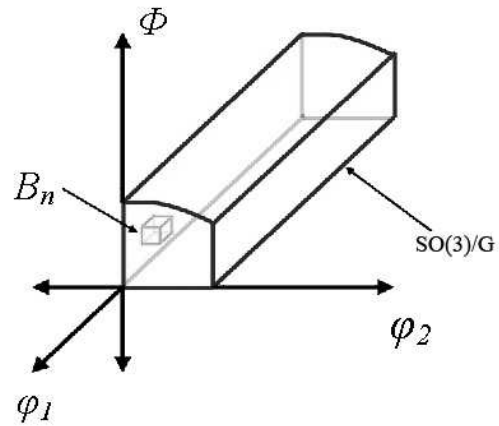


Figure 3.14: The cubic fundamental zone in the conventional Euler space (Gao et al., 2006).

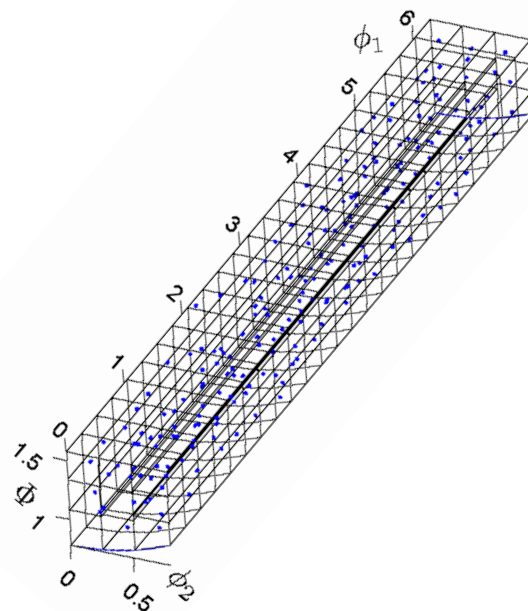


Figure 3.15: Reduced heat treated data set using  $\mathcal{K} = 3$ , represented by the fundamental zone partitioned by 216 boxes in 3D space, the unit of Euler angles [radian].

## The Crystallite Orientation Distribution Function (CODF)

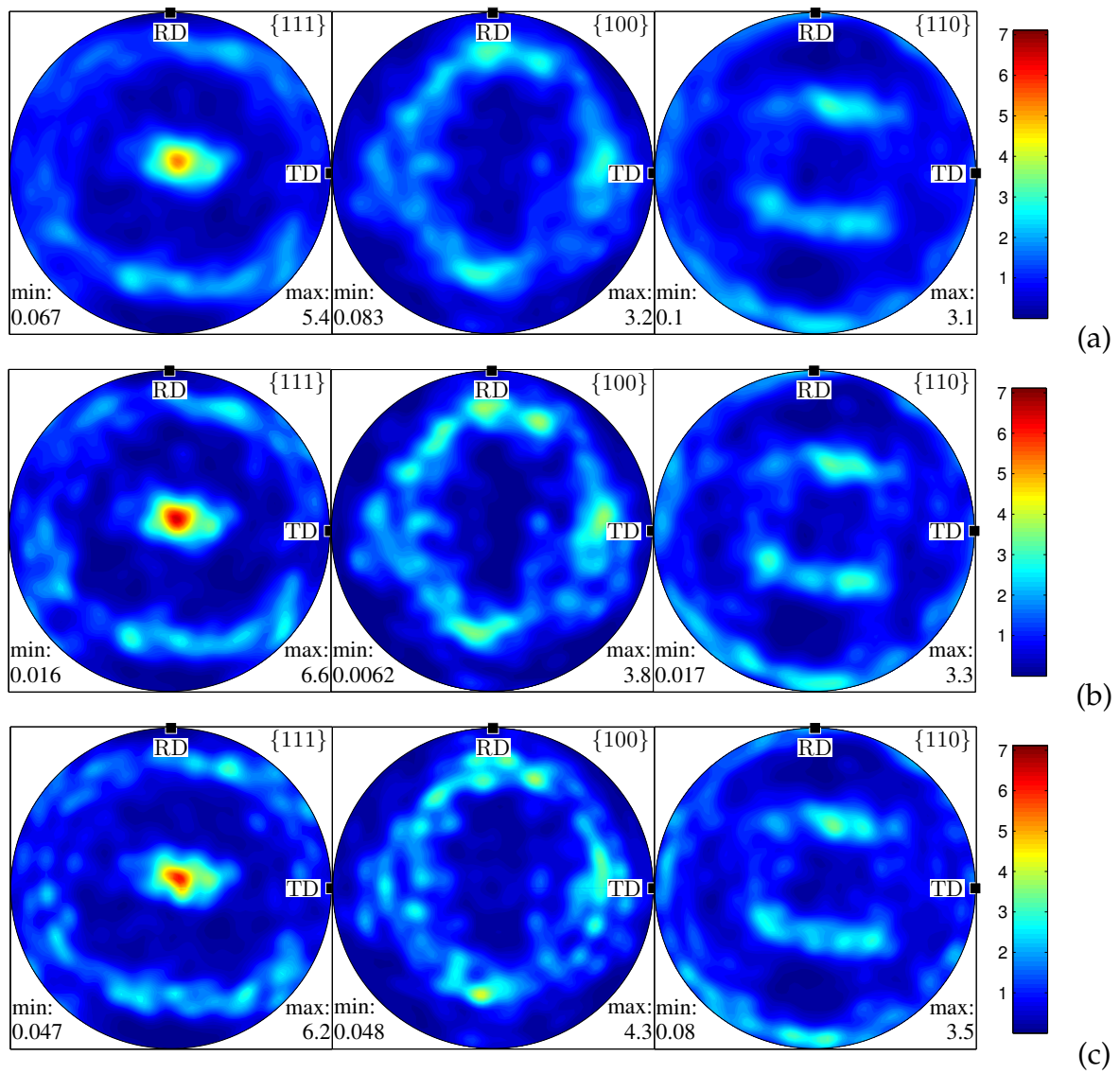


Figure 3.16: Comparison between pole figures of (a) 2554 grains, (b) 200 grains and (c) 212 texture components.

## The Crystallite Orientation Distribution Function (CODF)

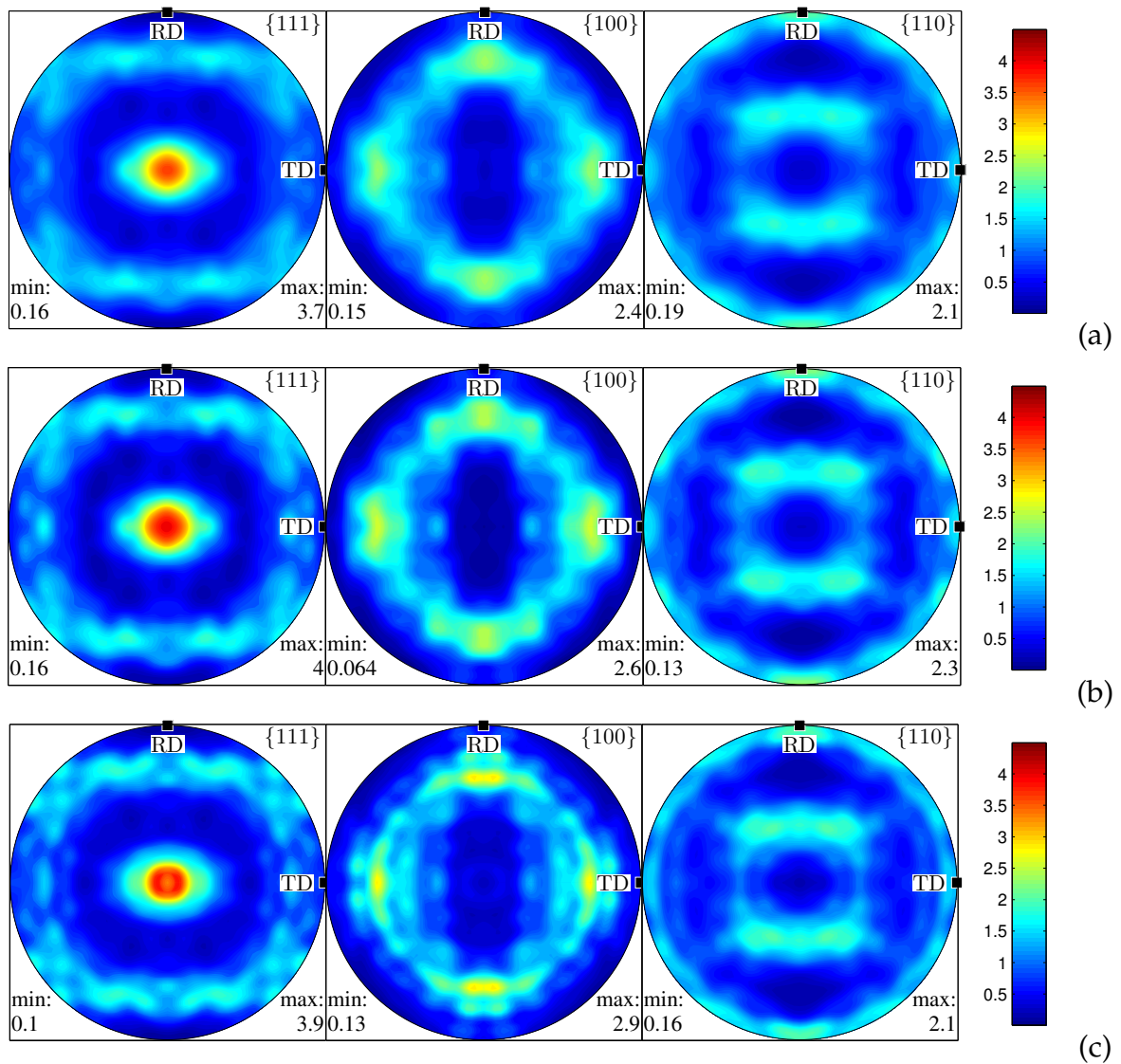


Figure 3.17: Comparison between pole figures of (a) 2554 grains, (b) 200 grains, (c) 212 texture components additionally assuming orthotropic sample symmetry.

# Chapter 4

## Estimation of Material Parameters

### 4.1 Estimation of Material Parameters based on Tensile Test Experiments

#### 4.1.1 Experimental Data of Tensile Tests

This section aims to identify the material parameters used in the micromechanical model of DC04 steel based on uniaxial tensile tests. A specimen is cut from a heat treated sheet metal of a DC04 steel at different angles to the rolling direction (RD). Two different uniaxial tensile experiment series are used to investigate the macroscopic stress-strain relation. The two series of experiments have been performed by IAM-WBM (Project A6) and the Institute of Forming Technology and Lightweight Construction (IUL, Technical University of Dortmund).

In the experiments of Project A6, the initial thickness of the specimen is  $t_0 = 1$  mm with  $L_0 = 15$  mm gauge length and  $w_0 = 5$  mm width. Three tensile data sets are identified for specimens oriented at  $0^\circ$ ,  $45^\circ$  and  $90^\circ$  to RD. These experiments contain information of the displacements and the forces over time. The nominal stress is calculated by  $\sigma_0 = F/A_0$ , where  $F$  is the force and  $A_0 = t_0 w_0$  is the initial area of the cross section. The engineering strain is given by  $\varepsilon = L(t)/L(0) - 1 = \Delta L(t)/L(0)$ . Fig. 4.1 shows the nominal stress versus the engineering strain for differently oriented specimens.

In the experimental data of IUL (Dortmund), several data sets are identified for specimens oriented at  $0^\circ$ ,  $15^\circ$ ,  $30^\circ$ ,  $45^\circ$ ,  $60^\circ$ ,  $75^\circ$  and  $90^\circ$  to the RD. The initial thickness of the specimen varies in the range  $t_0 = 1.16 - 1.2$  mm with a gauge length  $L_0 = 80$  mm and the range  $w_0 = 19.81 - 19.92$  mm. Fig. 4.2 shows the tensile nominal stress versus the engineering strain for the differently oriented specimens. The tests were conducted at the constant velocity of  $0.0025 \text{ s}^{-1}$ .

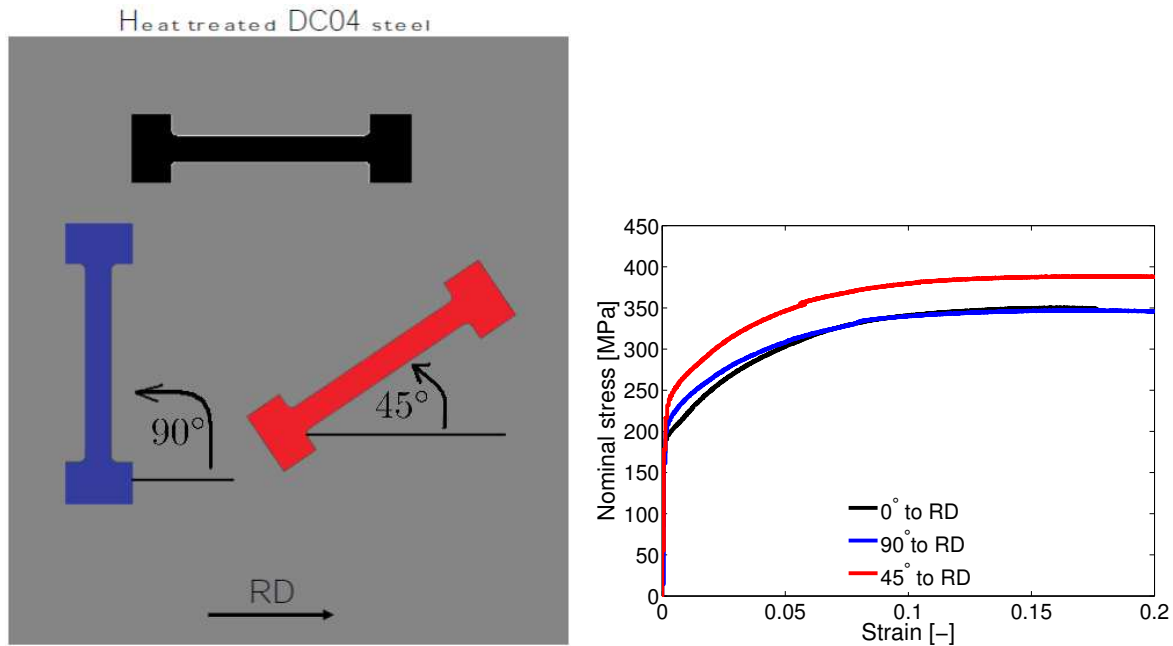


Figure 4.1: (left) Tensile specimen at different angles to RD and (right) experimental stress-strain curves for different angles to RD (experiment by Project A6) - 0°, 45°, 90° to RD.

#### 4.1.2 FE Modeling and Simulation of Tensile Tests

A finite element model for modeling the tensile tests is created by ABAQUS and the Taylor type polycrystal model is applied at the integration points of the finite element. The mechanical constitutive law discussed in Chapter 2 is implemented numerically by a user defined subroutine UMAT (Manuals of SIMULIA, see, Abaqus/CAE (2009) and Böhlke et al. (2005)). The orthotropic orientation data set (800 grains) of the heat treated DC04 steel is used in the Taylor type polycrystal model as initial grain orientation distribution. The  $\{110\}\langle 111\rangle$  and  $\{112\}\langle 111\rangle$ , i.e. 24 slip systems  $\alpha = 1 \dots 24$  are used. In Figure 4.3, the finite element model is shown. It represents a representative element for the macroscopically homogeneous material. Stresses and strains are computed at the eight integration points within the FE-model. The length, the width and the area are 1 mm, 1 mm and 1 mm<sup>2</sup>, respectively. The initial time increment is 10<sup>-6</sup> s and the maximum time increment is 1 s. The total time in the simulations is 200 s corresponding to the final displacement of  $u_x = 0.2$ . As a result, the applied strain rate is 10<sup>-3</sup> s<sup>-1</sup>. Note that each rotation of the initial orientation data set about the normal direction  $e_3$  (ND) with angle  $\theta$  corresponds to the oriented specimen. The rotation matrix  $\underline{\underline{Q}}$  representing

## Estimation of Material Parameters

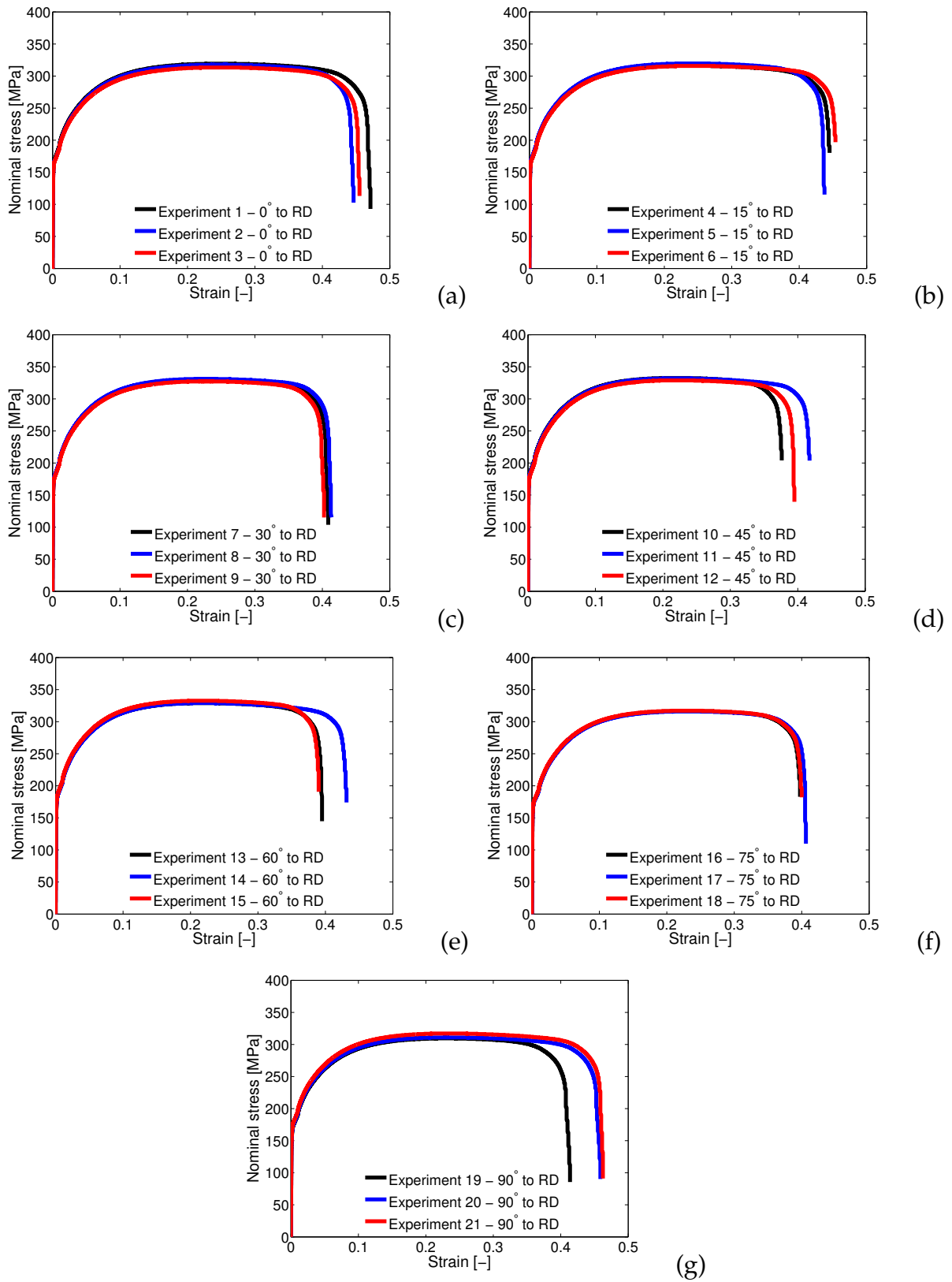


Figure 4.2: Uniaxial tensile stress-strain curves for specimen oriented at different angles to RD (experiment by IUL, Technical University of Dortmund): (a)  $0^\circ$ , (b)  $15^\circ$ , (c)  $30^\circ$ , (d)  $45^\circ$ , (e)  $60^\circ$ , (f)  $75^\circ$ , (g)  $90^\circ$ .

the rotation about  $e_3$ , can be expressed as follows

$$\underline{\underline{\Theta}}(\theta) = \begin{bmatrix} \cos(\theta) & -\sin(\theta) & 0 \\ \sin(\theta) & \cos(\theta) & 0 \\ 0 & 0 & 1 \end{bmatrix}. \quad (4.1)$$

Each tensile simulation for a fixed angle  $\theta$  is performed for the symmetrized orientation set. The nominal stress is computed by  $\sigma_0 = F/A_0$ , where  $F$  is the sum of computed forces at nodes along the tensile direction during deformation.

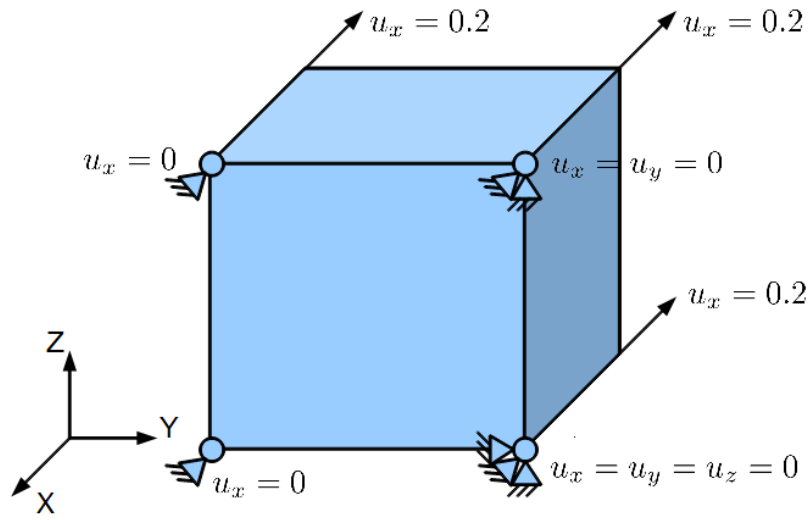


Figure 4.3: FE-model of the uniaxial tensile test with one finite element.

In this work, a set of material parameters needs to be estimated by comparing simulation results to experimental data. This will be done based on stress-strain curves and the least square fitting method. The elastic constants of DC04 steel used in tensile test simulations are given by Sudook and Ward (2007) (Table 4.1). The other material parameters, i.e., the reference slip rate  $\dot{\gamma}_0$ , the strain-rate sensitivity parameter  $m$ , the initial critical resolved shear stress  $\tau_0^C$ , the asymptotic critical resolved shear stress  $\tau_{V0}^C$ , and the initial hardening modulus  $\Theta_0$  are estimated based on the experimental stress-strain curves and are also given in Table 4.1. The values of the initial and asymptotic critical resolved shear stresses are estimated in the first step via the Taylor factor  $M \cong 3$  (see, e.g., U. F. Kocks (2000)) between the microscopic shear stress and the macroscopic nominal stress

$$\tau_0^C \cong \frac{\sigma_0^{macro}}{M} \Big|_{\theta=0^\circ}, \quad \tau_{V0}^C \cong \frac{\sigma_\infty^{macro}}{M} \Big|_{\theta=0^\circ}, \quad (4.2)$$

where the macroscopic nominal stresses  $\sigma_0^{macro}$  and  $\sigma_\infty^{macro}$  can be estimated from the experimental tensile curves. These two microscopic shear stresses and the hardening

$C_{1111}$ [GPa]	$C_{1122}$ [GPa]	$C_{1212}$ [GPa]
231.5	135.0	116.0

Elastic constants of DC04 steel (Sudook and Ward, 2007).

$m$ [-]	$\dot{\gamma}_0$ [s <sup>-1</sup> ]	$n$ [-]
20	0.001	5

Material parameters in flow rule.

$\tau_0^C$ [MPa]	$\tau_{V0}^C$ [MPa]	$\Theta_0$ [MPa]
73	133	860

Modeled hardening parameters.

Table 4.1: Set of material parameters based on the experimental tensile tests of Project A6.

modulus  $\Theta_0$  are then adjusted to fit to the experimental curves for all different angles  $\theta$ . The least square method is applied in order to determine the optimal parameters. The error is defined by

$$E_2 = \sqrt{\frac{1}{n} \sum_{i=1}^n d_i^2} = \sqrt{\frac{1}{n} \sum_{i=1}^n |P_i^{exp} - P_i^{num}|}, \quad (4.3)$$

where  $n$  is the number of data points.  $d_i$  is the distance between the experimental data point  $P_i^{exp}$  and simulated data point  $P_i^{num}$  with respect to the same strain. Table 4.1 shows the set of optimal material parameters based on the minimization of  $E_2$  for all tensile directions simultaneously. The corresponding stress-strain curves are shown in Fig. 4.4. By using this optimal set, the comparison between the numerical and experimental results for the oriented specimen at different angles to RD is depicted in Fig. 4.5.

At IUL (TU Dortmund), for each tensile direction three tensile experiments have been performed. A mean stress-strain curve is obtained based on these three experimental curves. At a fixed angle to RD, the numerical stress-strain curve is compared to the corresponding mean curve based on the minimization of the aforementioned error mean  $E_2$ . The range of strain 0–0.2 is considered to estimate the optimal set of material parameters. In Fig. 4.6, computed nominal stress-strain curves are compared to the experimental curves. The set of material parameters determined again by a least square method is shown in Table 4.2.

In the following investigation, a mean parameter set is used which estimates the stress-strain behavior of the given experimental data (see Table 4.3).

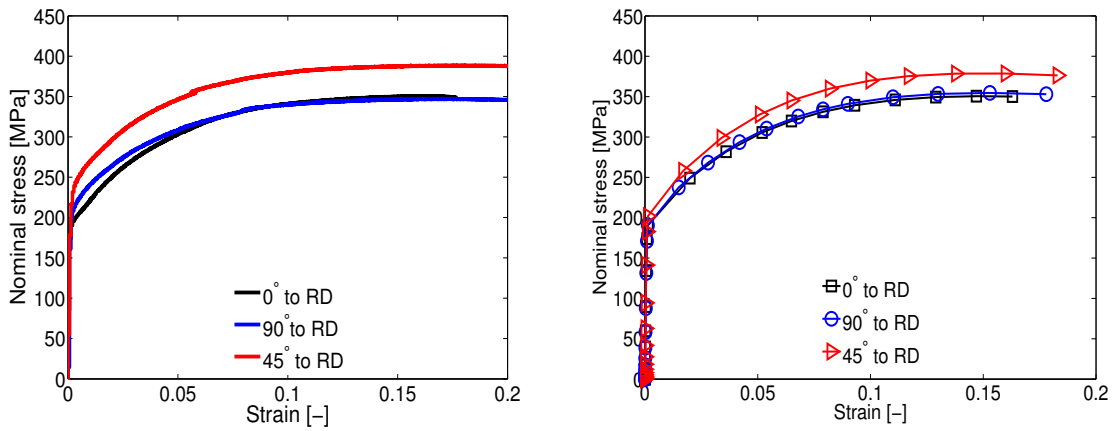


Figure 4.4: Curves of tensile test experiments given by Project A6 (left) and simulations with  $\{110\}\langle 111 \rangle + \{112\}\langle 111 \rangle$  slip systems (right).

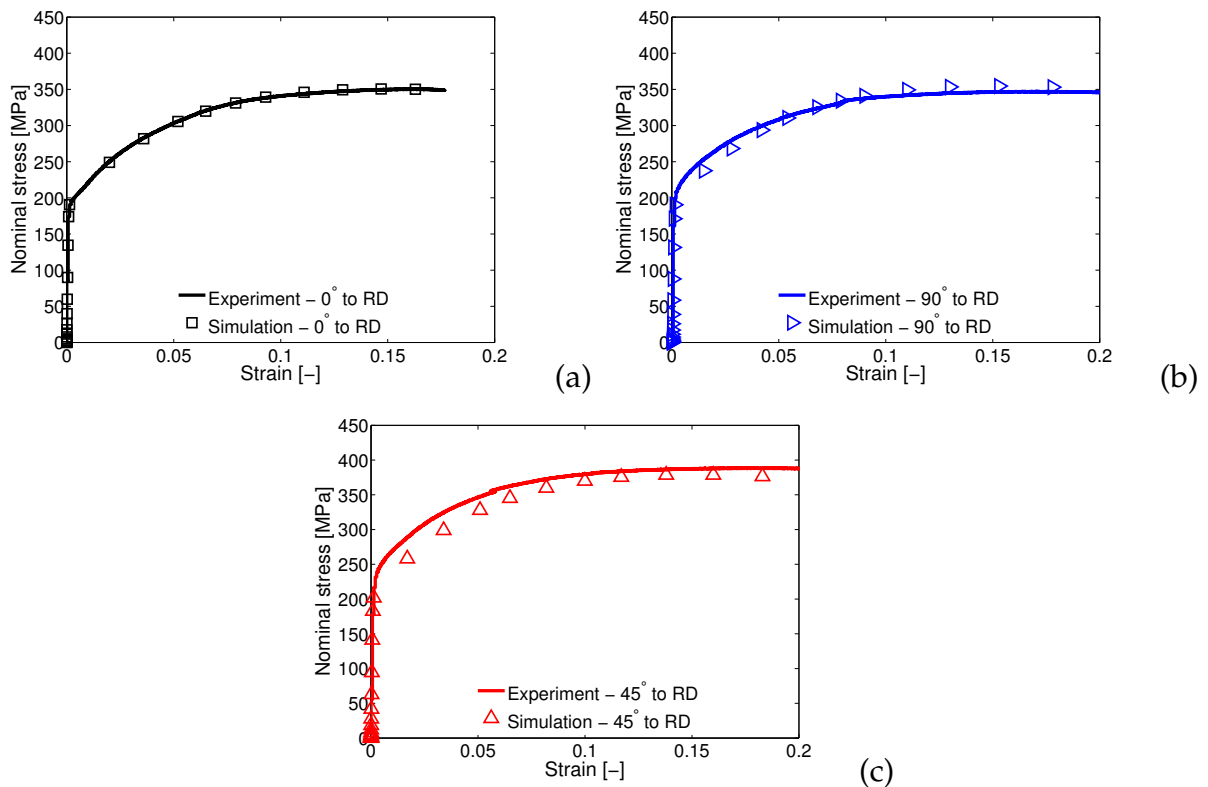


Figure 4.5: Numerically determined stress-strain curves with the optimal set of material parameters in comparison to experimental stress-strain curves (Project A6) for different angles to RD - (a)  $0^\circ$ , (b)  $90^\circ$ , (c)  $45^\circ$ .

## Estimation of Material Parameters

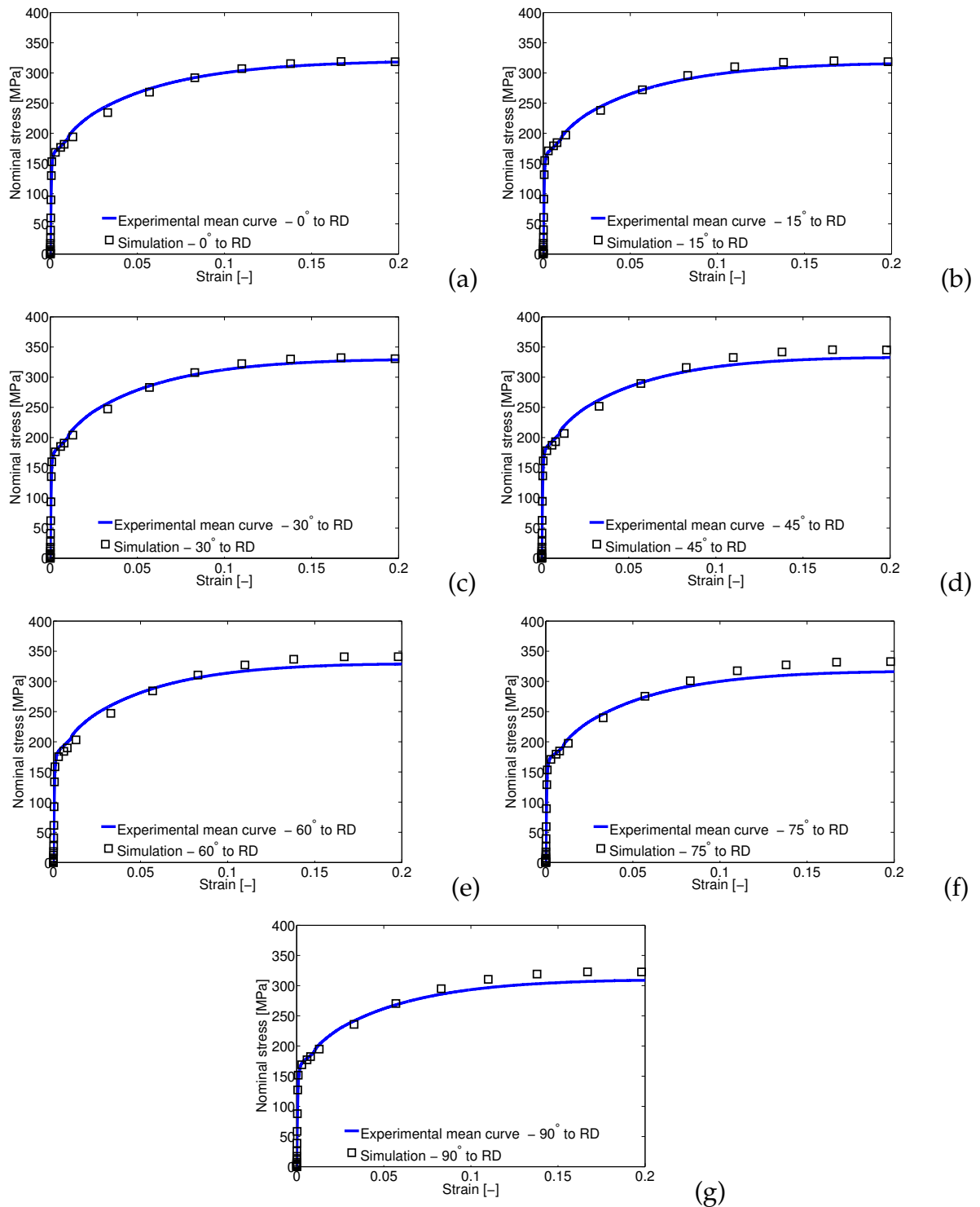


Figure 4.6: Numerically determined stress-strain curves in comparison to experimental data of IUL (TU Dortmund) for different angles to RD - (a)  $0^\circ$ , (b)  $15^\circ$ , (c)  $30^\circ$ , (d)  $45^\circ$ , (e)  $60^\circ$ , (f)  $75^\circ$ , (g)  $90^\circ$ .

$\tau_0^C$ [MPa]	$\tau_{V0}^C$ [MPa]	$\Theta_0$ [MPa]
61	127	650

Table 4.2: Modeled hardening parameters based on the experimental tensile tests of IUL (Dortmund).

$\tau_0^C$ [MPa]	$\tau_{V0}^C$ [MPa]	$\Theta_0$ [MPa]
$67 \pm 6$	$130 \pm 3$	$755 \pm 105$

Table 4.3: A mean set of hardening parameters.

## 4.2 Estimation of Material Parameters based on Micro-pillar Experiments

### 4.2.1 Micro-pillar Compression Tests

Recently, a new approach has been introduced, based on a combination of Focused Ion Beam (FIB) machining and a simple extension of the nano-indentation technique (Uchic et al., 2004) to study the fundamental mechanical properties of materials. With FIB-milling, micro-pillars are carved out in the surface of a substrate material for the preparation of specimens. A modified nano-indentation system, fitted with a flat-end diamond indenter, is used to carry out the micro-compression tests, afterwards. The information of the load-displacement data are continuously recorded during the experiment as in a regular nano-indentation. Various micro-pillar compression tests were performed by Ni (Uchic et al., 2004; El-Awady et al., 2009), Au (Volkert and Lilleodden, 2006), Cu (Raabe et al., 2007; Kiener et al., 2009; Akarapu et al., 2010), Mo (Bei et al., 2007), Al (Senger et al., 2008), and Zr (Yang et al., 2009) single crystal micro-pillars of different diameters in the range of microns. The results of these experiments revealed a strong size-dependence on small-scale plasticity.

Raabe et al. (2007) and Kiener et al. (2009) performed crystal plasticity finite element simulations of cylindrical Cu single crystal compression tests (Fig. 4.8) and evaluated them with respect to the role of the initial crystal orientation, deformation-induced orientation changes, sample geometry (diameter-to-length ratio) and Coulomb friction of micro-pillar compression tests. It has been shown that there is no significant difference between rectangular and cylindrical sample geometry, that samples with larger values for the diameter-to-length ratio revealed higher orientation and shape stability during the compression, that non-zero friction conditions reduce shape instability regardless of the initial crystallographic orientation of the compressed

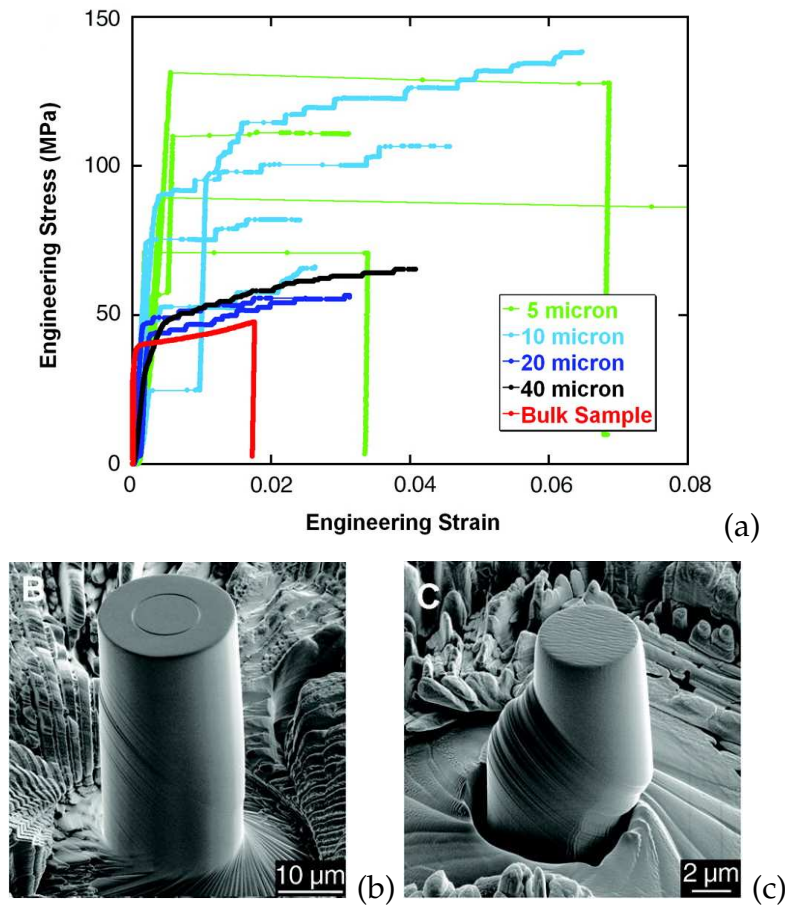


Figure 4.7: Mechanical behavior for pure Ni micro-samples having a  $\langle 134 \rangle$ -orientation, (a) stress-strain curves for micro-samples having different diameters, as well as the stress-strain curve for a bulk single crystal, (b) a scanning electron micrograph (SEM) image of a micro-sample tested to 4 strains, and (c) a SEM image of a micro-sample after testing (Uchic et al., 2004).

specimen. Moreover, Senger et al. (2008) and Akarapu et al. (2010) investigated the deformation of micro-pillars including dislocation dynamics under compression with constrained loading axis using a discrete dislocation approach. Their technique can provide a rigorous explanation of non-uniform deformations of small scale specimens.

#### 4.2.2 Experimental Micro-pillar Compression Tests performed in Project A6

Micro-pillar compression samples were prepared by using a FIB micro-compression testing method in the Project A6. The mechanical tests are performed by a stiff flat punch indenter under the force rate of  $\dot{F} = 10^{-4} \text{ mNs}^{-1}$ . Two micro-pillar samples

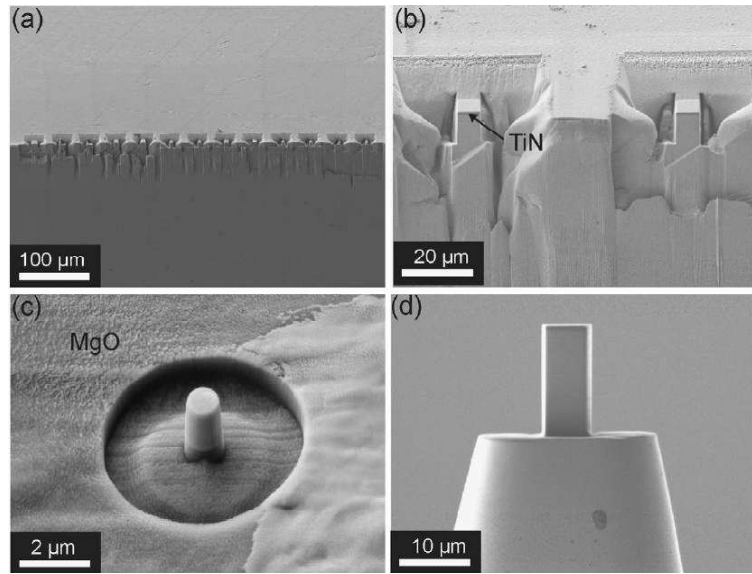


Figure 4.8: (a) Some differently sized Cu samples fabricated into a bulk single crystal, (b) two Cu samples with a thick TiN coating on top, (c) a cylindrical Cu pillar fabricated, and (d) a Cu specimen on top of an etched needle (Kiener et al., 2009).

with different geometry are shown in Figs. 4.9-4.10. Each micro-pillar column has an individual crystal orientation which is given in Table 4.4. In the micro-pillar compression test, the experimental load and displacement data are obtained over time.

Column	$\phi_1 [^\circ]$	$\Phi [^\circ]$	$\phi_2 [^\circ]$
1	80.05	34.79	41.12
2	79.29	34.48	42.29

Table 4.4: Micro-pillar orientations (experiment by Project A6).

### 4.2.3 FE Modeling and Simulation of Micro-pillar Tests

This section describes crystal plasticity FE simulations of the micro-pillar experiments. The aim is to estimate the material parameters of the crystal plasticity model. The single crystal plasticity model described above is applied for the micro-pillar compression simulations. In these micro-pillar simulations, the pillars were modeled as column with perfectly rectangular cross-section placed on a bulk material (Fig. 4.11). The bulk material has the same crystal orientation and same material properties as the micro-pillar itself. Due to the non-constant height in each experimental micro-pillar column, the initial height in the FE micro-pillar model is the mean height of two

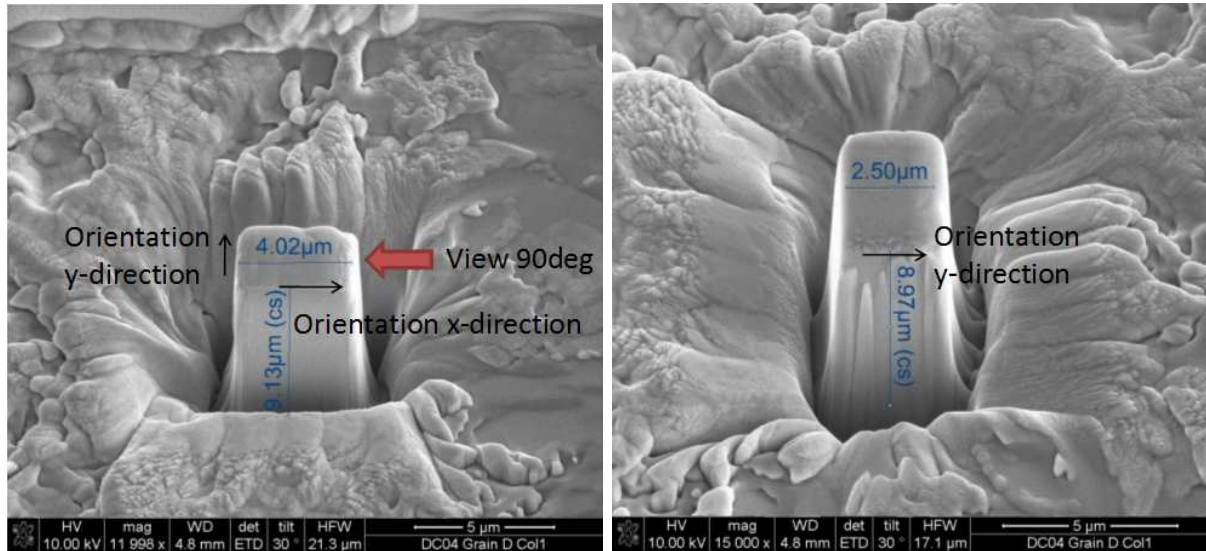


Figure 4.9: Geometry of micro-pillar column 1 (experiment by Project A6).

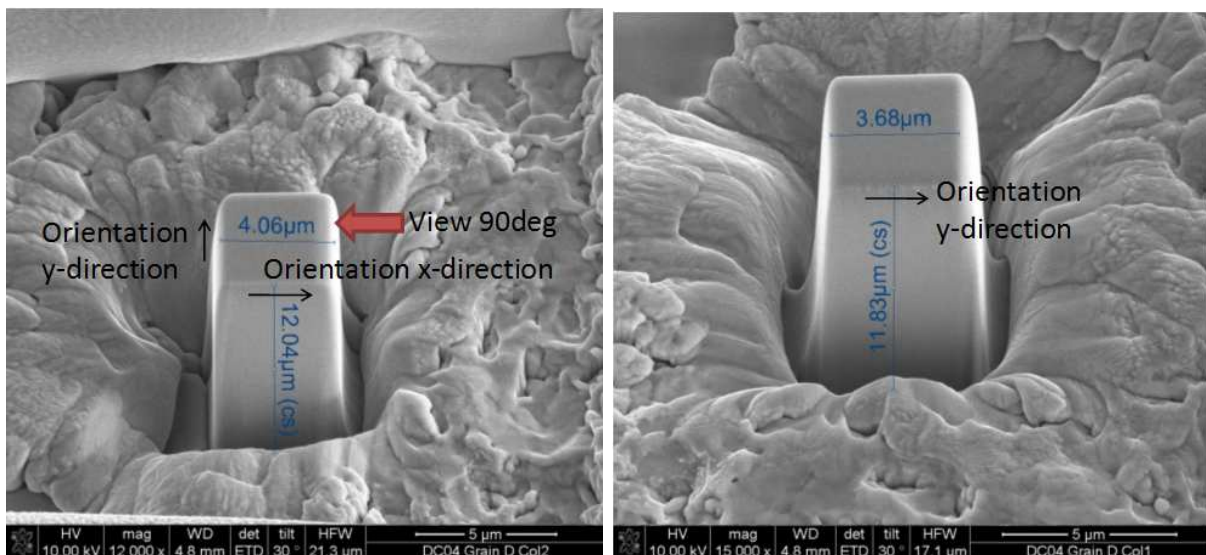


Figure 4.10: Geometry of micro-pillar column 2 (experiment by Project A6).

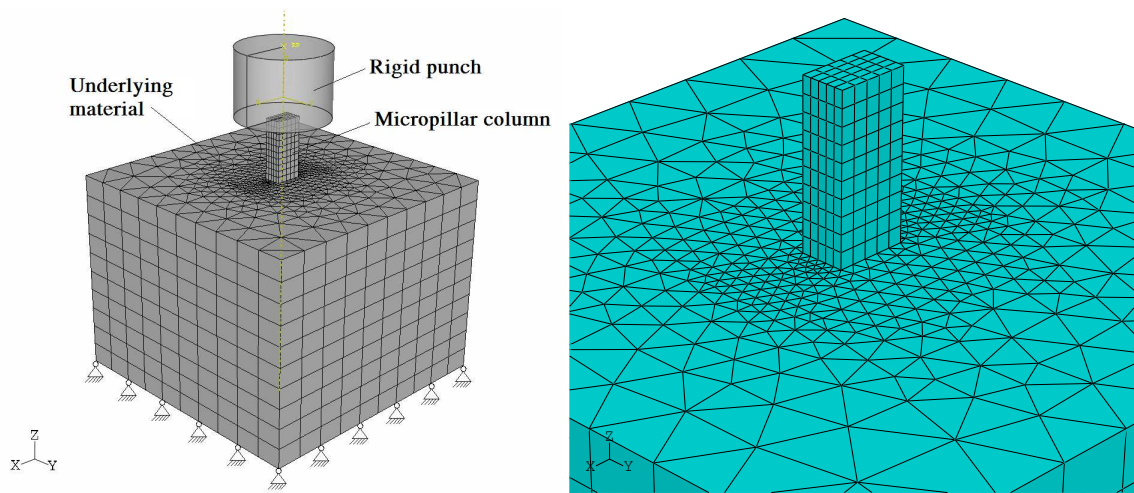


Figure 4.11: Mechanical boundary conditions of micro-pillar test and FE mesh of micropillar and underlying material.

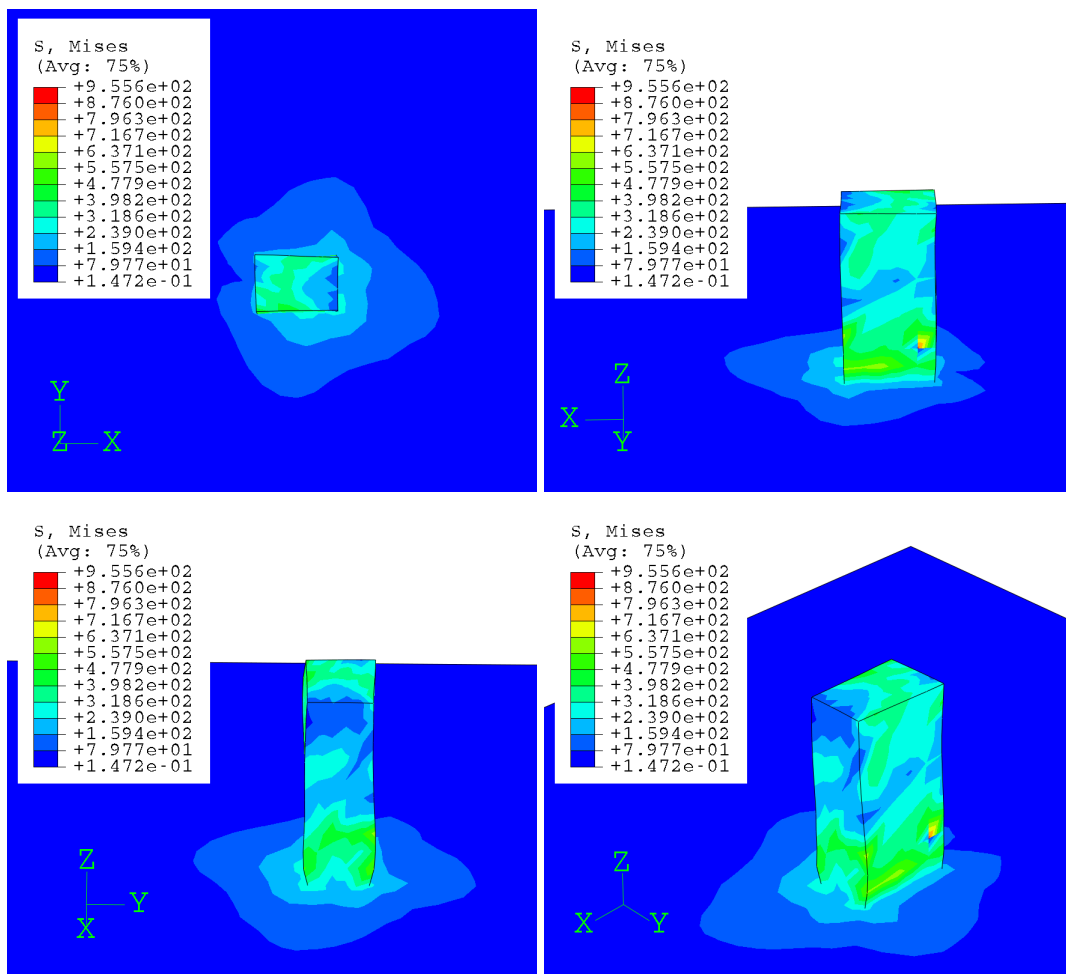


Figure 4.12: The von-Mises stress field [MPa] in deformed configuration of micro-pillar column 1 under different viewpoints.

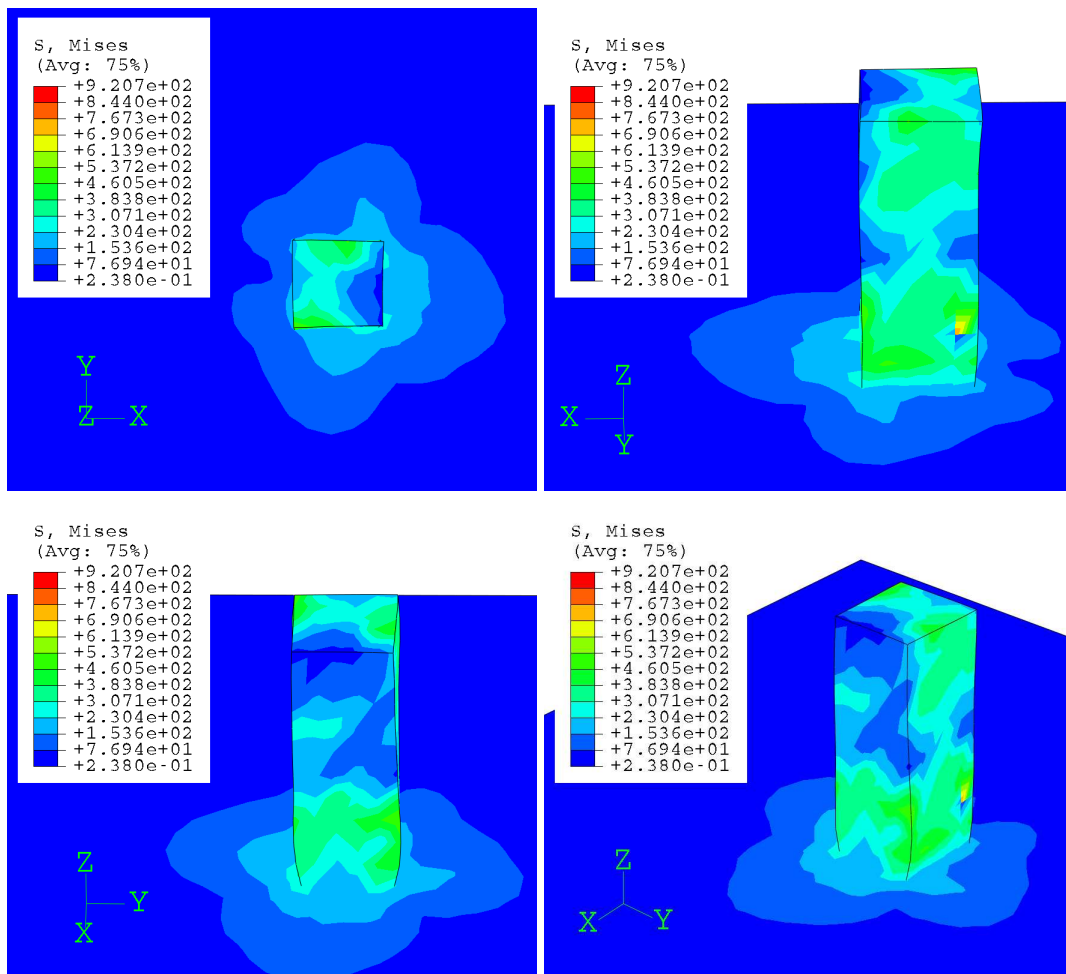


Figure 4.13: The von-Mises stress field [MPa] in deformed configuration of micro-pillar column 2 under different viewpoints.

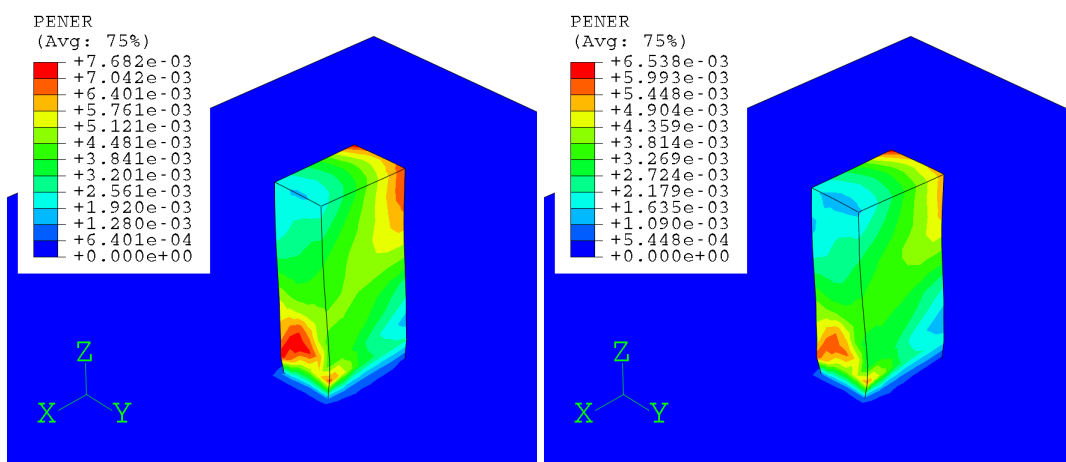


Figure 4.14: Plastic strain rate (PENER [ $s^{-1}$ ]) of column 1 at two different steps: the end of compression step (left) and the end of creep step (right).

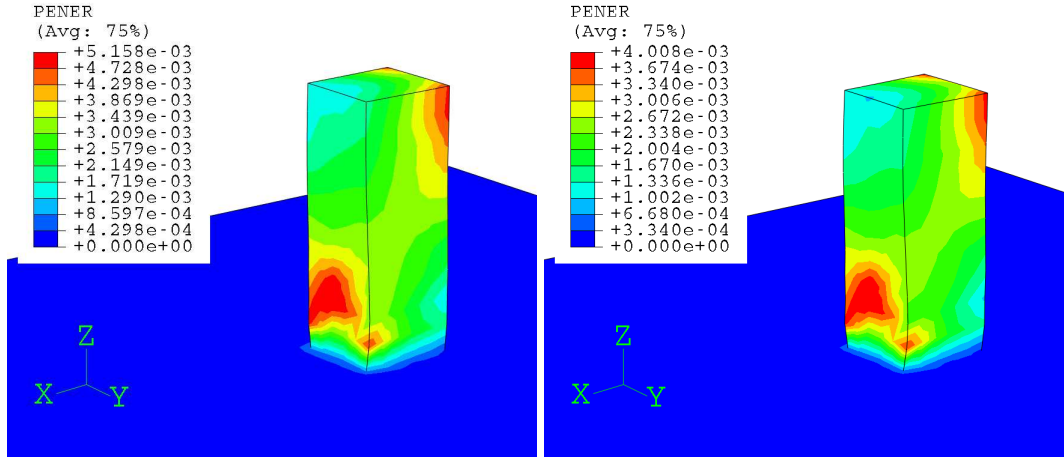


Figure 4.15: Plastic strain rate (PENER [ $s^{-1}$ ]) of column 2 at two different steps: the end of compression step (left) and the end of creep step (right).

observed heights in the experiment. The mean height of column 1 and column 2 is  $9.05 \pm 0.08 \mu m$  and  $11.935 \pm 0.105 \mu m$ , respectively. The loading is subjected to the pillar by means of a rigid punch with a force rate  $\dot{F} = 10^{-4} mNs^{-1}$ . The Coulomb coefficient is set equal to 0.01 for the contact between punch and micro-pillar surface. The displacement at the bottom plane of the base material is assumed to be zero. All other surfaces are stress free. The FE mesh consists of 9301 elements and 5723 nodes (Column 1) and 9001 elements and 5558 nodes (Column 2). Two three-dimensional element types C3D6 and C3D8 are used in FE meshes. During the numerical simulation, the BCC slip systems  $\{110\} + \{112\}\langle 111 \rangle$  are taken into account. The elastic constants of the ferritic steel DC04 used in the FE simulations are given in Table 4.1. The material parameters used in the flow rule are also given in Table 4.1.

Both FE-simulations for the two micro-pillar compression tests are performed in three main steps. In the first step, the micro-pillar is compressed by a punch force under the punch velocity of  $\dot{F} = 10^{-4} mNs^{-1}$  (called the compression step). The total time in this step is 74 s for column 1 and 98 s for column 2, respectively. In the second step, the punch force is kept constant over a period of time depending on each micro-pillar compression test (creep step). This time period is 13 s for column 1 and 15 s for column 2, respectively. In the third step, the compressive force is removed from the surface of the column (unloading step). The total time is 80 s for column 1 and 95 s for column 2, respectively. The simulated results of the stress distribution and the micro-pillar geometry after the unloading step are shown in Fig. 4.12 and 4.13. The plastic strain rate at the different aforementioned main steps for two columns is shown in Fig. 4.14 and 4.15.

#### 4.2.4 Estimation of Material Parameters

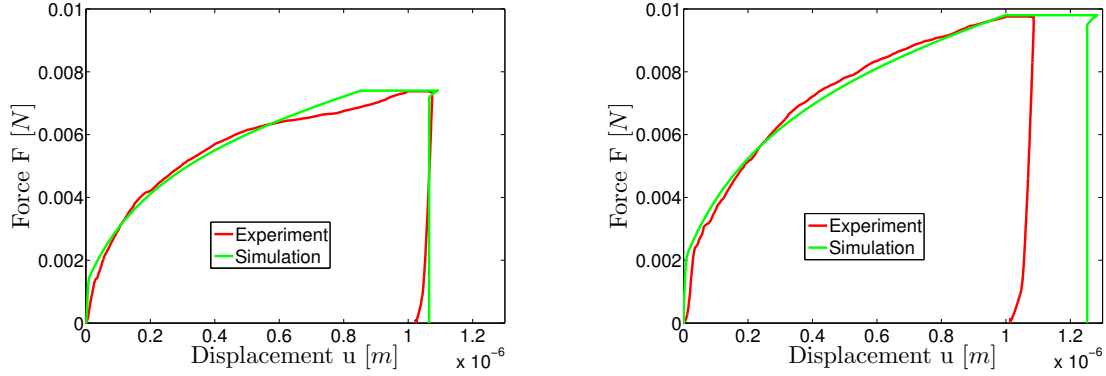


Figure 4.16: Comparison of the numerical and experimental load-displacement curves for micro-pillar column 1 (left) and micro-pillar column 2 (right).

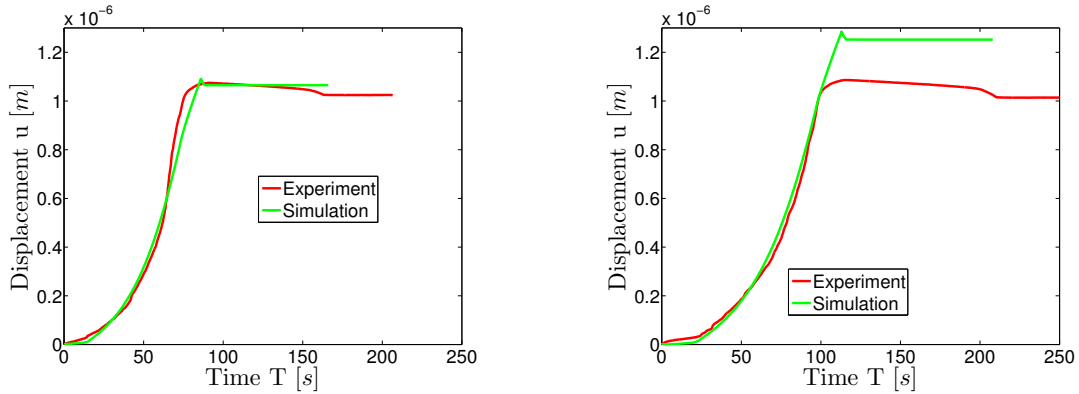


Figure 4.17: Comparison of the numerical and experimental displacement-time curves for micro-pillar column 1 (left) and micro-pillar column 2 (right).

The flow material parameters consisting of the initial critical resolved shear stress  $\tau_0^C$ , the asymptotic critical resolved shear stress  $\tau_{V0}^C$ , and the hardening modulus  $\Theta_0$  are estimated based on the FE micro-pillar simulations. The estimation is performed again by using a least square optimization procedure based on the experimental load-displacement (Fig. 4.16), the displacement-time (Fig. 4.17), and the load-time (Fig. 4.18) curves. The displacement  $u$  is extracted from the displacement of the sample surface which has contact with the punch surface during the micro-pillar simulation. In the creep step, the displacement of column 1 is in good agreement with the experiment, as shown in Fig. 4.16 (left). However, the displacement of column 2 is larger than the observed experiment, as shown in Fig. 4.16 (right). In Fig. 4.19, the computed stress-stretch curves of column 1 and column 2 are compared to the experimental

## Estimation of Material Parameters

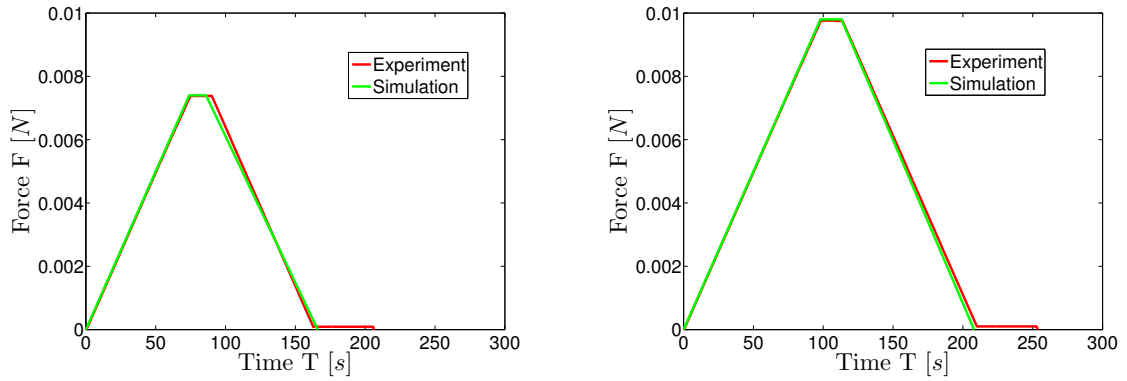


Figure 4.18: Comparison of the numerical and experimental load-time curves for micro-pillar column 1 (left) and micro-pillar column 2 (right).

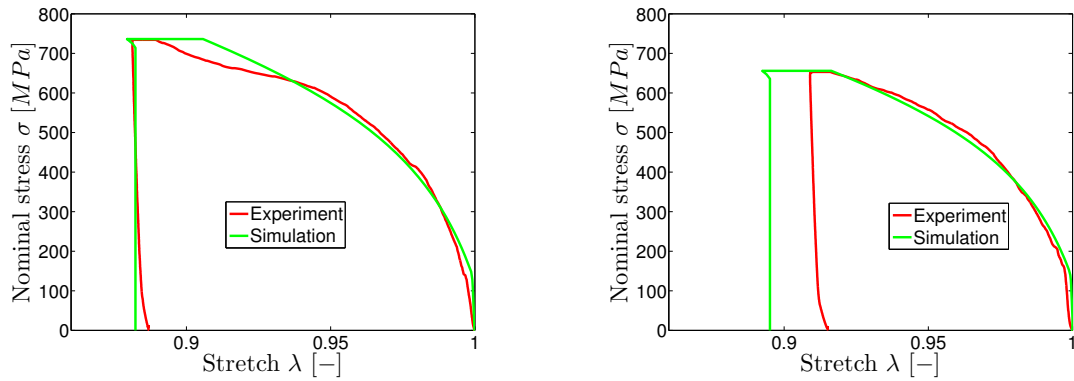


Figure 4.19: Comparison of the numerical and experimental stress-stretch curves for micro-pillar column 1 (left) and micro-pillar column 2 (right).

$\tau_0^C$ [MPa]	$\tau_{V0}^C$ [MPa]	$\Theta_0$ [MPa]
20	160	6000

Table 4.5: Estimated material parameters based on the experimental micro-pillar compression tests of Project A6.

curves. The stretch is defined by  $\lambda = H/H_0 = (H_0 - u)/H_0$ , where  $H_0$  is the initial height of the micro-pillar column, and  $H$  is the height of the micro-pillar column after deformation. It can be seen that the experimental curves are reproduced by the simulations. The set of material parameters is given in Table 4.5.

# Chapter 5

## Simulation of the Deformation Behavior on the Grain Scale

### 5.1 FE-Modeling and Full Field Simulation for EBSD Data

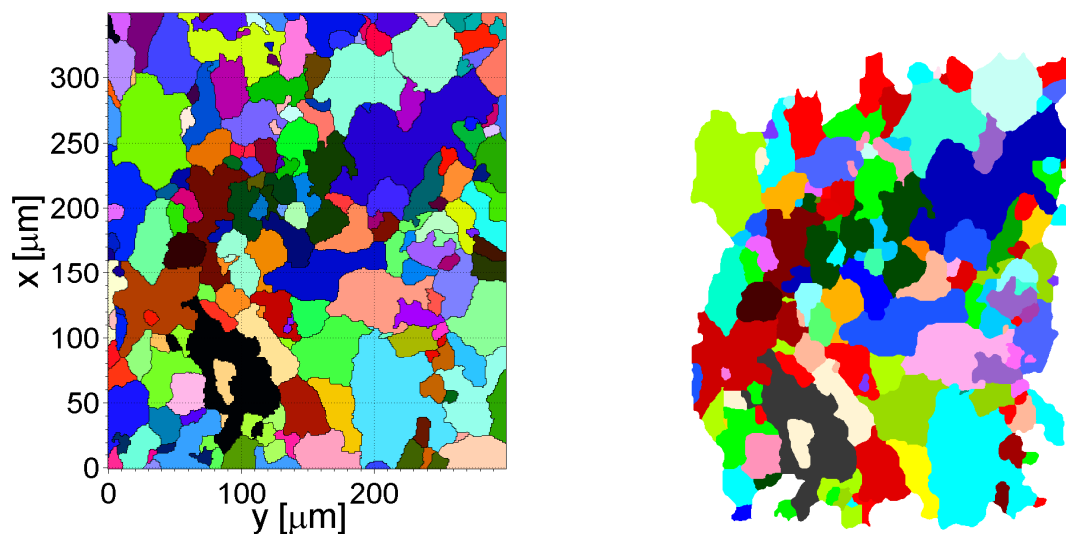


Figure 5.1: (left) Microstructure of heat treated DC04 steel at the initial state obtained from the clustering process by MTEX toolbox and (right) complete grains constructed by the Simpleware software.

In this section, the microstructural image of the tensile specimen at the initial state, as shown in Figure 5.1 (left) (Section 3.2.2, Chapter 3), is used as input data for performing crystal plasticity simulations on the grain scale. The sample picture is imported into a commercial software Simpleware to construct a 2D FE-model as shown in Figure 5.1

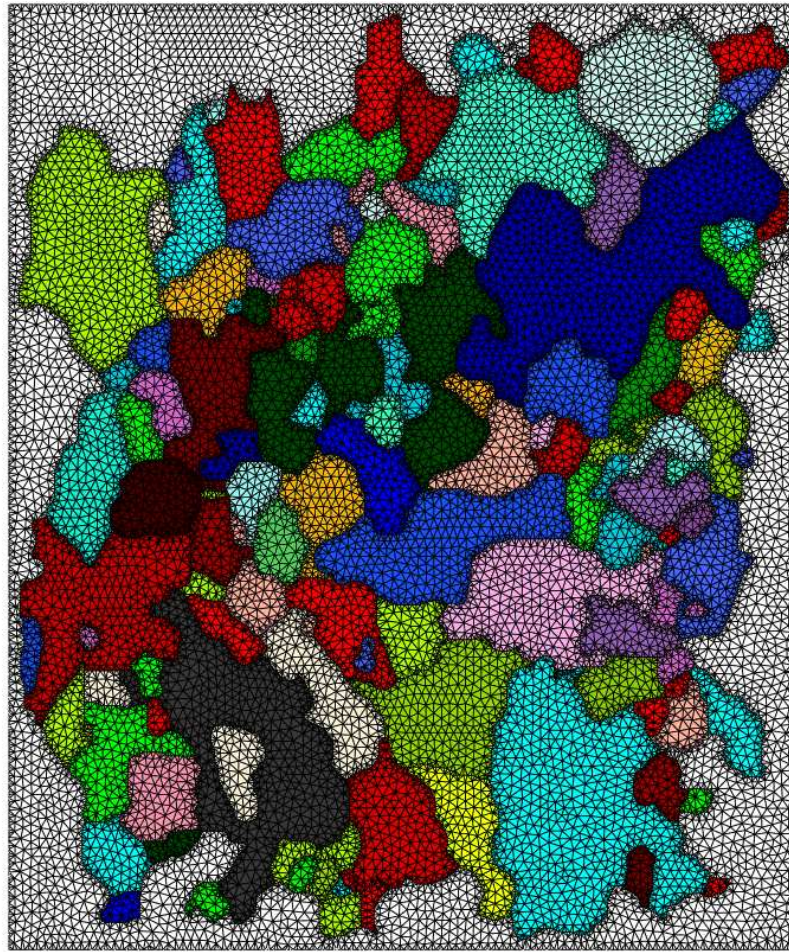


Figure 5.2: FE-mesh of the microstructure at the initial state.

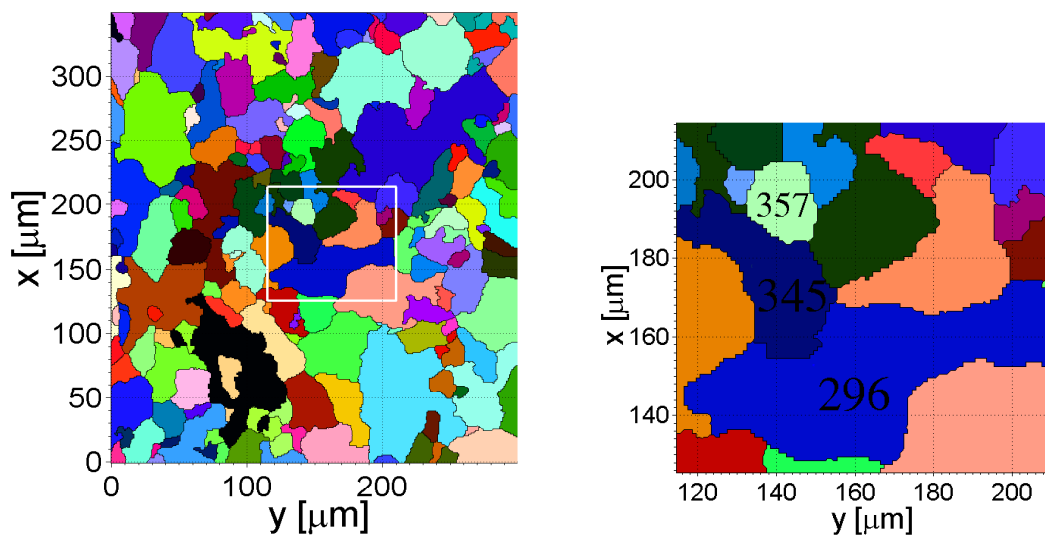


Figure 5.3: (left) Location of 3 selected local grains in the microstructural image and (right) enlargement of 3 local grains: #296, #345 and #357.

(right). Simpleware offers two important options for processing and meshing two- or three-dimensional image data. The first one is ScanIP, which is the platform for the image processing and the second one, is ScanFE which is a fully integrated meshing module for the conversion of masks (or grains) to 2D or 3D finite element meshes. The type of elements used in the FE mesh are linear and quadratic hexahedral elements. Details of the software can be found in Simpleware (2000–2011). After the processing steps in ScanIP, a FE output data containing the set of nodes, the set of hexahedral elements, and the set of tetrahedral elements is obtained. The data can be exported in the ABAQUS format (Fig. 5.2). Different colors indicate different crystal orientations of the grains. The white region around the grains was assumed to show an ideal behavior according to the von Mises plasticity model. The plastic properties with Young’s modulus ( $E = 200$  GPa) and Poisson’s ratio ( $\nu = 0.3$ ) are assigned to the ideal von Mises plastic region. For the plastic behavior, the flow parameters  $\sigma_{F0} = 180$  MPa,  $\sigma_{F\infty} = 303$  MPa, describing the linear hardening, are estimated from the experimental tensile stress-strain curve for  $0^\circ$  to the rolling direction (Fig. 4.1).

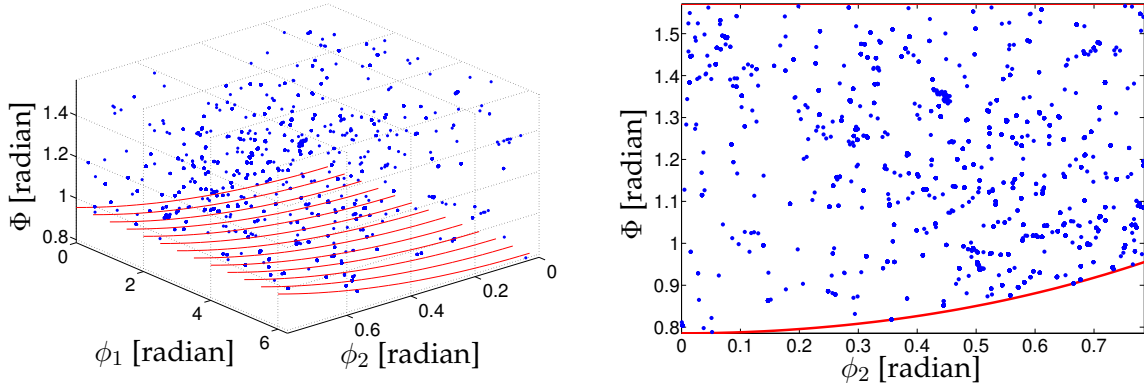


Figure 5.4: Initial grain orientations in the 3D (left) and 2D fundamental zone  $\phi_2 - \Phi$  (right).

Note that the color distribution of grains in Fig. 5.1 (right) is not equal to the one in Fig. 5.1 (left) due to the different conventions of colours between the Simpleware software and ABAQUS/CAE. In order to uniquely define the evolution of 45 grains during the FE simulation, initial Euler angles of these grains are transformed into the cubic fundamental zone as aforementioned in Section 3.3. The fundamental zone is described in Fig. 5.4. In Fig. 5.5, the initial Euler angles of 45 grains transformed in the fundamental zone are shown. Fig. 5.3 shows the location of 3 local grains in the experimental microstructure. The initial Euler angles of these grains are explicitly shown in the FE simulation (Fig. 5.6). The simulation is carried out by using the implicit Euler scheme for time integration and the user subroutine UMAT

## Simulation of the Deformation Behavior on the Grain Scale

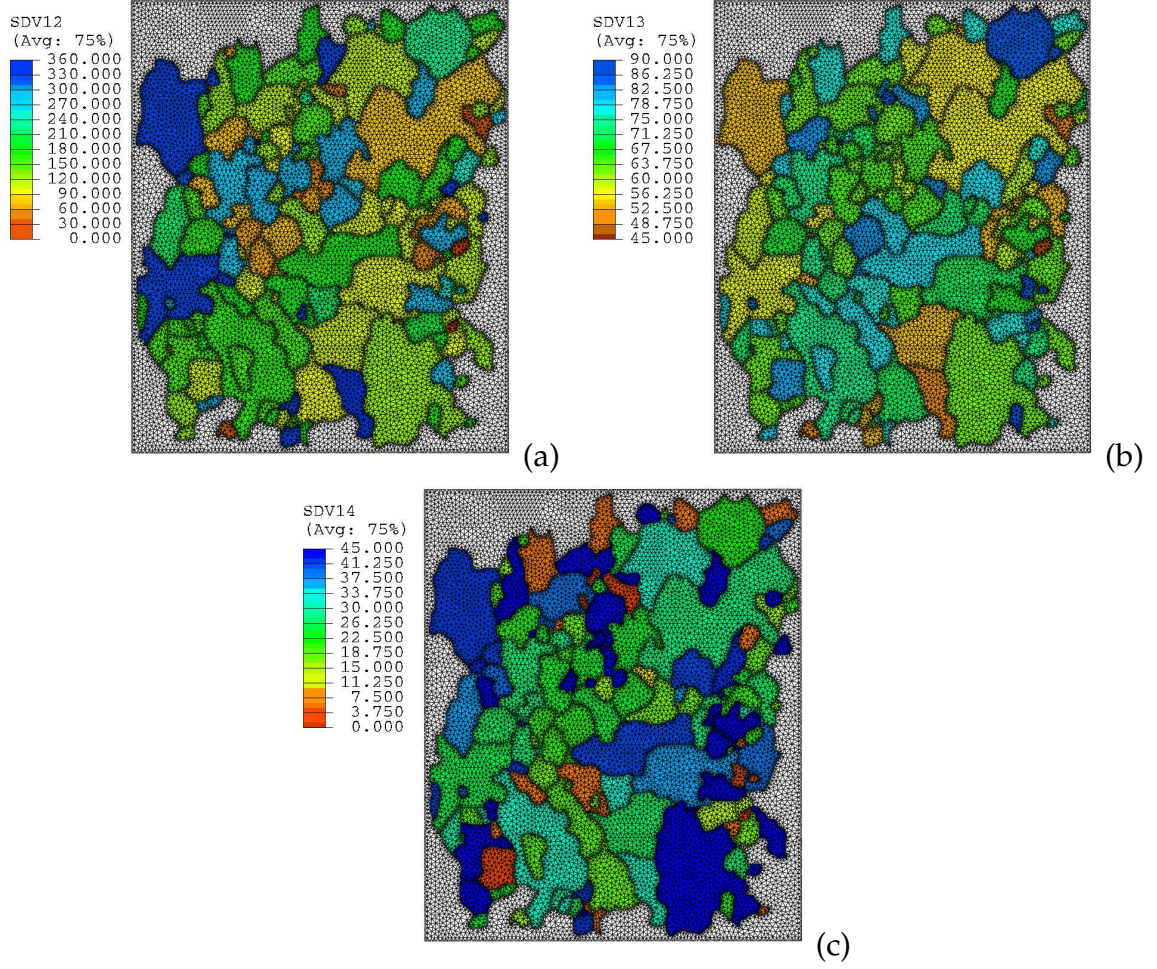


Figure 5.5: Initial Euler angle distribution [ $^{\circ}$ ] in the FE simulation: (a) angle  $\phi_1$ , (b) angle  $\Phi$  and (c) angle  $\phi_2$  in the fundamental zone.

defining the constitutive law of the crystals introduced in Chapter 2. The material parameters shown in Table 4.3, are used for performing the grain scale simulation. For the slip mechanism, the grain scale simulation is based on using the combination of  $\{110\}\langle 111\rangle + \{112\}\langle 111\rangle$  slip systems. Homogeneous displacement boundary conditions at the outer boundary of the RD-TD plane are applied. The strain in the normal direction (ND) is assumed to be zero. Furthermore, a plane strain state is assumed. The boundary conditions are defined by the ABAQUS subroutine DISP. The displacement vector and the displacement gradient are given by

$$\mathbf{u}(\mathbf{X}, t) = \mathbf{x} - \mathbf{X} \quad (5.1)$$

and

$$\mathbf{H} = \text{Grad}(\mathbf{u}(\mathbf{X}, t)), \quad (5.2)$$

respectively, where  $\mathbf{X}$  is the reference position of the material points and  $\mathbf{x} = \chi_{\kappa}(\mathbf{X}, t)$  is the current position at time  $t$ . The displacement gradient  $\mathbf{H}$  can be given in terms of

## Simulation of the Deformation Behavior on the Grain Scale

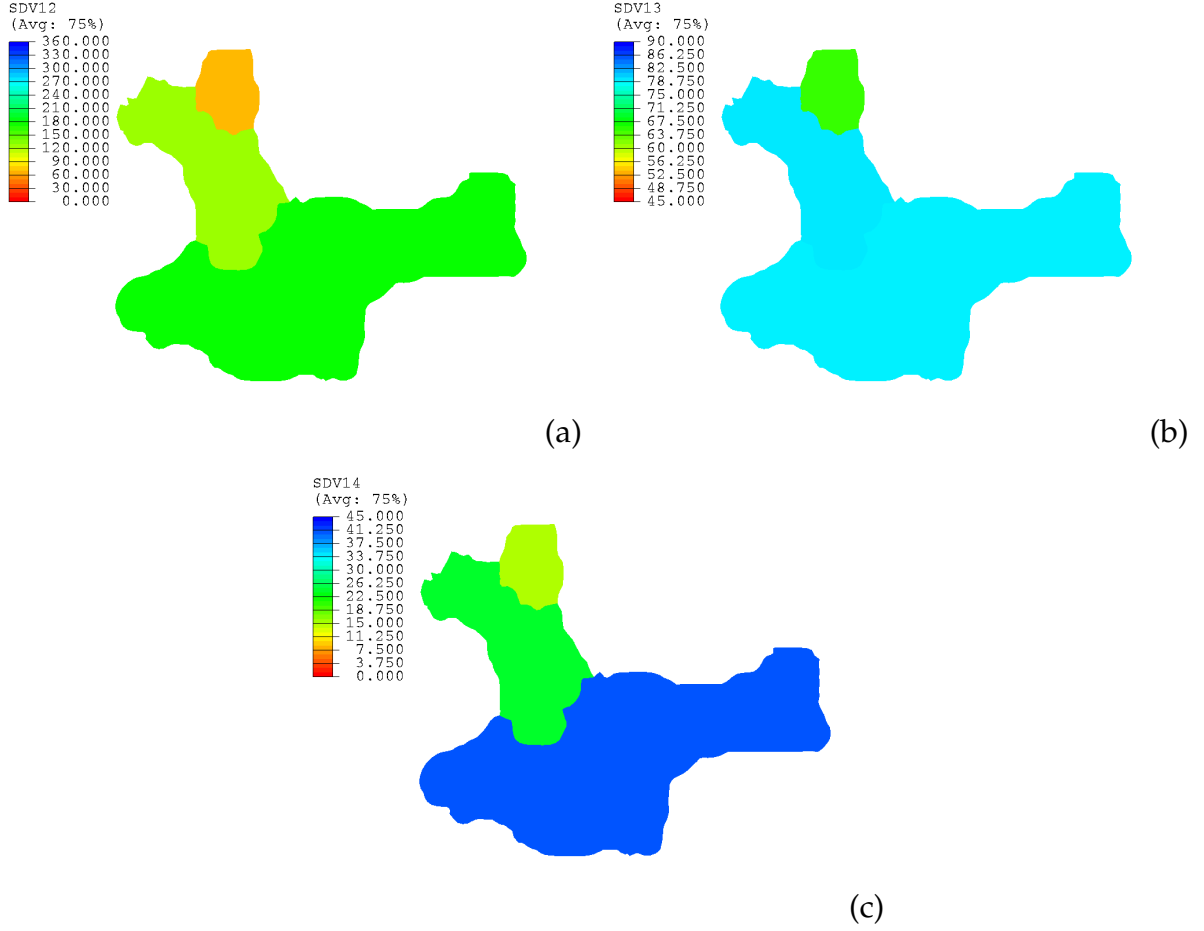


Figure 5.6: Initial Euler angles [°] of 3 local grains in the FE simulation: (a) angle  $\phi_1$ , (b) angle  $\Phi$  and (c) angle  $\phi_2$  in the fundamental zone.

the deformation gradient  $\mathbf{F}$

$$\mathbf{H} = \text{Grad}(\mathbf{u}(\mathbf{X}, t)) = \text{Grad}(\mathbf{x}) - \mathbf{I} = \mathbf{F} - \mathbf{I} \quad (5.3)$$

Assuming the constant velocity gradient for plane strain compression is given by

$$\mathbf{L} = \dot{\epsilon}_0 \begin{bmatrix} \frac{-1}{\sqrt{2}} & 0 & 0 \\ 0 & \frac{1}{\sqrt{2}} & 0 \\ 0 & 0 & 0 \end{bmatrix} \mathbf{e}_i \otimes \mathbf{e}_j. \quad (5.4)$$

The deformation gradient is given by the exponential form,

$$\mathbf{F}(t) = \exp(\mathbf{L}t)\mathbf{F}(0), \quad (5.5)$$

with  $\mathbf{F}(0) = \mathbf{I}$ . The constant strain rate is set to  $\dot{\epsilon}_0 = 10^{-3} [\text{s}^{-1}]$ . The special form of the velocity gradient implies a displacement in the X-Y plane in the reference configuration

## Simulation of the Deformation Behavior on the Grain Scale

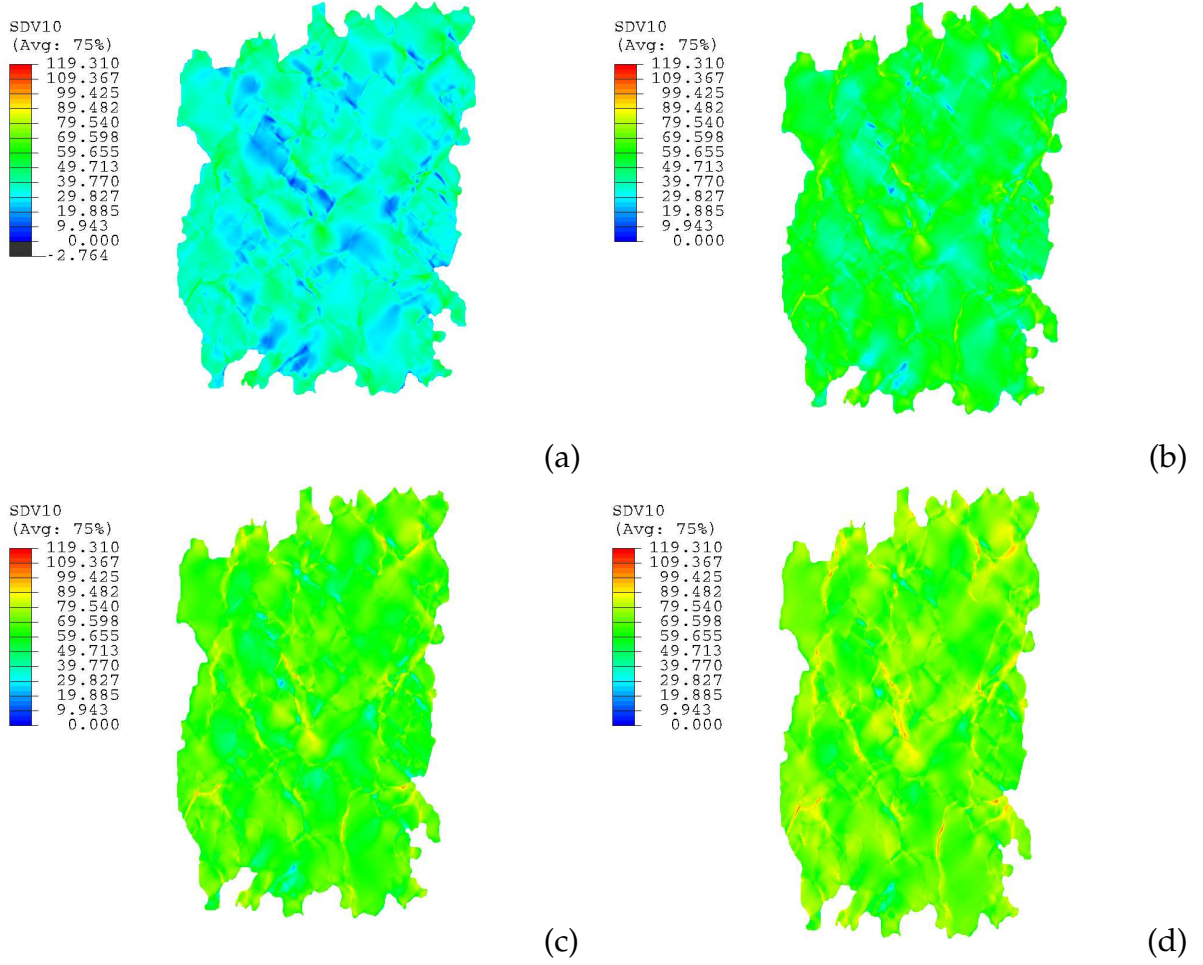


Figure 5.7: Distribution of critical resolved shear stress [MPa] of the grain structure at the different states: (a) 5%, (b) 10%, (c) 15% and (d) 20% elongation.

and a constant volume during the simulation. From Eq. 5.2, the displacement on the boundary is obtained

$$\mathbf{u}(\mathbf{X}, t) = \mathbf{H}\mathbf{X} = \mathbf{H}\mathbf{F}^{-1}\mathbf{x}. \quad (5.6)$$

By combining this equation with Eq. 5.3, the prescribed displacement is defined in the subroutine DISP at the time  $t$  in terms of the deformation gradient in Eq. 5.5, so that the displacement becomes

$$\mathbf{u}(\mathbf{X}, t) = (\mathbf{I} - \mathbf{F}^{-1})\mathbf{x}. \quad (5.7)$$

The total time in FE-simulation is 260 s corresponding to 20% elongation. The FE results are evaluated at different total times such as 65 s, 130 s and 195 s corresponding to 5%, 10% and 15% elongation, respectively. The field of critical resolved shear stress  $\tau_c$  is depicted in Fig. 5.7 at the aforementioned different states of the FE simulation. These results show a strongly inhomogeneous field caused by the evolution of individual grain orientations in the microstructure during deformation.

## Simulation of the Deformation Behavior on the Grain Scale

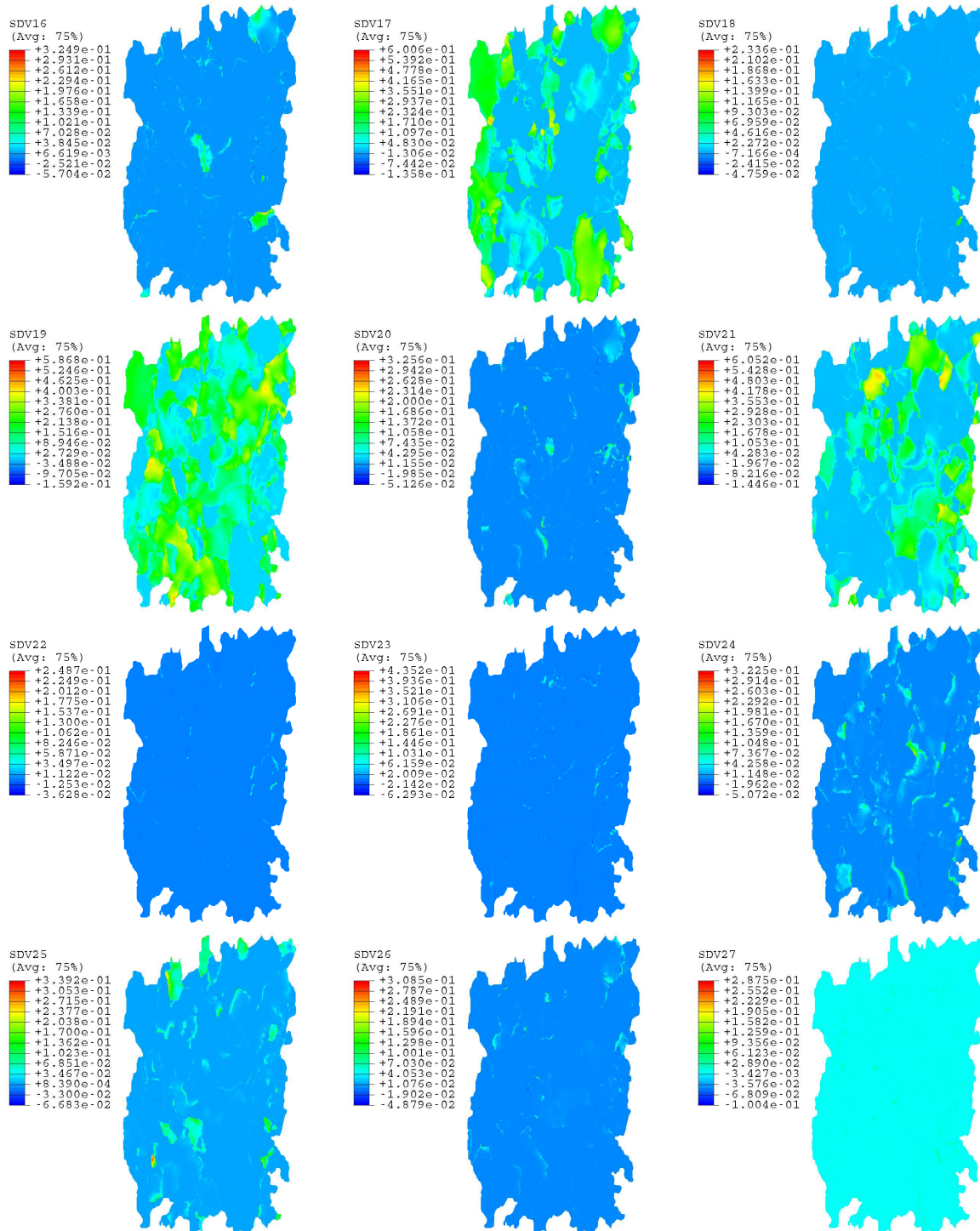


Figure 5.8: Plastic slip on 12 slip systems  $\{110\}\langle 111 \rangle$  at 20% elongation, the unit is  $[s^{-1}]$ .

## Simulation of the Deformation Behavior on the Grain Scale

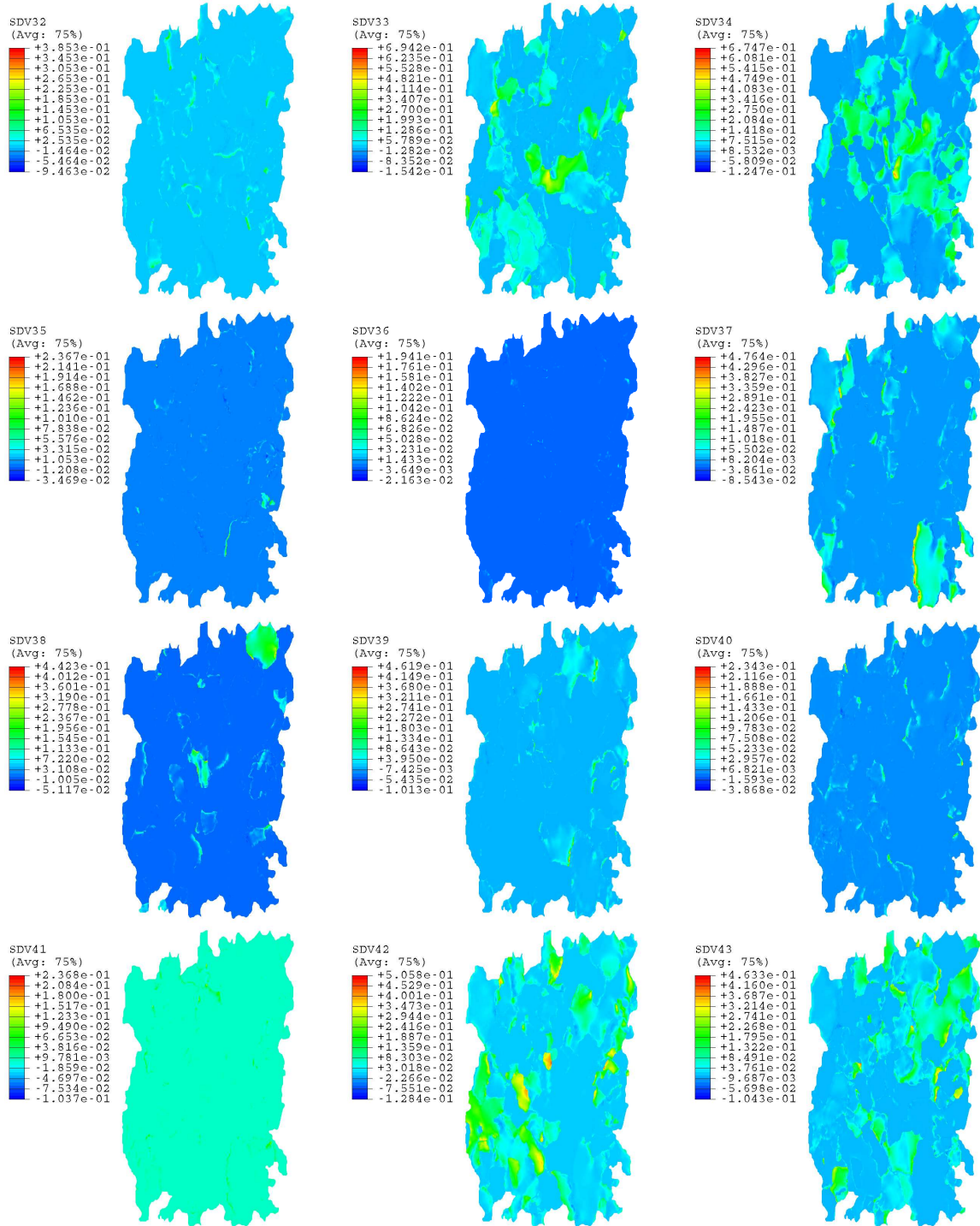


Figure 5.9: Plastic slip of 12 slip systems  $\{112\}\langle 111 \rangle$  at 20% elongation, the unit is  $[s^{-1}]$ .

In addition, the plastic slip of each slip system  $\alpha$  ( $\alpha = 1 \dots 24$ ) in BCC slip systems  $\{110\} + \{112\}\langle 111 \rangle$  is computed by integrating the slip rate  $\dot{\gamma}_\alpha$  over the time during the grain scale simulation. The plastic slip is described as follows

$$\gamma_\alpha = \int_0^t |\dot{\gamma}_\alpha| dt. \quad (5.8)$$

Figs. 5.8-5.9 represent the plastic slip in 24 slip systems at 20% elongation. It can be seen that the grain-structure shows a very heterogeneous state of slip.

## 5.2 Comparison between Grain Scale Simulations and Experiments

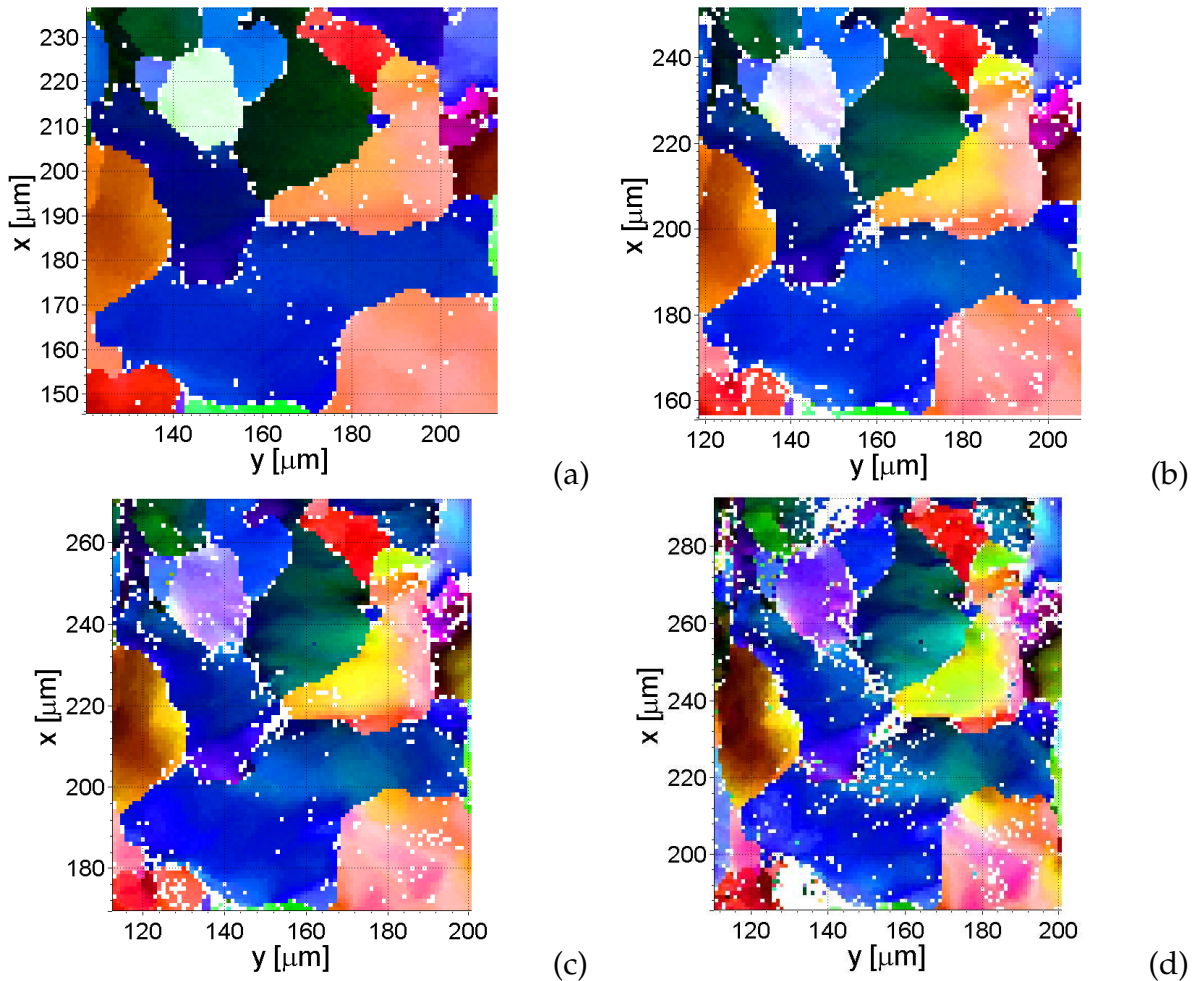


Figure 5.10: Microstructural images of local grains at different states.

In this section, a comparison between the numerical results and the experimental data is performed for three local grains. Numerical results at different tensile strains are

## Simulation of the Deformation Behavior on the Grain Scale

compared to the corresponding experimental results. In order to obtain Euler angles and the reorientation in the three grains (Fig. 5.10), post processing steps have to be carried out. Firstly, the measured grain data set at each different state of deformation is transformed into the fundamental zone. Secondly, each triple of Euler angles of the measurement points is extracted at different states of deformation. A comparison of Euler angles between the experiment and the FE simulation is shown in Figs. 5.11-5.14. The evolution of Euler angles in the numerical simulation is quite close to the experimental findings.

In the third step, the reorientation of each measurement point is computed for each state of deformation. The formula to compute the angle of reorientation is given by

$$\omega = \left| \arccos \left( \frac{\text{tr}(\mathbf{Q}\mathbf{Q}_0^T) - 1}{2} \right) \right|, \quad (5.9)$$

where  $\mathbf{Q}_0$  represents the crystal orientation at the initial state of deformation and  $\mathbf{Q}$  the orientation of the same point at different states of deformation. Both  $\mathbf{Q}_0$  and  $\mathbf{Q}$  are parameterized by Euler angles lying in the same fundamental zone. During the simulation,  $\mathbf{Q}$  is extracted by the polar decomposition  $\mathbf{F}_e = \mathbf{R}_e \mathbf{U}_e$ , where  $\mathbf{R}_e = \mathbf{Q}$  is the elastic rotation and  $\mathbf{U}_e$  is the elastic stretch tensor. The computed reorientation is the minimum relative orientation distance between the initial and actual crystal orientation. By comparing the colour distribution representing the values in the legend (Fig. 5.15), the reorientations in the numerical simulations agree well with the experimental results. In addition, the computed reorientations of local grains #345 and #296 are in good agreement with the experiment. However, the computed reorientation of local grain the #357 is lower than in the experiment. This can probably be explained by neglecting the three-dimensional grain structure due to the lack of data.

## Simulation of the Deformation Behavior on the Grain Scale

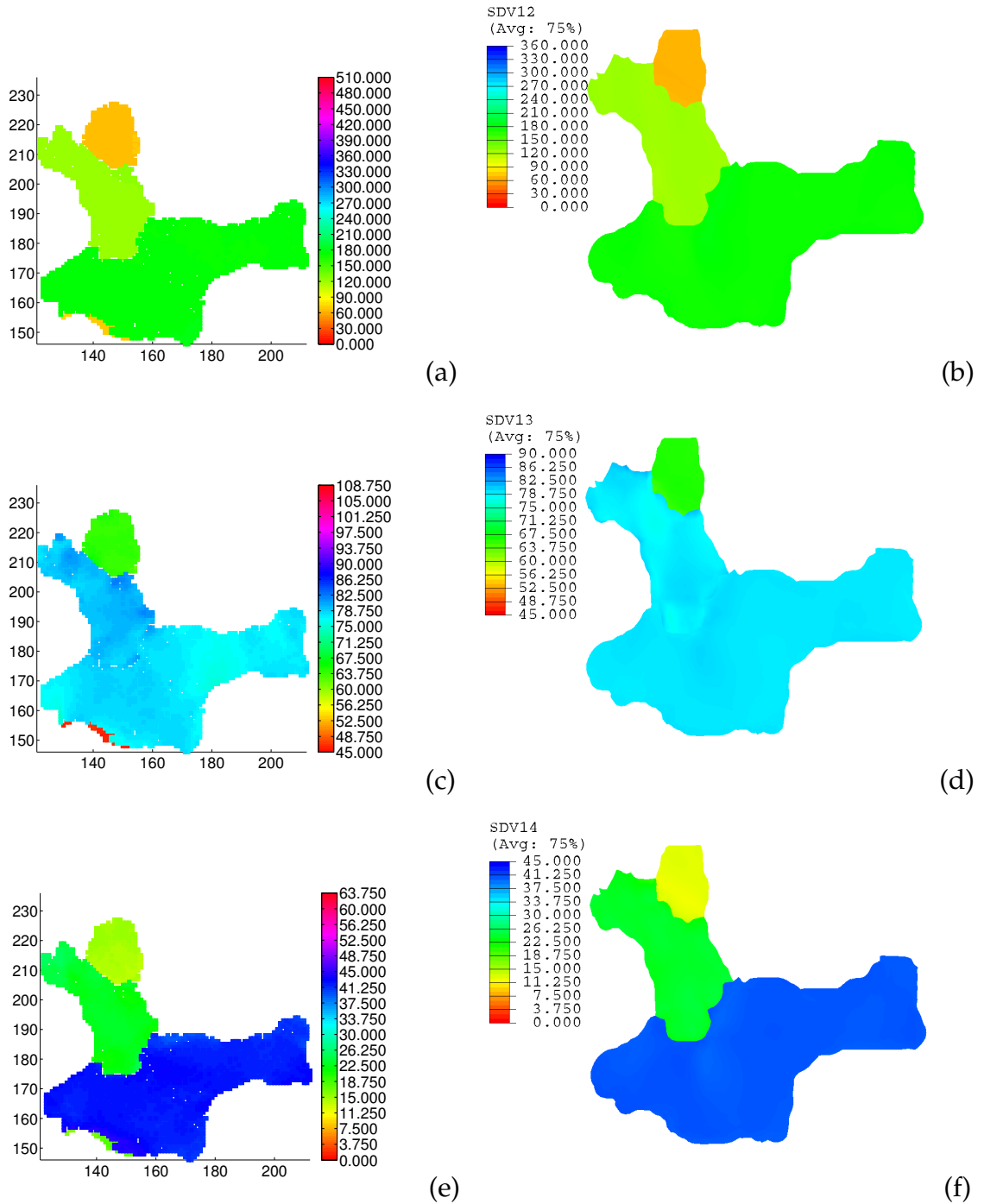


Figure 5.11: Comparison of Euler angles  $[\circ]$  between the experiment (left) and numerical results (right) at the state of 5% elongation: (a)–(b) angle  $\phi_1$ , (c)–(d) angle  $\Phi$ , (e)–(f) angle  $\phi_2$ .

## Simulation of the Deformation Behavior on the Grain Scale

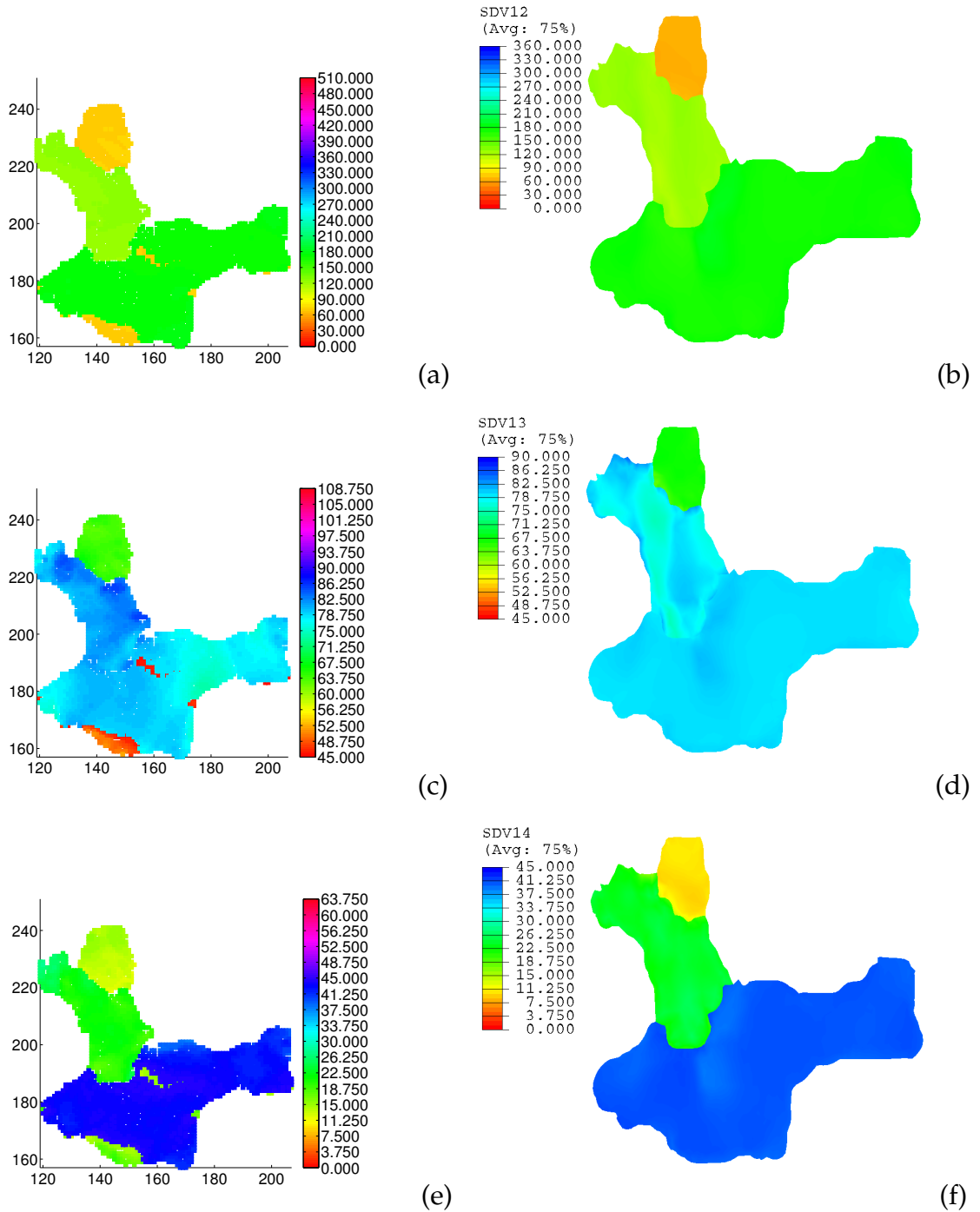


Figure 5.12: Comparison of Euler angles  $[\circ]$  between the experiment (left) and numerical results (right) at the state of 10% elongation: (a)–(b) angle  $\phi_1$ , (c)–(d) angle  $\Phi$ , (e)–(f) angle  $\phi_2$ .

## Simulation of the Deformation Behavior on the Grain Scale

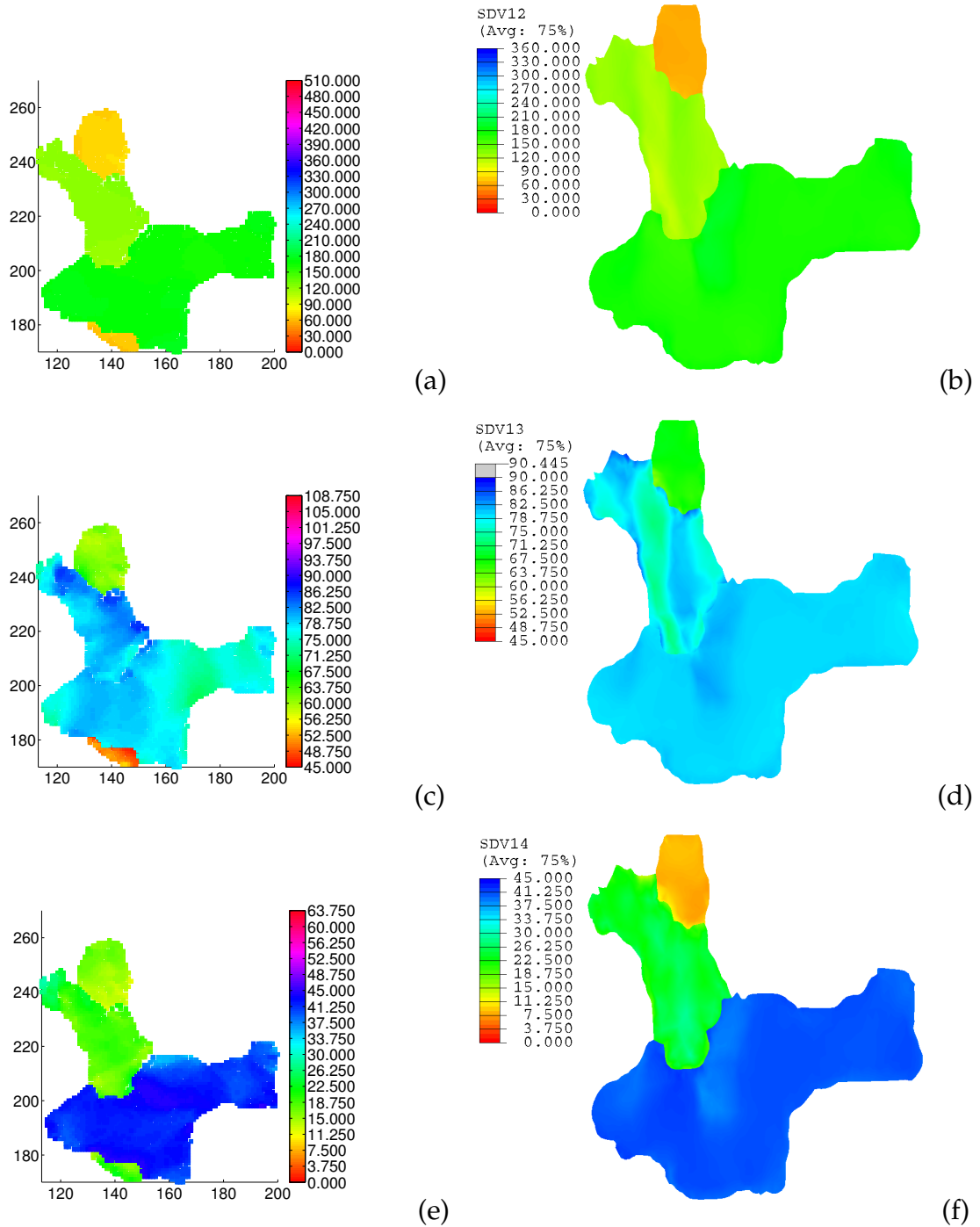


Figure 5.13: Comparison of Euler angles [ $^{\circ}$ ] between the experiment (left) and numerical results (right) at the state of 15% elongation: (a)–(b) angle  $\phi_1$ , (c)–(d) angle  $\Phi$ , (e)–(f) angle  $\phi_2$ .

## Simulation of the Deformation Behavior on the Grain Scale

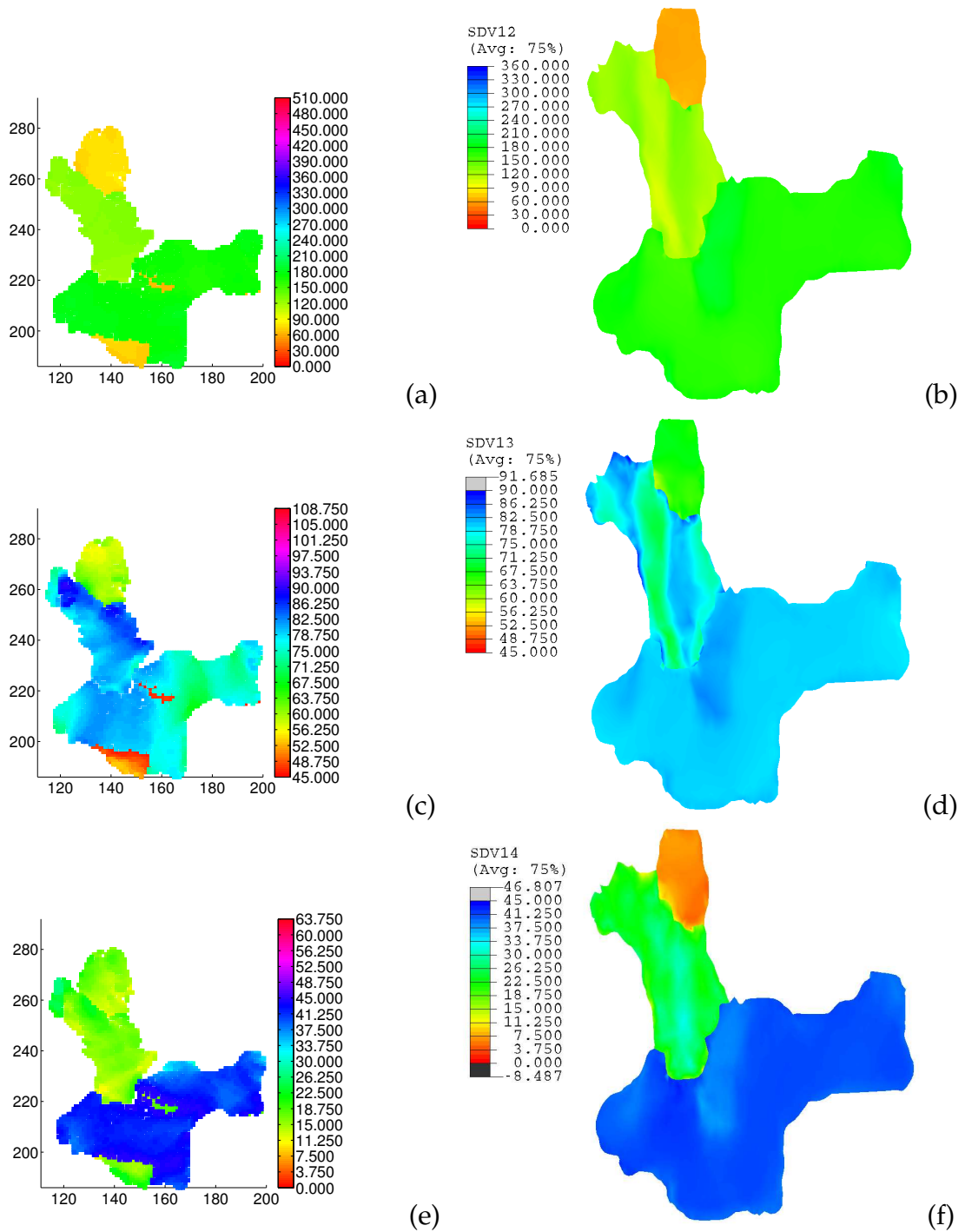


Figure 5.14: Comparison of Euler angles [ $^{\circ}$ ] between the experiment (left) and numerical results (right) at the state of 20% elongation: (a)–(b) angle  $\phi_1$ , (c)–(d) angle  $\Phi$ , (e)–(f) angle  $\phi_2$ .

## Simulation of the Deformation Behavior on the Grain Scale

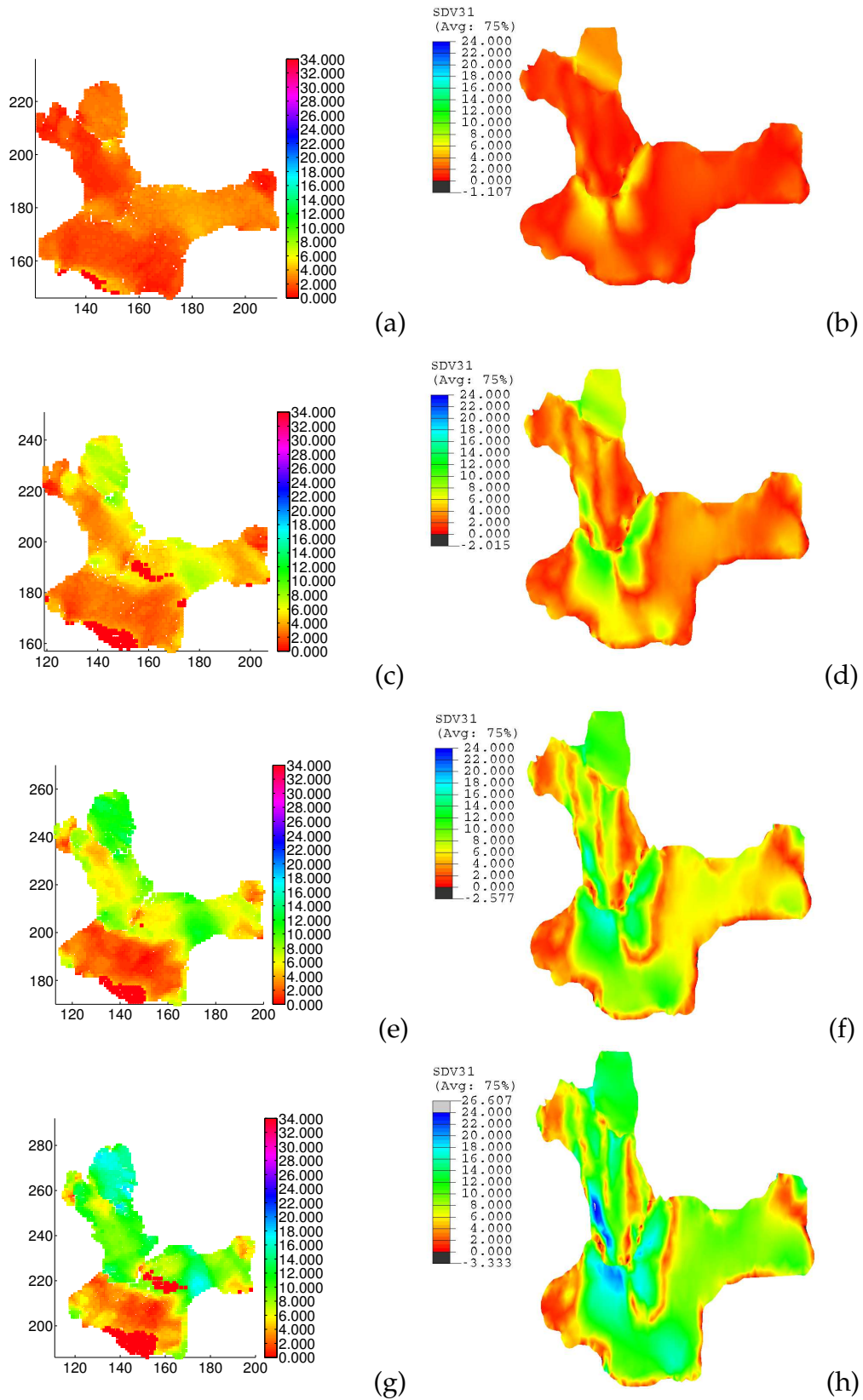


Figure 5.15: Comparison of reorientation  $[\circ]$  between the experiment (left) and numerical results (right) at different states: (a)–(b) 5%, (c)–(d) 10%, (e)–(f) 15%, (g)–(h) 20% elongation.

## Chapter 6

# Application of the Polycrystal Model for Metal Forming Operation

### 6.1 Deep Drawing Experiment at IFU



Figure 6.1: Experimental deep drawing tool set-up and some products (IFU, Stuttgart).

In manufacturing engineering, the experimental rig shown in Fig. 6.1, is one of the widely used equipment to produce cup shaped components. Cup drawing is not only an important metal forming process but also serves as a basic test for the sheet metal formability and for modeling the anisotropic behavior of metal. Due to the recent developments of the powerful computer hardware, much attention has been given to the computer simulation for sheet metal forming. Simultaneously, the three-dimensional sheet metal forming analysis technique has reached an early stage of maturity that allowed for the industrial use based on the development of the three-dimensional simulation software.

There are several basic and extended studies on constitutive laws in FE codes to model

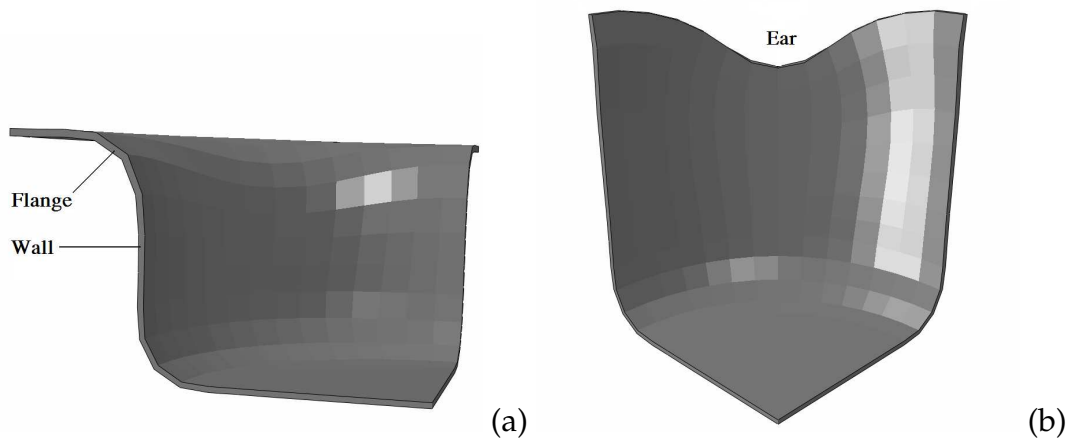


Figure 6.2: (a) Illustration of two important regions in the deep drawing process and (b) the characteristics of earing profile in a quarter of the drawn cup.

rigid-viscoplastic, elasto-viscoplastic and elastoplastic anisotropic behaviour of metals at the macroscopic level, see, e.g. Taylor (1938); Dawson et al. (2004); Kanetake et al. (1985); Mathur and Dawson (1989); Lege et al. (1989); Miehe et al. (1999); Dawson et al. (2004); Habraken (2004); Delannay et al. (2005); Böhlke et al. (2006, 2007); Ahn et al. (2009); Schulze et al. (2009). During the deep drawing process, two important regions of the can shown in Fig. 6.2a are considered to include the flange where most of the deformation occurs and the wall that supports the force being necessary to cause the deformation in the flange. In the case of the blank diameter being too large, the force in the wall can exceed its strength and, therefore, possibly cause a failure (Hosford and Caddell, 2007). The peaks (highest positions) and the valleys of a drawn cup are illustrated in Fig. 6.2b.

In this chapter, the estimated material parameters in Chapter 4 are applied for the two-scale Taylor type model to perform FE simulations of a deep drawing process (Phan et al., 2010, 2011a). The orientation data sets, explained in Chapter 3, are assigned to the FE-model at the integration points. By applying this method, the earing profile of a sheet metal is predicted and compared to the experimental results provided by the Institute of Forming Technology (IFU, University of Stuttgart).

Three experiments are carried out at IFU (Fig. 6.4). The experimental set-up is given as follows: the blank holder force was 98 kN (mass of 10 T); punch diameter: 100 mm; punch profile radius: 10 mm; die opening diameter: 104 mm; die profile radius: 10 mm; sheet diameter: 180 mm, illustrated in Fig. 6.3 (left). The sheet thickness is 1.2 mm. The measured Coulomb coefficient  $\mu$  was found in the range 0.08 – 0.12 taking into account the experimental oil lubrication. The measured earing profiles are depicted in Fig. 6.3 (right).

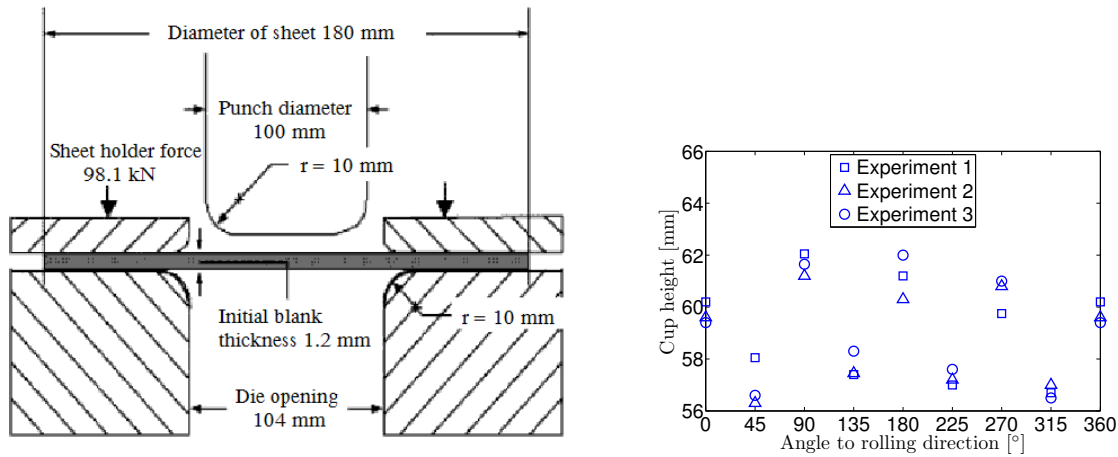


Figure 6.3: (left) Tool geometry and set-up for deep drawing process and (right) earing profiles obtained from deep drawing process in experiments (IFU, University of Stuttgart).

## 6.2 FE-Modeling and Simulation of Deep Drawing

In this section, a FE-model of a deep drawing process using ABAQUS standard (Abaqus/CAE, 2009) is considered. Due to the orthotropic sample symmetry of the orientation data set and the symmetry of the experimental tool set-up, only a quarter of the DC04 steel sheet is modeled in a three-dimensional deep drawing process. Figs. 6.5 show the FE-model of the deep drawing process for a quarter of the sheet metal. The number of elements is 253 in this FE-model. The element types C3D8H and C3D6H are used in two partitioned regions of the DC04 steel sheet, illustrated in Fig. 6.6. At the initial state, the quarter of the sheet is fixed between the upper die and lower die. A ring is inserted between the dies and lies on the lower die. The ring thickness, 1 mm, is smaller than the sheet thickness. The objective of the ring is to avoid contact of the dies causing numerical problems. The punch displacement is approximately set to 70 mm similar to the experimental data.

### 6.2.1 Deep Drawing Simulation for a Single Crystal

The first FE simulation concentrates on a single crystalline sheet with the standard orientation within the material. The form of ears are different for each selected single crystal orientation. Two different single crystal orientations illustrated in Fig. 6.7 are taken into account in this section. The first single crystal orientation,  $[100]$ -orientation,



Figure 6.4: The deformed cups of 3 experiments: (a)-(b) Experiment 1, (c)-(d) Experiment 2, (e)-(f) Experiment 3 (experiment by IFU (University of Stuttgart)).

## Application of the Polycrystal Model for Metal Forming Operation

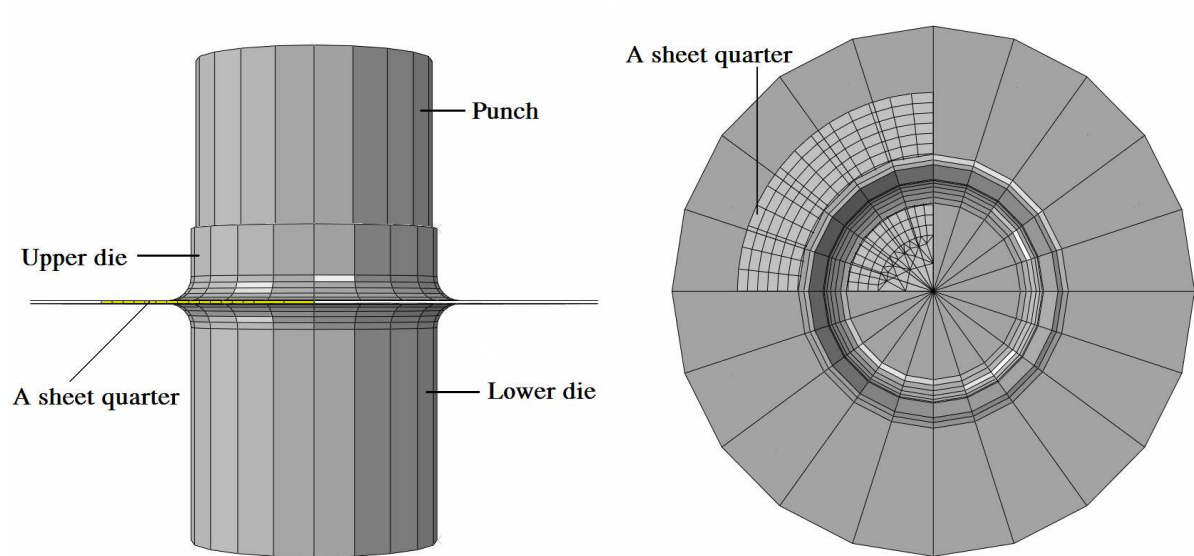


Figure 6.5: FE deep drawing simulation set-up of a sheet quarter.

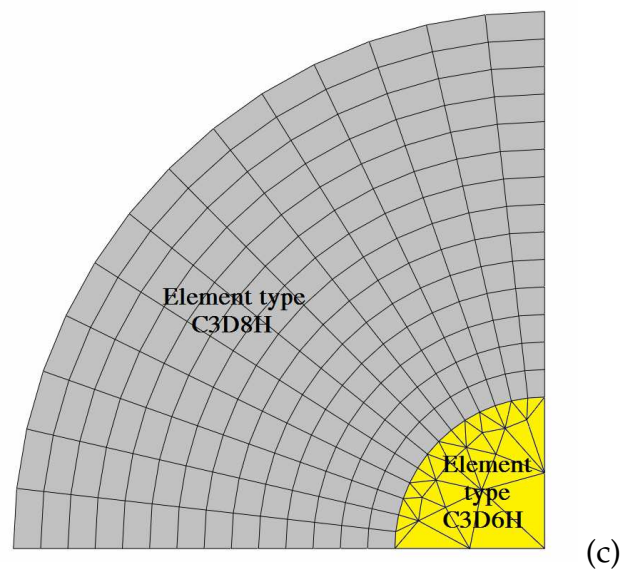


Figure 6.6: Configuration of the finite element mesh using 253 three-dimensional elements in the sheet quarter.

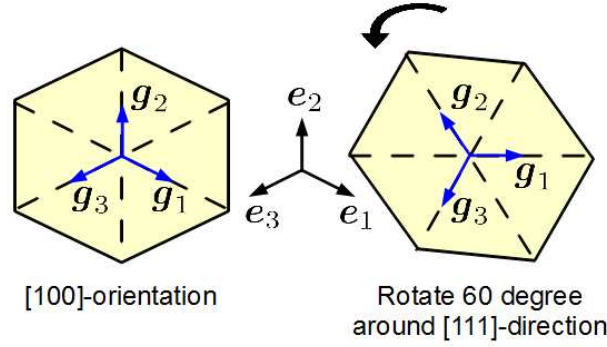


Figure 6.7: Orientations of two examined single crystal orientations.

is specified by the orthogonal tensor defined as follows

$$Q_{ij} = \begin{bmatrix} 1 & 0 & 0 \\ 0 & 1 & 0 \\ 0 & 0 & 1 \end{bmatrix}. \quad (6.1)$$

This means that no rotation exists between the sample coordinate system  $e_i$  and the crystal coordinate system  $g_i$ . The second single crystal orientation is obtained by rotating the crystal  $60^\circ$  around the  $[111]$ -direction. The orthogonal tensor is specified by

$$Q_{ij} = \frac{1}{3} \begin{bmatrix} 2 & -1 & 2 \\ 2 & 2 & -1 \\ -1 & 2 & 2 \end{bmatrix}. \quad (6.2)$$

The large strain single crystal plasticity model is applied at the integration points of the ABAQUS FE-model and accounts for plastic deformation by a combination of BCC slip system families  $\{110\}\langle 111 \rangle + \{112\}\langle 111 \rangle$ . The slip plane normal  $\tilde{n}_\alpha$  and the slip direction  $\tilde{d}_\alpha$  of the coupled BCC slip system are accounted for in the model by the Schmid tensors  $\tilde{M}_\alpha = \tilde{d}_\alpha \otimes \tilde{n}_\alpha$  ( $\alpha = 1 \dots 24$ ). The FE simulation of the deep drawing process is described in two main steps. In the first step, the quarter of sheet is pressed by a holder force. The sheet is pushed down subsequently into the lower die by the punch in the second step. Due to numerical problems, a low Coulomb coefficient of 0.05 is assumed in the numerical FE simulations of the aforementioned single crystal orientations. Figs. 6.8-6.9 show the results of the plastic strain rate and the form of ears in the sheet quarter for two different single crystal orientations. It can be seen that the earing profiles of two single crystal orientations are different. This shows that the deformation behavior of the polycrystalline sheet will be strongly influenced by the underlying single crystal orientations.

## Application of the Polycrystal Model for Metal Forming Operation

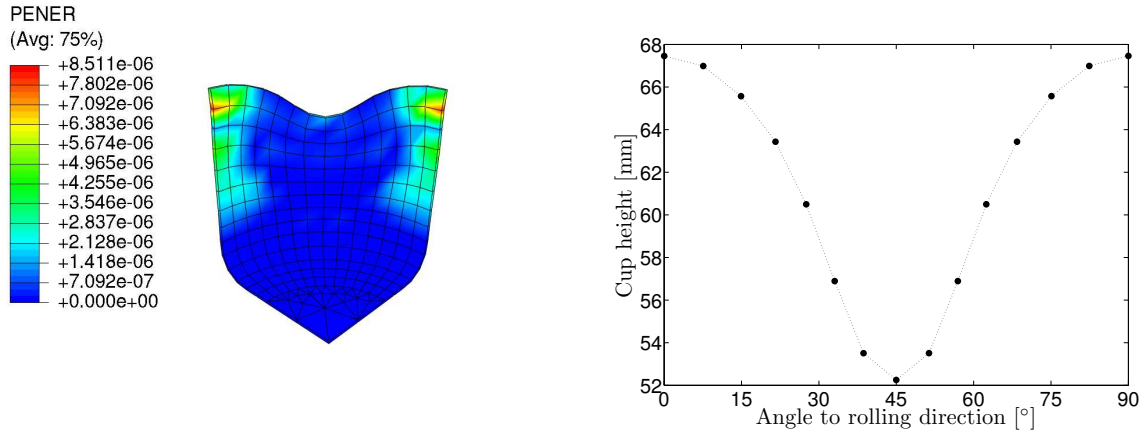


Figure 6.8: Numerical results obtained by using the standard crystal [100]-orientation: (left) plastic strain rate, PENER [ $s^{-1}$ ] and (right) earing profile of the sheet quarter in rolling direction.

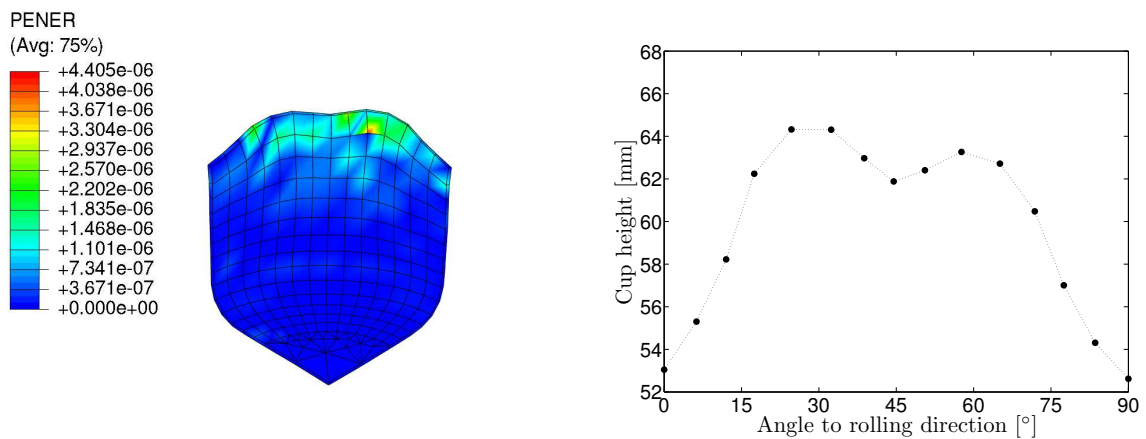


Figure 6.9: Numerical results obtained by using the single crystal orientation rotated  $60^\circ$  about [111]-direction: (left) plastic strain rate, PENER [ $s^{-1}$ ] and (right) earing profile of the sheet quarter in rolling direction.

## 6.2.2 Deep Drawing Simulation with Crystal Orientations extracted from EBSD Texture Data

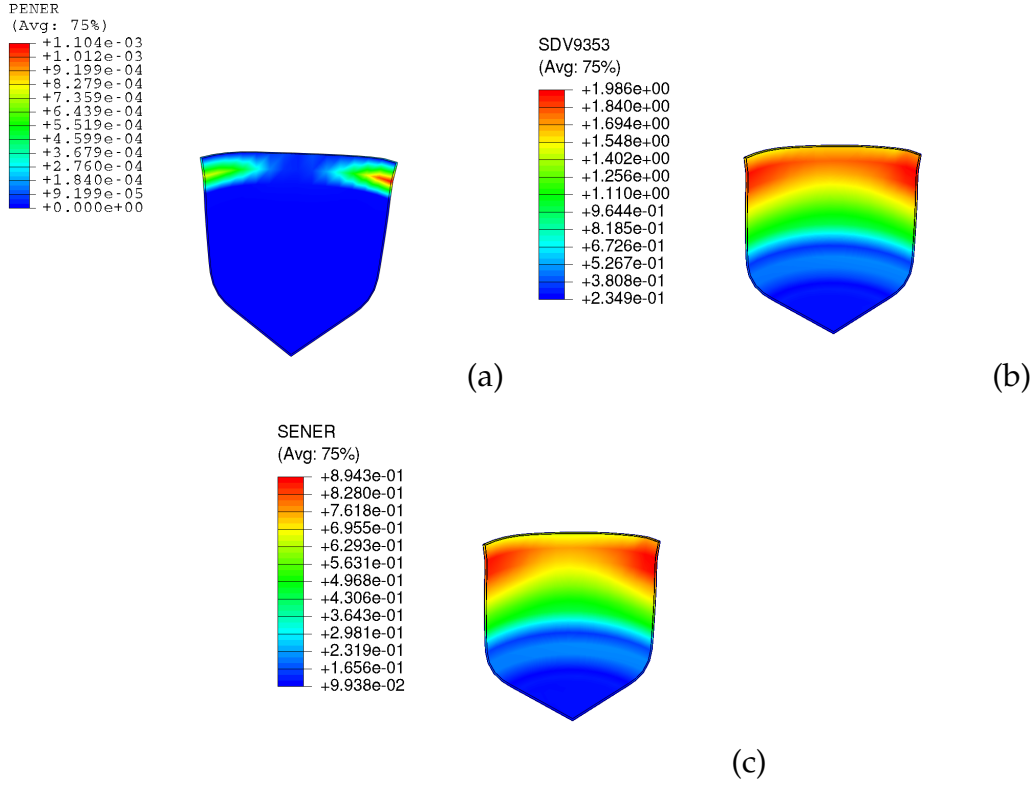


Figure 6.10: Numerical results obtained by using the orthotropic orientation data set of 200 original grains, (a) plastic strain rate [s<sup>-1</sup>], (b) accumulated plastic slip [-], and (c) plastic strain [-].

In order to study the crystallographic texture effects in the deep drawing simulation, the reduced orthotropic orientation data set of the heat treated DC04 steel is taken into account. The reduced orientation data set consisting of 200 grains, is extracted from the original orientation data set with 2554 grains (see Section 3.2.1, Chapter 3). The orthotropic orientation data of this reduced data, consisting of 800 (200 × 4 symmetry operations) single crystal orientations, is assigned to the integration points of the FE-model and proves to be sufficient to simulate the effect of the polycrystalline earing. During the numerical simulation, the accumulated plastic slip  $\gamma$  is computed by the sum of all slip rates  $\dot{\gamma}_\alpha$  ( $\alpha = 1 \dots 24$ ) over time

$$\gamma = \int_0^t \sum_{\alpha} |\dot{\gamma}_\alpha| dt. \quad (6.3)$$

The simulated results of the plastic strain rate, the accumulated plastic slip and plastic strain are shown in Fig. 6.10. The evolution of von Mises stress at different deformation

## Application of the Polycrystal Model for Metal Forming Operation

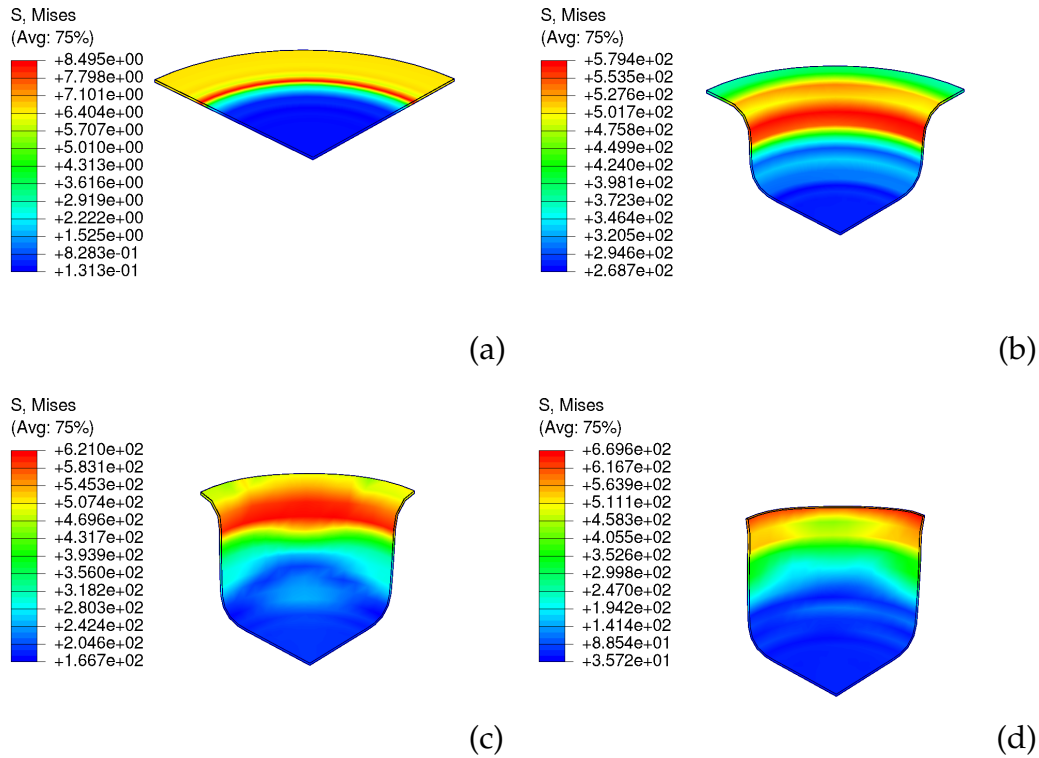


Figure 6.11: Evolution of von Mises stress [MPa] in deep drawing simulation by using the orthotropic orientation data of 200 original grains: (a) Compression step by holder force, (b)-(d) different deformation states.

states is represented in Fig. 6.11. A comparison between experimental earing profiles and numerical earing profiles is shown in Fig. 6.12. The predicted number of ears agrees well with the experimental result. A satisfactory agreement of the predicted cup deformation with the experimental result cannot be found for the friction coefficient in the measured range 0.08 – 0.12. Nevertheless, the magnitude of the calculated earing height agrees better to the experiment when the friction coefficient is decreased. The effect of the friction coefficients on the earing is significant for the specific range  $\mu = 0 - 0.06$  selected here. It can be seen that the numerical earing profile is in good agreement to the experiment for the friction coefficient approximately  $\mu = 0.04$ .

### 6.2.3 Deep Drawing Simulation with Texture Components

In this section, the low dimensional texture representation by the texture components, discussed in Section 3.3 (Chapter 3), is used to simulate the deep drawing process of the polycrystalline DC04 steel sheet. The influence of the dimensionality reduction of the orientation input data is verified by comparing the computed earing profile to the experimental results. The original heat treated orientation data including

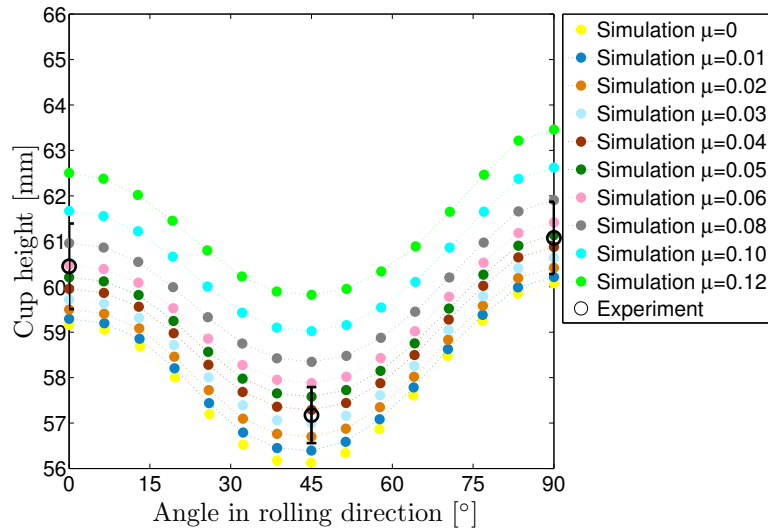


Figure 6.12: Comparison of earing profiles between experimental data and numerical results by using the orthotropic orientation data of 200 original grains for different friction coefficients  $\mu$ ; Mean value of experiments ( $\bigcirc$ ), standard deviation is indicated by the error bar  $\bar{I}$ .

2554 grains is reduced to 212 texture components in the fundamental zone. The orthotropic orientation data set, 848 ( $212 \times 4$  symmetry operations) single crystal orientations, is assigned to the integration points of the FE-models. Fig. 6.13 represents numerical results of the plastic strain rate, the accumulated plastic slip, and the accumulated plastic strain. Fig. 6.15 shows the evolution of the von Mises stress at different deformation states. The comparison between experimental earing profiles and numerical earing profiles for different friction coefficients is shown in Fig. 6.14. The magnitude of the numerical earing is quite similar to the one obtained from the aforementioned simulation using 800 single crystal orientations. The results show that the number of ears obtained in the numerical results and experimental results are in good agreement when considering a full sheet metal of DC04 steel.

## Application of the Polycrystal Model for Metal Forming Operation

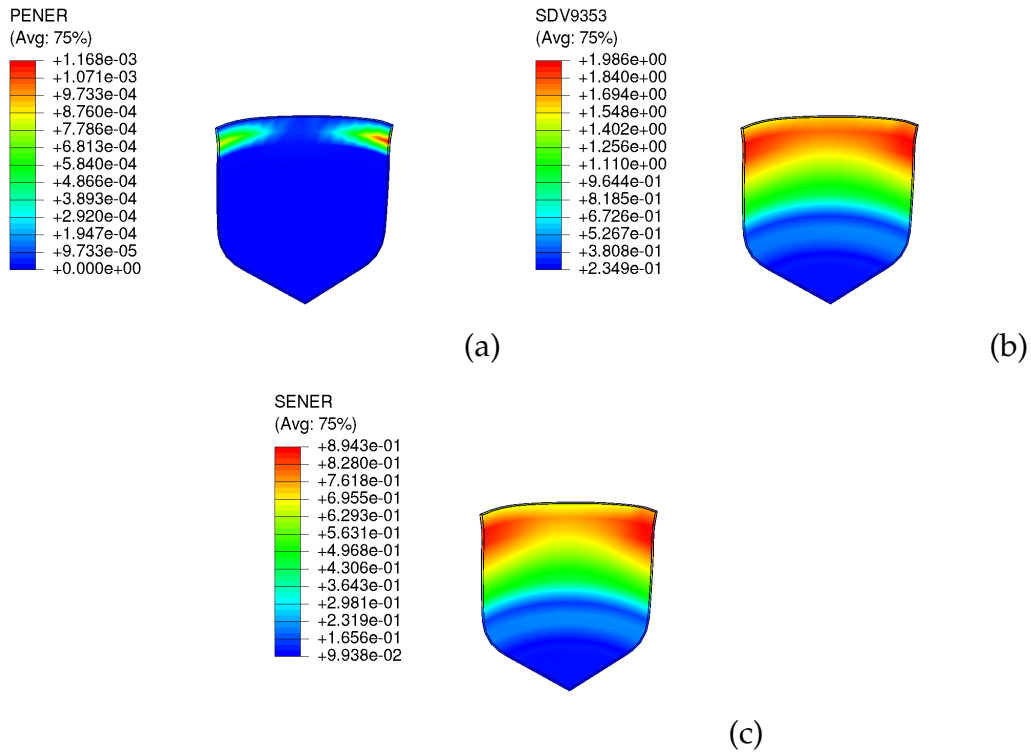


Figure 6.13: Numerical results obtained by using the orthotropic orientation data set of 212 texture components, (a) plastic strain rate  $[s^{-1}]$ , (b) accumulated plastic slip  $[-]$  and (c) accumulated plastic strain  $[-]$ .

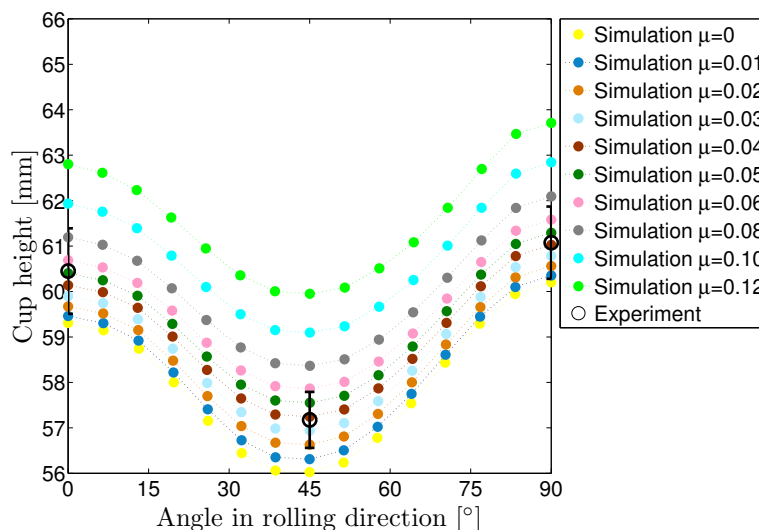


Figure 6.14: Comparison of earing profiles between experimental data and numerical results by using the orthotropic orientation data of 212 texture components for different friction coefficients  $\mu$ ; Mean value of experiments ( $\circ$ ), standard deviation is indicated by the error bar  $\bar{I}$ .

## Application of the Polycrystal Model for Metal Forming Operation

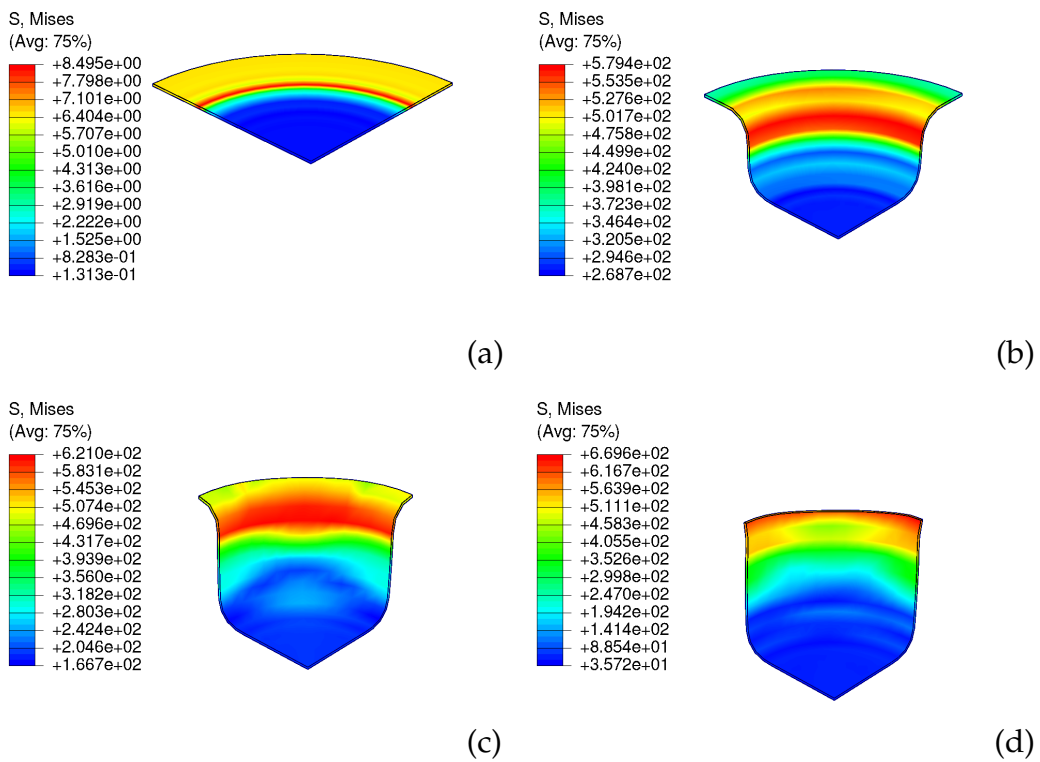


Figure 6.15: Evolution of von Mises stress [MPa] in deep drawing simulation by using the orthotropic orientation data of 212 texture components: (a) Compression step by holder force, (b)-(d) different deformation states.

# Chapter 7

## Texture-based Modeling of Strain Localization

### 7.1 Finite Element Approximation and Localization Criteria

In order to evaluate the formability of sheet metals, the prediction of forming limit diagrams (FLDs) is considered in the following. As proposed and investigated by several authors (Marniciak and Kuczynski, 1967; Janssens et al., 2001; Viatkina et al., 2005; Lang et al., 2005; Uthaisangasuk et al., 2007; Aretz, 2007; Verleysena et al., 2011; Volk and Hora, 2011), forming limit curves can be used to predict the localization behavior of metals in industrial manufacturing processes. For a given sheet material, the FLD is the curve representing the strains with localization in strain space using the major strain  $\varepsilon_1$  and the minor strain  $\varepsilon_2$ . Maximum values of  $\varepsilon_1$  and  $\varepsilon_2$  are determined by measuring principal strains at a failure state. As defined and illustrated in Fig. 7.1 (see, e.g., Keeler and Backofen (1963); Goodwin (1968) and Viatkina et al. (2005)), the FLDs separate the strain space in the safe and unsafe domains.

Hill (1952) proposed an analytical method by taking into account the strain instability of an initially homogeneous sheet metal. The zero extension criterion in the bifurcation analysis was developed to investigate the deep drawing range. Storen and Rice (1975) extended Hill's stability analysis in order to predict the onset of localized necking in thin sheets under biaxial stretching. Furthermore, the perturbation analyzes of Benallal and Tvergaard (1995) and Benallal et al. (2001) can be used to predict the localization behavior of rate-dependent materials phenomena. By Aretz (2007, 2010), the diffuse and localized necking models according to Hill (1952); Marniciak and Kuczynski (1967) are investigated within the framework of rigid-plastic and elastic-plastic constitutive models using various yield functions for plastic anisotropic material. These formability

models have been applied to different orthotropic sheet metals in order to predict FLDs of different types of aluminium alloys.

In this section, the prediction of FLD for a heat treated DC04 steel is performed by using a micromechanical model. Strain instabilities are analyzed based on FE simulations with real texture data. The heat treated texture data of the DC04 steel is used, e.g., an orthotropic texture data set composed of 800 grains (200 grains with orthotropic symmetry). The Taylor type polycrystal model is used for the scale transition. Crystal orientations of the orthotropic texture data are assigned to each integration point of the FE mesh (Phan et al., 2011b). The numerical FLD is compared to the experimental result provided by IFU (Stuttgart).

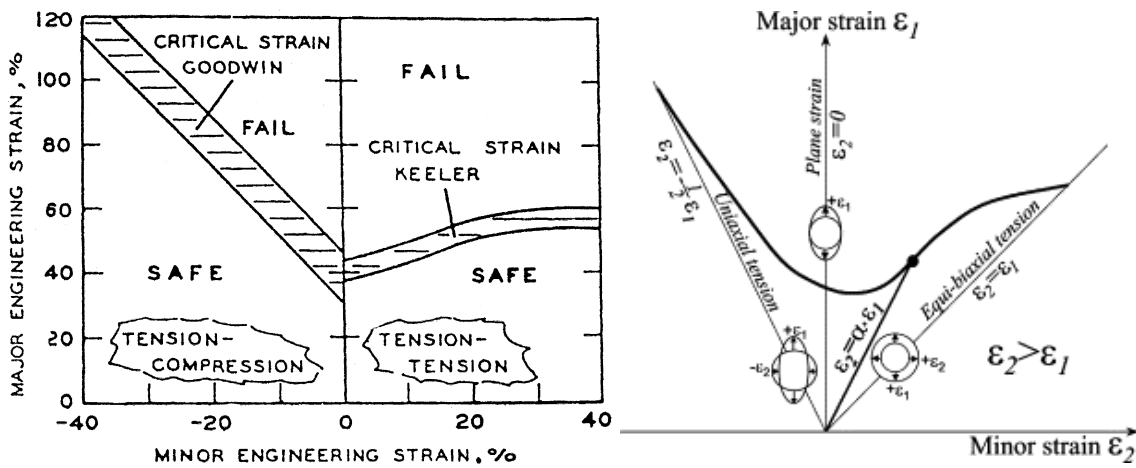


Figure 7.1: Forming limit diagrams (Keeler and Backofen, 1963; Goodwin, 1968; Viatkina et al., 2005).

One finite element model is used to determine the forming limit curve of the heat treated DC04 steel. A plane stress state is assumed. Two criteria are considered in the localization analysis to determine the FLD (see, e.g., Chapter 5, Marniciak et al. (2002)). In the positive minor strain region ( $\varepsilon_2 > 0$ ) of the FLD, the criterion based on the maximum stress power per unit volume is applied. This criterion corresponds to the maximum force criterion by Hill (1952). In the negative minor strain region ( $\varepsilon_2 < 0$ ), a criterion based on the maximum tension  $T$  (membrane stress) is applied. During the proportional loading paths, the following relation between the principal values of Hencky strain tensor  $\varepsilon^H = \ln U$  is assumed with  $\rho \in [-\frac{1}{2}, 1]$

$$\varepsilon_2^H = \rho \varepsilon_1^H. \quad (7.1)$$

The uniaxial tension, plane strain compression, and biaxial tension are represented by the values  $\rho = -1/2, 0$  and  $1$ , respectively.

The Hencky strain tensor is given by

$$\boldsymbol{\varepsilon}^H = \begin{bmatrix} \ln U_{11} & 0 & 0 \\ 0 & \rho \ln U_{22} & 0 \\ 0 & 0 & -(\rho + 1) \ln U_{33} \end{bmatrix} = \begin{bmatrix} \ln U & 0 & 0 \\ 0 & \rho \ln U & 0 \\ 0 & 0 & -(\rho + 1) \ln U \end{bmatrix}. \quad (7.2)$$

The  $\rho$ -values of  $-1/2$ ,  $0$ , and  $1$  correspond to tension, plane strain compression and biaxial tension. These different strain paths are illustrated in Fig. 7.2. The reference stretch rate is defined by

$$\dot{U}_0 = \frac{\sqrt{3}}{2} \frac{\dot{\varepsilon}_V}{\sqrt{\rho^2 + \rho + 1}}. \quad (7.3)$$

The time-dependent stretch in Eq. 7.2 is computed by

$$U = U_{11} = 1 + \dot{U}_0(\rho) t. \quad (7.4)$$

$\dot{\varepsilon}_V$  is set equal to  $10^{-3} \text{ s}^{-1}$ .

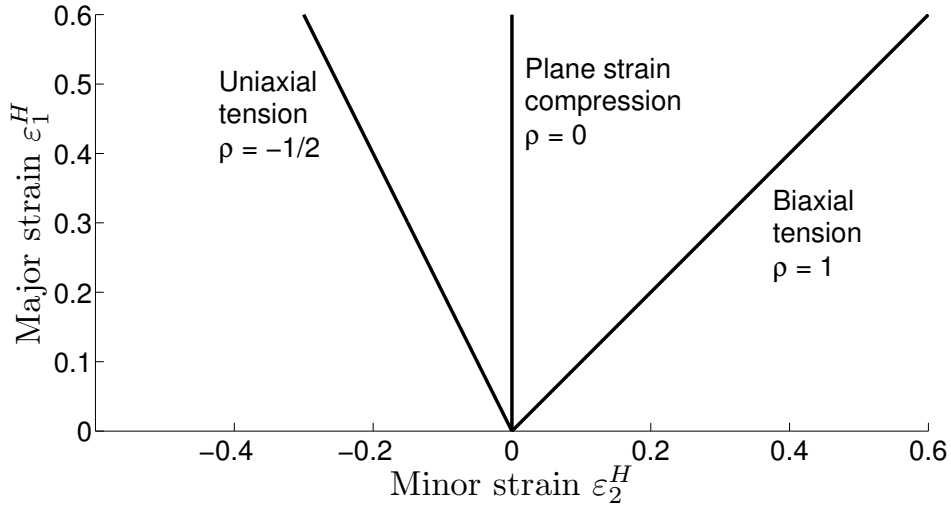


Figure 7.2: Interpretation of different strain paths depending on  $\rho$ .

The maximum principal force criterion (Hill, 1952) can be formulated as follows

$$P = T_{22}^{1PK} A_0 \rightarrow \text{Maximum}, \quad (7.5)$$

where the initial cross-sectional area  $A_0$  and the component  $T_{22}^{1PK} = \sigma_{22}/F_{22}$  of the first Piola-Kirchhoff stress tensor are used. The tensor  $\mathbf{T}^{1PK}$  is related to the Cauchy stress  $\boldsymbol{\sigma}$  and the deformation gradient  $\mathbf{F}$ , by  $\mathbf{T}^{1PK} = J \boldsymbol{\sigma} \mathbf{F}^{-T}$ , where  $J = \det(\mathbf{F})$ .

The maximum principal tension  $T$  criterion can be formulated as follows

$$T = \sigma_{22} h \rightarrow \text{Maximum}, \quad (7.6)$$

where  $h(t)$  is the current sheet thickness.

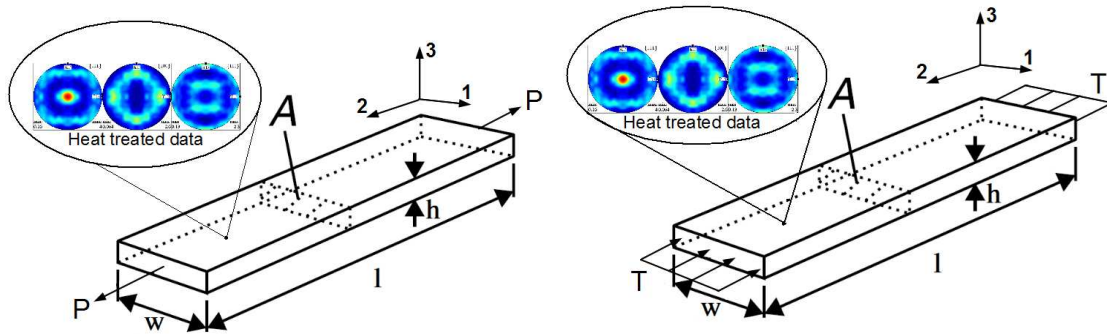
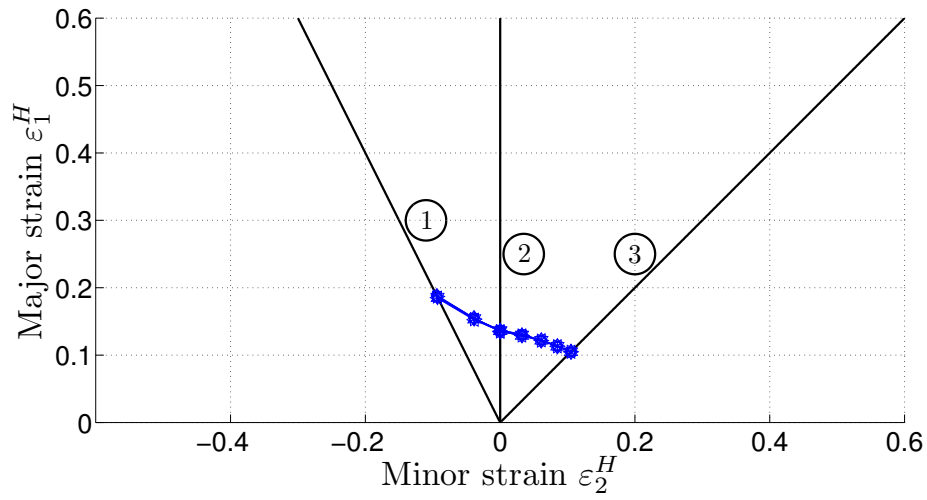


Figure 7.3: Localization analysis based on two criteria: (left) Criterion 1: Maximum principal force  $P$  and (right) Criterion 2: Maximum principal tension  $T$ .

## 7.2 Comparison between FE Simulations and Experiments

The FLD is determined by applying a Taylor type polycrystal model based on orthotropic heat treated texture data. The FE-model uses C3D8 type elements. The heat treated texture is taken into account as a natural microstructure imperfection in real metal. Fig. 7.3 represents stereographic pole figures of the orthotropic texture distribution given by 800 grains. The material parameters used for numerical calculations are given in Table 4.3 and correspond to the material parameters that have been identified based on tensile tests.

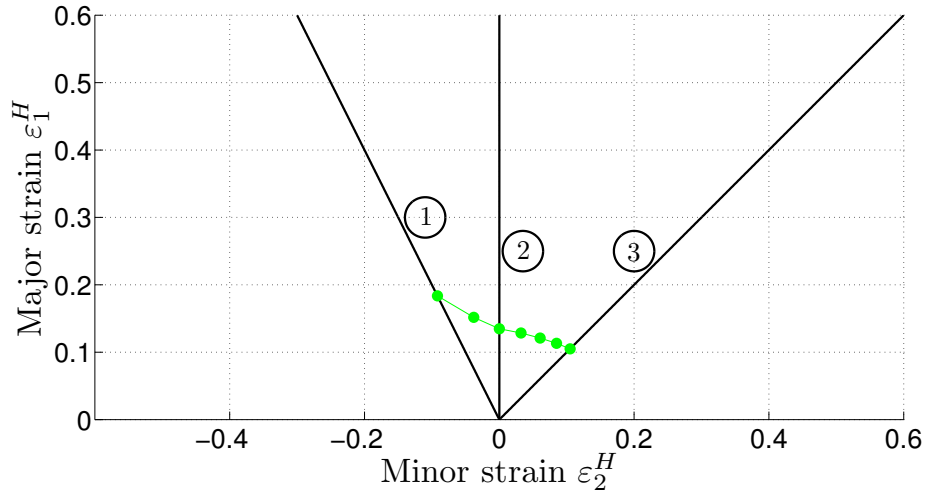
In order to analyze the initiation of deformation localization during proportional strain paths, different simulations are performed with strain ratios  $\rho \in [-1/2, 1]$ . By rotating the orthotropic texture  $0^\circ, 10^\circ, 20^\circ, 30^\circ, 40^\circ, 50^\circ, 60^\circ, 70^\circ, 80^\circ, 90^\circ$  about the normal direction (ND), 10 computed forming limit curves are obtained for each strain path. Each simulation of the rotated texture will give a FLD calculated for a fixed strain ratio  $\rho$ . All calculated simulations approximately reach an equivalent strain of 50%. Fig. 7.4 displays all forming limit curves calculated of different rotated texture data in the  $\varepsilon_1^H - \varepsilon_2^H$ . The FLD is obtained by representing the Hencky principal strain given by Eq. 7.2 corresponding to the maximum principal load  $P$  in the positive minor in-plane strain region (Criterion 1), and the maximum principal tension  $T$  in the negative minor in-plane strain region (Criterion 2). The lowest localization point for fixed  $\rho$  is shown in Fig. 7.5. By comparing the numerical results to the experimental mean FLD shown in Fig. 7.6, the critical strains are strongly underestimated. It can be seen that the numerical results agree better with experimental results in the negative minor strain region  $\varepsilon_2^H \in [-0.1, 0]$ . However, the computed results in the positive minor strain region show a qualitatively different behavior than the experimental one. The FLD



① Uniaxial tension ② Plane strain compression ③ Biaxial tension

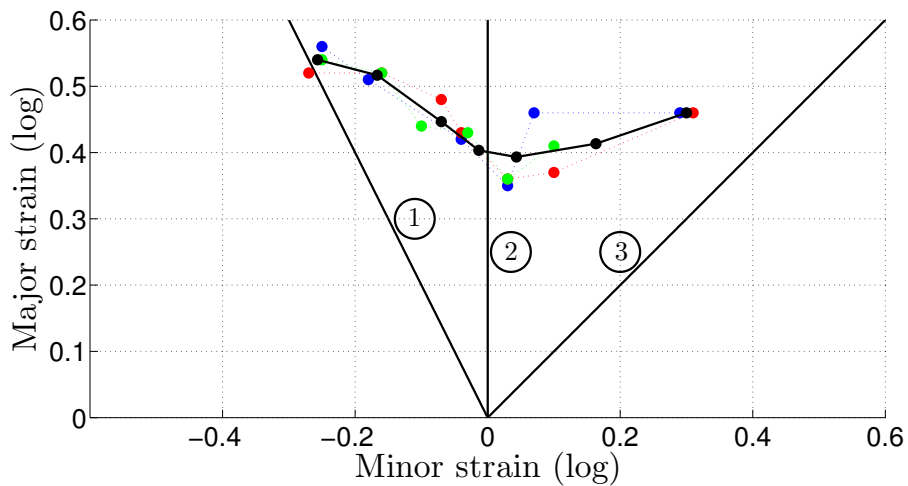
Figure 7.4: Forming limit curves calculated for DC04 steel with orthotropic texture data rotated by  $0^\circ$  ( $\times$ ),  $10^\circ$  ( $+$ ),  $20^\circ$  ( $\square$ ),  $30^\circ$  ( $\nabla$ ),  $40^\circ$  ( $\triangle$ ),  $50^\circ$  ( $\bullet$ ),  $60^\circ$  ( $\triangleleft$ ),  $70^\circ$  ( $\triangleright$ ),  $80^\circ$  ( $\diamond$ ),  $90^\circ$  ( $*$ ) to the rolling direction.

result obtained from the analysis of applied simple localization criteria corresponds to a conservative estimation of diffuse necking.



① Uniaxial tension ② Plane strain compression ③ Biaxial tension

Figure 7.5: Predicted lowest bound of FLD (●) for DC04 steel.



① Uniaxial tension ② Plane strain compression ③ Biaxial tension

Figure 7.6: Forming limit diagrams for the heat treated DC04 steel (experiment by IFU, Stuttgart), Experimental FLD 1 (●), Experimental FLD 2 (●), Experimental FLD 3 (●) and Experimental mean FLD (●).

# Chapter 8

## Summary

Several numerical results using a large strain single- and polycrystalline plasticity material model for a heat treated DC04 steel, based on micromechanical constitutive equations, have been presented in this thesis. The micromechanical model proved to be efficient and prospectively applicable in general in order to model the mesoscopic and the macroscopic mechanical behavior. The homogenization procedure yields a micro-macro transition from the microscopic level to the macroscopic level. This transition was implemented by means of user-defined subroutines in the commercial FE software package ABAQUS together with an implicit time integration procedure for the constitutive behavior of single crystals. This thesis illustrates how the real texture information can be incorporated into a continuum mechanical modeling.

The material parameters of the DC04 steel were identified for a large strain BCC crystal plasticity model based on experimental tensile tests. The material model was verified via full field FE simulations on the grain scale with real EBSD data for estimating the heterogeneity of the strain field and the reorientations of grains in a tensile test. The computed local grain reorientations were compared to experimental data at different states of elongation. By applying the Taylor type polycrystal model at the integration points, FE deep drawing simulations were performed based on real texture data. The computed earing profiles of these simulations were compared to the experimental data. The formability limit was analyzed for different strain paths based on the aforementioned polycrystal model accounting for the texture data of the heat treated DC04 steel at the integration points. The criterion delivers information about the onset of diffuse necking in the sheet metal. All simulations are based on the extended Kocks-Mecking hardening law, see e.g. (Böhlke et al., 2005), with a combination of two slip system families,  $\{110\}\langle 111 \rangle + \{112\}\langle 111 \rangle$  and show a good agreement with the experimental results.

The macroscopic material behaviour in tensile tests has been used to determine an optimal set of material parameters in the micromechanical model using the

reduced texture data of the heat treated DC04 steel. The single crystal orientations extracted from the 2D EBSD data of this steel have been used in the two-scale tensile test simulations. A comparison of the crystal plasticity FE simulation with the experimental tensile test for the uniaxial stress-strain curves has been presented. For that, experimental tensile tests of Project A6 and IUL (TU Dortmund) have been used. The material model parameters were identified alternatively based on uniaxial micro-pillar compression tests performed with single crystal columns of heat treated DC04 steel. Single crystal plasticity FE simulations of micro-pillar compression tests have been performed for a supposed non-zero Coulomb coefficient. These simulations were compared with experimental compression tests for stress-stretch and load-displacement curves to estimate the underlying material parameters. However, the material parameters determined by means of the pillar test cannot be used for the simulation of metal forming operation since the parameters reflect size effects on the microscale which are not relevant on the macroscale. For example, the hardening modulus is much too large if it is determined based on pillar simulations.

A verification of the material model has been carried out. Based on EBSD data, the grain-structure was modeled by a FE-model. The FE mesh has been imported into the ABAQUS/CAE software for the performance of the grain scale simulation. This FE simulation has been used for the identified DC04 steel material micro-parameters and two families of the BCC slip systems were assumed to possibly act simultaneously, namely  $\{110\}\langle 111 \rangle + \{112\}\langle 111 \rangle$ . In addition, a procedure for mapping the initial grain orientations into the fundamental zone has been implemented. The micromechanical behavior was analyzed in terms of the evolution of grain orientations. The grain orientations and reorientations are compared to the experiment for a group of grains. The numerical results of local grain reorientations seem to underestimate the heterogeneity compared to the experimental results. This issue can be probably explained by the neglect of the three-dimensional microstructure and interaction of the beneath microstructure in the 2D grain scale simulation. The influence of 3D interaction needs to be further investigated in further studies.

In the third step, a direct implementation of the Taylor-type polycrystal plasticity model at the integration points of finite elements in a deep drawing process is used to model the texture evolution and anisotropy in metal forming. The numerical results are validated by comparing numerical and experimental earing profiles. In particular, the crystallographic texture components being a reduced set of EBSD data is shown to be a prospectively efficient technique to predict anisotropic plasticity phenomena of textured polycrystalline materials in the metal forming operation. The numerical result proved that the earing profile and the effective height of a drawn cup can be predicted using a two-scale approach incorporating crystallographic texture data from experiments.

In the last step, a potential method to predict the FLD during sheet metal forming has been shown. The formability limit prediction has been presented for different strain paths using real texture data in Taylor-type simulations. In general, a satisfactory agreement of the FLD with the experimental data has not been found. The strain localization is strongly underestimated compared to the experimental data. However, it should be noted that the experimental data by IFU represent failure strains which correspond to strains that are much larger than the strains at diffuse necking. The FLD result obtained by the suggested scheme corresponds to a conservative estimation of diffuse necking.

# Appendix

## Rotational Symmetry Group of Cubic Lattice

Euler angles $\phi_1, \Phi, \phi_2$	Rotational matrices	Euler angles $\phi_1, \Phi, \phi_2$	Rotational matrices
$0, 0, 0$	$\begin{bmatrix} +1 & 0 & 0 \\ 0 & +1 & +1 \\ 0 & 0 & +1 \end{bmatrix}$	$0, \frac{\pi}{2}, 0$	$\begin{bmatrix} +1 & 0 & 0 \\ 0 & 0 & -1 \\ 0 & +1 & 0 \end{bmatrix}$
$0, \pi, 0$	$\begin{bmatrix} +1 & 0 & 0 \\ 0 & -1 & 0 \\ 0 & 0 & -1 \end{bmatrix}$	$\frac{\pi}{2}, \frac{\pi}{2}, \frac{3\pi}{2}$	$\begin{bmatrix} 0 & 0 & +1 \\ 0 & +1 & 0 \\ -1 & 0 & 0 \end{bmatrix}$
$\pi, \pi, 0$	$\begin{bmatrix} -1 & 0 & 0 \\ 0 & +1 & 0 \\ 0 & 0 & -1 \end{bmatrix}$	$\frac{\pi}{2}, 0, 0$	$\begin{bmatrix} 0 & -1 & 0 \\ +1 & 0 & 0 \\ 0 & 0 & +1 \end{bmatrix}$
$\pi, 0, 0$	$\begin{bmatrix} -1 & 0 & 0 \\ 0 & -1 & 0 \\ 0 & 0 & +1 \end{bmatrix}$	$\pi, \frac{\pi}{2}, \pi$	$\begin{bmatrix} +1 & 0 & 0 \\ 0 & 0 & +1 \\ 0 & -1 & 0 \end{bmatrix}$
$\frac{\pi}{2}, \frac{\pi}{2}, 0$	$\begin{bmatrix} 0 & 0 & +1 \\ +1 & 0 & 0 \\ 0 & +1 & 0 \end{bmatrix}$	$\frac{3\pi}{2}, \frac{\pi}{2}, \frac{\pi}{2}$	$\begin{bmatrix} 0 & 0 & +1 \\ 0 & +1 & 0 \\ +1 & 0 & 0 \end{bmatrix}$
$\frac{3\pi}{2}, \frac{\pi}{2}, \pi$	$\begin{bmatrix} 0 & 0 & -1 \\ +1 & 0 & 0 \\ 0 & -1 & 0 \end{bmatrix}$	$\frac{3\pi}{2}, 0, 0$	$\begin{bmatrix} 0 & +1 & 0 \\ 0 & 0 & -1 \\ -1 & 0 & 0 \end{bmatrix}$

Table 1: 24 elements of the rotational symmetry group of the cubic lattice (Part 1)

Euler angles $\phi_1, \Phi, \phi_2$	Rotational matrices	Euler angles $\phi_1, \Phi, \phi_2$	Rotational matrices
$\frac{3\pi}{2}, \frac{\pi}{2}, 0$	$\begin{bmatrix} 0 & 0 & -1 \\ -1 & 0 & 0 \\ 0 & +1 & 0 \end{bmatrix}$	$\frac{\pi}{2}, \pi, 0$	$\begin{bmatrix} 0 & +1 & 0 \\ +1 & 0 & 0 \\ 0 & 0 & -1 \end{bmatrix}$
$\frac{\pi}{2}, \frac{\pi}{2}, \pi$	$\begin{bmatrix} 0 & 0 & +1 \\ -1 & 0 & 0 \\ 0 & -1 & 0 \end{bmatrix}$	$\frac{3\pi}{2}, \pi, 0$	$\begin{bmatrix} 0 & -1 & 0 \\ -1 & 0 & 0 \\ 0 & 0 & -1 \end{bmatrix}$
$\pi, \frac{\pi}{2}, \frac{\pi}{2}$	$\begin{bmatrix} 0 & +1 & 0 \\ 0 & 0 & -1 \\ -1 & 0 & 0 \end{bmatrix}$	$\frac{\pi}{2}, \frac{\pi}{2}, \frac{\pi}{2}$	$\begin{bmatrix} 0 & 0 & +1 \\ 0 & -1 & 0 \\ +1 & 0 & 0 \end{bmatrix}$
$0, \frac{\pi}{2}, \frac{3\pi}{2}$	$\begin{bmatrix} 0 & +1 & 0 \\ 0 & 0 & -1 \\ -1 & 0 & 0 \end{bmatrix}$	$\pi, \frac{\pi}{2}, 0$	$\begin{bmatrix} -1 & 0 & 0 \\ 0 & 0 & +1 \\ 0 & +1 & 0 \end{bmatrix}$
$\pi, \frac{\pi}{2}, \frac{3\pi}{2}$	$\begin{bmatrix} 0 & -1 & 0 \\ 0 & 0 & +1 \\ -1 & 0 & 0 \end{bmatrix}$	$\frac{3\pi}{2}, \frac{\pi}{2}, \frac{3\pi}{2}$	$\begin{bmatrix} 0 & 0 & -1 \\ 0 & -1 & 0 \\ -1 & 0 & 0 \end{bmatrix}$
$0, \frac{\pi}{2}, \frac{\pi}{2}$	$\begin{bmatrix} 0 & -1 & 0 \\ 0 & 0 & -1 \\ +1 & 0 & 0 \end{bmatrix}$	$0, \frac{\pi}{2}, \pi$	$\begin{bmatrix} -1 & 0 & 0 \\ 0 & 0 & -1 \\ 0 & -1 & 0 \end{bmatrix}$

Table 2: 24 elements of the rotational symmetry group of the cubic lattice (Part 2)

# Bibliography

Abaqus/CAE, 2009. Abaqus/CAE User's Manual, 6.9.

Ahn, D., Joon, J., Kim, K., 2009. Modeling of anisotropic plastic behavior of ferritic stainless steel sheet. *International Journal of Mechanical Sciences* 51, 718–725.

Akarapu, S., Zbib, H. M., Bahr, D. F., 2010. Analysis of heterogeneous deformation and dislocation dynamics in single crystal micropillars under compression. *Plasticity* 26, 239–257.

Aretz, H., 2007. Numerical analysis of diffuse and localized necking in orthotropic sheet metals. *International Journal of Plasticity* 23, 798–840.

Aretz, H., 2010. An extension of Hill's localized necking model. *International Journal of Engineering Science* 48, 312–331.

Asaro, R. J., Needleman, A., 1985. Texture development and strain hardening in rate dependent polycrystals. *Acta Materialia* 33, 923–953.

Asaro, R. J., Rice, J. R., 1977. Strain localization in ductile single crystals. *Journal of Mechanics and Physics of Solids* 25, 309–338.

Bei, H., Shim, S., George, E. P., Miller, M. K., Herbert, E. G., Pharr, G. M., 2007. Compressive strengths of molybdenum alloy micro-pillars prepared using a new technique. *Scripta Materialia* 57, 397–400.

Benallal, A., Fudoli, C. A., Venturini, W. S., 2001. An implicit BEM formulation for gradient plasticity and localization phenomena. *International Journal for Numerical Methods in Engineering* 53, 1853–1869.

Benallal, A., Tvergaard, V., 1995. Nonlocal continuum effects on bifurcation in the plane strain tension–compression test. *Journal of the Mechanics and Physics of Solids* 43, 741–770.

Böhlke, T., 2000. *Crystallographic Texture Evolution and Elastic Anisotropy: Simulation, Modeling, and Application*. Shaker Verlag GmbH 2001, Germany.

- Böhlke, T., Glüge, R., Klöden, B., Skrotzki, W., Bertram, A., 2007. Finite element simulation of texture evolution and swift effect in NiAl under torsion. *Modelling Simulation Material Science Engineering* 15, 619–637.
- Böhlke, T., Risy, G., Bertram, A., 2005. A texture component model for anisotropic polycrystal plasticity. *Computational Material Science* 32, 284–293.
- Böhlke, T., Risy, G., Bertram, A., 2006. Finite element simulation of metal forming operations with texture based material models. *Modelling Simulation Material Science Engineering* 14, 365–387.
- Bradley, C. J., Cracknell, A. P., 1972. *The Mathematical Theory of Symmetry in Solids*. Oxford: Clarendon Press.
- Bronkhorst, C. A., Kalidindi, S. R., Anand, L., 1992. Polycrystalline plasticity and the evolution of crystallographic texture in FCC metals. *Philosophical Transactions of the Royal Society of London A* 341, 443–477.
- Bunge, H., 1982. *Texture Analysis and Materials Science*. London: Butterworths.
- Bunge, H., 1993. *Texture Analysis in Materials Science*. Culliver Verlag Göttingen.
- Bunge, H. J., 1987. *Quantitative texture analysis*. Dgm Metallurgy Information Germany.
- Cho, J., Rollett, A. D., Oh, K. H., 2005. Determination of a mean orientation in electron backscatter diffraction measurements. *Metallurgical and Materials Transactions A* 36A, 3427–3438.
- Cotterill, P., Mould, P. R., 1976. *Recrystallization and grain growth in metals*. Surrey University Press, London .
- Dawson, P. R., MacEwen, S. R., Wu, P.-D., 2004. Advances in sheet metal forming analyses: dealing with mechanical anisotropy from crystallographic texture. *Archives of Computational Methods in Engineering* 11 (No. 1), 3–96.
- Delannay, L., Béringhier, M., Chastel, Y., Logé, R., 2005. Simulation of cup-drawing based on crystal plasticity applied to reduced grain samplings. *Materials Science Forum* 495–497, 1639–1644.
- El-Awady, J. A., Wen, M., Ghoniem, N. M., 2009. The role of the weakest-link mechanism in controlling the plasticity of micropillars. *Mechanics and Physics of Solids* 57, 32–50.

- Gambin, W., 2001. *Plasticity and Textures*. Kluwer Academic Publishers, P.O. Box 17, 3300 AA Dordrecht, Netherlands.
- Gao, X., Przybyla, C. P., Adams, B. L., 2006. Methodology for recovering and analyzing two-point pair correlation functions in polycrystalline materials. *Metallurgical and Materials Transactions A* 37A, 2379–2387.
- Goodwin, G. M., 1968. Application of strain analysis to sheet metal forming problems in the press shop. *Society of Automotive Engineers* (No. 680093), 380–387.
- Gumbsch, P., 2003. Modeling strain hardening the hard way. *Science* Vol. 301 (No. 5641), 1857–1858.
- Gumbsch, P., 2005. An application oriented view on Materials Modeling, *Handbook of Materials Modeling* edited by S. Yip, pages 2713–2718. Springer Verlag, Netherlands.
- Habraken, A. M., 2004. Modelling the plastic anisotropy of metals. *Archives of Computational Methods in Engineering* 11 (No. 1), 3–96.
- Helm, D., Butz, A., Raabe, D., Gumbsch, P., 2011. Microstructure-based description of the deformation of metals: Theory and application. *Journal of the Minerals, Metals & Materials Society* 63 (No. 4), 26–33.
- Helming, K., 1996. *Texturapproximation durch Modellkomponenten*. Culliver Verlag Göttingen.
- Hielscher, R., 2010. MTEX Quantitative Texture Analysis Software. <http://code.google.com/p/mtex/>.
- Hill, R., 1952. On discontinuous plastic states with special reference to localised necking in thin sheet. *Journal of the Mechanics and Physics of Solids* , 19–30.
- Hosford, W. F., Caddell, R. M., 2007. *Metal Forming: Mechanics and Metallurgy*. United States of America by Cambridge University Press, New York.
- Humbert, M., Wagner, F., Esling, C., 1992. Numbering the crystallographic variants in phase transformation. *Journal of Applied Crystallography* 25, 724–730.
- Janssens, K., Lambert, F., Vanrostenberghe, S., Vermeulen, M., 2001. Statistical evaluation of the uncertainty of experimentally characterised forming limits of sheet steel. *Journal of Materials Processing Technology* 112, 174–184.
- Jöchen, K., Böhlke, T., 2010. Influence of the number of grains in a polycrystal on the prediction of texture during rolling by using the Taylor approach. *Proceedings in Applied Mathematics and Mechanics* 10, 415–416.

## BIBLIOGRAPHY

- Jöchen, K., Böhlke, T., 2011. Preprocessing of texture data for an efficient use in homogenization schemes. Proceedings of International Conference on Technology Plasticity (ICTP) , 848–853.
- Kanetake, N., Tozawa, Y., Yamamoto, S., 1985. Calculataion of earing in deep drawing for BCC metal sheets using texture data. International Journal of Mechanical Sciences 27 (No. 4), 249–256.
- Keeler, S. P., Backofen, W. A., 1963. Plastic instability and fracture in sheets stretched over rigid punches. Transactions of the American Society for Metals 56, 25–48.
- Kiener, D., Motz, C., Dehm, G., 2009. Micro-compression testing: A critical discussion of experimental constraints. Material Science and Engineering A 505, 79–87.
- Kocks, U., Mecking, H., 2003. Physics and phenomenology of strain hardening: the FCC case. Progress in Materials Science 48, 171–273.
- Lang, L., Danckert, J., Nielsen, K. B., 2005. Multi-layer sheet hydroforming: Experimental and numerical investigation into the very thin layer in the middle. Journal of Materials Processing Technology 170, 524–535.
- Lee, E. H., 1969. Elastic-plastic deformation at finite strains. Journal of Applied Mechanics 36, 1–6.
- Lege, D., Barlat, F., Brem, J., 1989. Characterization and modelling of the mechanical behavior and formability of a 2008-T4 sheet sample. International Journal of Mechanical Sciences 7 (No. 31), 549–563.
- Maitland, T., 2004. Electron Backscattered Diffraction: an EBSD system added to an SEM is a valuable new tool in the materials characterization. Advanced Materials and Processes , 34–36, HKL Technology Inc., 52 Federal Road, Unit 2D, Danbury, Connecticut.
- Maitland, T., Sitzman, S., 2006. Scanning Microscopy for Nanotechnology, Chap. 2: Electron Backscatter Diffraction (EBSD) Technique and Material Characterization Examples, pages 41–75. Springer Science.
- Marniciak, Z., Duncan, J. L., Hu, S. J., 2002. Mechanics of sheet metal forming. Butterworth-Heinemann.
- Marniciak, Z., Kuczynski, K., 1967. Limit strain in the processes of stretch-forming sheet metal. International Journal of Mechanical Sciences 9, 609–620, pergamon Press Ltd.

- Mathur, K., Dawson, P., 1989. On modeling the development of crystallographic texture in bulk forming processes. *International Journal of Plasticity* 5, 67–94.
- Miehe, C., Schröder, J., Schotte, J., 1999. Computational homogenization in finite plasticity. simulation of texture development in polycrystalline materials. *Computer Methods in Applied Mechanics and Engineering* 171, 387–418.
- Morawiec, A., 2003. A method of precise misorientation determination. *Journal of Applied Crystallography* 36, 1319–1323.
- Morawiec, A., 2004. *Orientations and Rotations*. Springer.
- Nakamachi, E., Xie, C. L., Harimoto, M., 2001. Drawability assessment of bcc steel sheet by using elastic/crystalline viscoplastic finite element analyses. *International Journal of Mechanical Sciences* 43, 631–652.
- Nemat-Nasser, S., 2002. *Experimentally-based micromechanical modeling of metal plasticity with homogenization from micro- to macro-scale properties*. Kluwer Academic Publishers, created in the United States of America.
- Paquin, A., Berbenni, S., Favier, V., Lemoine, X., Berveiller, M., 2001. Micromechanical modeling of the elastic-viscoplastic behavior of polycrystalline steels. *Plasticity* 17, 1267–1302.
- Phan, V. T., Jöchen, K., Böhlke, T., 2011a. Micromechanical modeling of metal forming operations. AIP (American Institute of Physics) Conference Proceedings 1353, 1215–1219, 14th International ESAFORM Conference on Material Forming: ESAFORM 2011, Belfast, UK, April 27-29 2011.
- Phan, V. T., Jöchen, K., Böhlke, T., 2011b. Micromechanical modelling for texture evolution and deformation localization in metal forming operations. submitted to *Proceedings of Summer School of Graduiertenkolleg 1483*.
- Phan, V. T., Jöchen, K., Böhlke, T., 2011c. Validation of material models on grain scale simulation based on EBSD data. *Proceedings in Applied Mathematics and Mechanics* 11, 543–544.
- Phan, V. T., Jöchen, K., Melcher, A., Böhlke, T., 2010. Deep drawing simulations based on microstructural data. *Proceedings in Applied Mathematics and Mechanics* 10 (No. 1), 69–70.
- Raabe, D., 1995. Simulation of rolling textures of b.c.c, metals considering grain interactions and crystallographic slip on 110, 112 and 123 planes. *Materials Science and Engineering A* 197, 31–37.

## BIBLIOGRAPHY

- Raabe, D., Klose, P., Engl, B., Imlau, K.-P., Friedel, F., Roters, F., 2002. Concepts for integrating plastic anisotropy into metal forming simulations. *Advances Engineering Materials* 4 (No. 4), 169–180.
- Raabe, D., Ma, D., Roters, F., 2007. Effects of initial orientation, sample geometry and friction on anisotropy and crystallographic orientation changes in single crystal microcompression deformation: A crystal plasticity finite element study. *Acta Materialia* 55, 4567–4583.
- Randle, V., 2000. *Electron Backscatter Diffraction in Material Science*. Kluwer Academic Publishers, New York.
- Roters, F., Eisenlohr, P., Hantcherli, L., Tjahjanto, D. D., Bieler, T. R., Raabe, D., 2010. Overview of constitutive laws, kinematics, homogenization and multiscale methods in crystal plasticity finite-element modeling: Theory, experiments, applications. *Acta Materialia* 58, 1152–1211.
- Schulze, V., Bertram, A., Böhlke, T., Krawietz, A., 2009. Texture-based modeling of sheet metal forming and springback. *Technische Mechanik Band 29, Heft 2*, 135–159.
- Schwartz, A. J., Kumar, M., Adams, B. L., Field, D. P., 2009. *Electron Backscatter Diffraction in Materials Science*. 2nd Edition, Springer Science+Business Media.
- Senger, J., Weygand, D., Gumbsch, P., Kraft, O., 2008. Discrete dislocation simulations of the plasticity of micro-pillars under uniaxial loading. *Scripta Materialia* 58, 587–590.
- Simpleware, 2000–2011. Simpleware: Converting 3D images into models. <http://www.simpleware.com/>.
- Storen, S., Rice, J. R., 1975. Localized necking in thin sheets. *Journal of the Mechanics and Physics of Solids* 23, 421–441.
- Sudook, A. K., Ward, L. J., 2007. Elastic constants and internal friction of martensitic steel, ferritic-pearlitic steel, and alpha-iron. *Material Science and Engineering A* 452-453, 633–639.
- Taylor, G., 1938. Plastic strain in metals. *J. Inst. Metals* 62, 307–324.
- U. F. Kocks, C. N. Tomé, H.-R. W., 2000. *Texture and Anisotropy: preferred orientations in polycrystals and their effect on materials properties*. Cambridge University Press.
- Uchic, M. D., Dimiduk, D. M., Florando, J. N., Nix, W. D., 2004. Sample dimensions influence strength and crystal plasticity. *Science* 305, 986–989.

- Uthaisangasuk, V., Prahl, U., Bleck, W., 2007. Stress based failure criterion for formability characterisation of metastable steels. *Computational Materials Science* 39, 43–48.
- Van Houtte, P., 1988. A comprehensive mathematical formulation of an extended Taylor-bishop-hill model featuring relaxed constraints, the Renouard-Winterberger theory and a strain rate sensitive model. *Textures and Microstructures* 8–9, 313–350.
- Verleysena, P., Peirsa, J., Slyckena, J. V., Faesb, K., Duchenec, L., 2011. Effect of strain rate on the forming behaviour of sheet metals. *Journal of Materials Processing Technology* 211, 1457–1464.
- Viatkina, E. M., Brekelmans, W. A. M., Geers, M. G. D., 2005. A crystal plasticity based estimate for forming limit diagrams from textural inhomogeneities. *Journal of Materials Processing Technology* 168, 211–218.
- Volk, W., Hora, P., 2011. New algorithm for a robust user-independent evaluation of beginning instability for the experimental FLC determination. *International Journal of Material Forming* 4, 339–346.
- Volkert, C. A., Lilleodden, E. T., 2006. Size effects in the deformation of sub-micron Au columns. *Philosophical Magazine* 86 (Nos. 33–35), 5567–5579.
- Wilbrandt, P.-J., 1985. New aspects of the recrystallization process. *Journal of Physics B* 35, 249–256.
- Xie, C. L., Nakamachi, E., 2002. Investigations of the formability of BCC steel sheets by using crystalline plasticity finite element analysis. *Materials and Design* 23, 59–68.
- Yalcinkaya, T., Brekelmans, W. A. M., Geers, M. G. D., 2008. BCC single crystal plasticity modeling and its experimental identification. *Modelling and Simulation in Materials Science and Engineering* 16 (No. 8), 085007.
- Yang, Y., Ye, J. C., Lu, J., Liu, F. X., Liaw, P. K., 2009. Effects of specimen geometry and base material on the mechanical behavior of focused-ion-beam-fabricated metallic-glass micropillars. *Acta Materialia* 57, 1613–1623.
- Zhao, Z., Roters, F., Mao, W., Raabe, D., 2001. Introduction of a texture component crystal plasticity finite element method for anisotropy simulations. *Advanced Engineering Materials* 3 (No. 12), 984–990.

# List of Figures

2.1	The deformation gradient $\mathbf{F}$ maps a material point $\mathbf{X}$ in the reference configuration $\Omega_0$ to $\bar{\mathbf{X}}$ in the intermediate configuration $\bar{\Omega}$ by $\mathbf{F}_p$ , and to $\mathbf{x}$ in the spatial configuration $\Omega$ by $\mathbf{F}_e$ . . . . .	12
2.2	BCC slip systems. . . . .	15
3.1	Definition of a crystal orientation by three Euler angles: (a) initial state, (b) angle $\phi_1$ , (c) angle $\Phi$ , and (d) angle $\phi_2$ . . . . .	19
3.2	Experimental set-up for EBSD measurements (provided by Project A6). . . . .	20
3.3	EBSD microstructural image of DC04 steel before tensile test (experiment by Project A6). . . . .	20
3.4	EBSD microstructural images of DC04 steel after tensile test (experiment by Project A6): (left) Image of the rough surface and (right) grains with different orientations. . . . .	22
3.5	Microstructural EBSD images of the heat treated DC04 steel. . . . .	25
3.6	Comparison between pole figures of 2554 grains (above) and 200 grains (below). . . . .	26
3.7	Crystallite orientation distribution function: (above) 2554 grains and (below) 200 grains. . . . .	27
3.8	Comparison between pole figures of 2554 grains (above), 200 grains (below) additionally assuming orthotropic sample symmetry. . . . .	28
3.9	Crystallite orientation distribution function: (above) 2554 grains, (below) 200 grains additionally assuming orthotropic sample symmetry. . . . .	29
3.10	Raw EBSD microstructural image of a heterogeneous sample cut parallel to rolling direction from a DC04 steel specimen at the initial state. . . . .	30
3.11	Microstructural images at the initial state. . . . .	30
3.12	Identification and numbering of 574 grains in the microstructural image of clustered data set at the initial state. . . . .	33

## LIST OF FIGURES

3.13	Microstructural images of raw EBSD data sets (experiment by Project A6, GRK1483) at different states. . . . .	36
3.14	The cubic fundamental zone in the conventional Euler space (Gao et al., 2006). . . . .	37
3.15	Reduced heat treated data set using $\mathcal{K} = 3$ , represented by the fundamental zone partitioned by 216 boxes in 3D space, the unit of Euler angles [radian]. . . . .	37
3.16	Comparison between pole figures of (a) 2554 grains, (b) 200 grains and (c) 212 texture components. . . . .	38
3.17	Comparison between pole figures of (a) 2554 grains, (b) 200 grains, (c) 212 texture components additionally assuming orthotropic sample symmetry. . . . .	39
4.1	(left) Tensile specimen at different angles to RD and (right) experimental stress-strain curves for different angles to RD (experiment by Project A6) - $0^\circ, 45^\circ, 90^\circ$ to RD. . . . .	41
4.2	Uniaxial tensile stress-strain curves for specimen oriented at different angles to RD (experiment by IUL, Technical University of Dortmund): (a) $0^\circ$ , (b) $15^\circ$ , (c) $30^\circ$ , (d) $45^\circ$ , (e) $60^\circ$ , (f) $75^\circ$ , (g) $90^\circ$ . . . . .	42
4.3	FE-model of the uniaxial tensile test with one finite element. . . . .	43
4.4	Curves of tensile test experiments given by Project A6 (left) and simulations with $\{110\}\langle 111 \rangle + \{112\}\langle 111 \rangle$ slip systems (right). . . . .	45
4.5	Numerically determined stress-strain curves with the optimal set of material parameters in comparison to experimental stress-strain curves (Project A6) for different angles to RD - (a) $0^\circ$ , (b) $90^\circ$ , (c) $45^\circ$ . . . . .	45
4.6	Numerically determined stress-strain curves in comparison to experimental data of IUL (TU Dortmund) for different angles to RD - (a) $0^\circ$ , (b) $15^\circ$ , (c) $30^\circ$ , (d) $45^\circ$ , (e) $60^\circ$ , (f) $75^\circ$ , (g) $90^\circ$ . . . . .	46
4.7	Mechanical behavior for pure Ni micro-samples having a $\langle 134 \rangle$ -orientation, (a) stress-strain curves for micro-samples having different diameters, as well as the stress-strain curve for a bulk single crystal, (b) a scanning electron micrograph (SEM) image of a micro-sample tested to 4 strains, and (c) a SEM image of a micro-sample after testing (Uchic et al., 2004). . . . .	48
4.8	(a) Some differently sized Cu samples fabricated into a bulk single crystal, (b) two Cu samples with a thick TiN coating on top, (c) a cylindrical Cu pillar fabricated, and (d) a Cu specimen on top of an etched needle (Kiener et al., 2009). . . . .	49

## LIST OF FIGURES

4.9	Geometry of micro-pillar column 1 (experiment by Project A6). . . . .	50
4.10	Geometry of micro-pillar column 2 (experiment by Project A6). . . . .	50
4.11	Mechanical boundary conditions of micro-pillar test and FE mesh of micropillar and underlying material. . . . .	51
4.12	The von-Mises stress field [MPa] in deformed configuration of micro-pillar column 1 under different viewpoints. . . . .	51
4.13	The von-Mises stress field [MPa] in deformed configuration of micro-pillar column 2 under different viewpoints. . . . .	52
4.14	Plastic strain rate (PENER [s <sup>-1</sup> ]) of column 1 at two different steps: the end of compression step (left) and the end of creep step (right). . . . .	52
4.15	Plastic strain rate (PENER [s <sup>-1</sup> ]) of column 2 at two different steps: the end of compression step (left) and the end of creep step (right). . . . .	53
4.16	Comparison of the numerical and experimental load-displacement curves for micro-pillar column 1 (left) and micro-pillar column 2 (right). . . . .	54
4.17	Comparison of the numerical and experimental displacement-time curves for micro-pillar column 1 (left) and micro-pillar column 2 (right). . . . .	54
4.18	Comparison of the numerical and experimental load-time curves for micro-pillar column 1 (left) and micro-pillar column 2 (right). . . . .	55
4.19	Comparison of the numerical and experimental stress-stretch curves for micro-pillar column 1 (left) and micro-pillar column 2 (right). . . . .	55
5.1	(left) Microstructure of heat treated DC04 steel at the initial state obtained from the clustering process by MTEX toolbox and (right) complete grains constructed by the Simpleware software. . . . .	57
5.2	FE-mesh of the microstructure at the initial state. . . . .	58
5.3	(left) Location of 3 selected local grains in the microstructural image and (right) enlargement of 3 local grains: #296, #345 and #357. . . . .	58
5.4	Initial grain orientations in the 3D (left) and 2D fundamental zone $\phi_2 - \Phi$ (right). . . . .	59
5.5	Initial Euler angle distribution [°] in the FE simulation: (a) angle $\phi_1$ , (b) angle $\Phi$ and (c) angle $\phi_2$ in the fundamental zone. . . . .	60
5.6	Initial Euler angles [°] of 3 local grains in the FE simulation: (a) angle $\phi_1$ , (b) angle $\Phi$ and (c) angle $\phi_2$ in the fundamental zone. . . . .	61
5.7	Distribution of critical resolved shear stress [MPa] of the grain structure at the different states: (a) 5%, (b) 10%, (c) 15% and (d) 20% elongation. . . . .	62
5.8	Plastic slip on 12 slip systems $\{110\}\langle 111 \rangle$ at 20% elongation, the unit is [s <sup>-1</sup> ]. . . . .	63

## LIST OF FIGURES

5.9	Plastic slip of 12 slip systems $\{112\}\langle 111 \rangle$ at 20% elongation, the unit is $[s^{-1}]$ . . . . .	64
5.10	Microstructural images of local grains at different states. . . . .	65
5.11	Comparison of Euler angles $[\circ]$ between the experiment (left) and numerical results (right) at the state of 5% elongation: (a)–(b) angle $\phi_1$ , (c)–(d) angle $\Phi$ , (e)–(f) angle $\phi_2$ . . . . .	67
5.12	Comparison of Euler angles $[\circ]$ between the experiment (left) and numerical results (right) at the state of 10% elongation: (a)–(b) angle $\phi_1$ , (c)–(d) angle $\Phi$ , (e)–(f) angle $\phi_2$ . . . . .	68
5.13	Comparison of Euler angles $[\circ]$ between the experiment (left) and numerical results (right) at the state of 15% elongation: (a)–(b) angle $\phi_1$ , (c)–(d) angle $\Phi$ , (e)–(f) angle $\phi_2$ . . . . .	69
5.14	Comparison of Euler angles $[\circ]$ between the experiment (left) and numerical results (right) at the state of 20% elongation: (a)–(b) angle $\phi_1$ , (c)–(d) angle $\Phi$ , (e)–(f) angle $\phi_2$ . . . . .	70
5.15	Comparison of reorientation $[\circ]$ between the experiment (left) and numerical results (right) at different states: (a)–(b) 5%, (c)–(d) 10%, (e)–(f) 15%, (g)–(h) 20% elongation. . . . .	71
6.1	Experimental deep drawing tool set-up and some products (IFU, Stuttgart). . . . .	72
6.2	(a) Illustration of two important regions in the deep drawing process and (b) the characteristics of earing profile in a quarter of the drawn cup. . . . .	73
6.3	(left) Tool geometry and set-up for deep drawing process and (right) earing profiles obtained from deep drawing process in experiments (IFU, University of Stuttgart). . . . .	74
6.4	The deformed cups of 3 experiments: (a)–(b) Experiment 1, (c)–(d) Experiment 2, (e)–(f) Experiment 3 (experiment by IFU (University of Stuttgart)). . . . .	75
6.5	FE deep drawing simulation set-up of a sheet quarter. . . . .	76
6.6	Configuration of the finite element mesh using 253 three-dimensional elements in the sheet quarter. . . . .	76
6.7	Orientations of two examined single crystal orientations. . . . .	77
6.8	Numerical results obtained by using the standard crystal $[100]$ -orientation: (left) plastic strain rate, PENER $[s^{-1}]$ and (right) earing profile of the sheet quarter in rolling direction. . . . .	78

## LIST OF FIGURES

6.9	Numerical results obtained by using the single crystal orientation rotated $60^\circ$ about [111]-direction: (left) plastic strain rate, PENER [ $s^{-1}$ ] and (right) earing profile of the sheet quarter in rolling direction. . . . .	78
6.10	Numerical results obtained by using the orthotropic orientation data set of 200 original grains, (a) plastic strain rate [ $s^{-1}$ ], (b) accumulated plastic slip [-], and (c) plastic strain [-]. . . . .	79
6.11	Evolution of von Mises stress [MPa] in deep drawing simulation by using the orthotropic orientation data of 200 original grains: (a) Compression step by holder force, (b)-(d) different deformation states. .	80
6.12	Comparison of earing profiles between experimental data and numerical results by using the orthotropic orientation data of 200 original grains for different friction coefficients $\mu$ ; Mean value of experiments ( $\circ$ ), standard deviation is indicated by the error bar $\bar{I}$ . . . .	81
6.13	Numerical results obtained by using the orthotropic orientation data set of 212 texture components, (a) plastic strain rate [ $s^{-1}$ ], (b) accumulated plastic slip [-] and (c) accumulated plastic strain [-]. . . . .	82
6.14	Comparison of earing profiles between experimental data and numerical results by using the orthotropic orientation data of 212 texture components for different friction coefficients $\mu$ ; Mean value of experiments ( $\circ$ ), standard deviation is indicated by the error bar $\bar{I}$ . . . .	82
6.15	Evolution of von Mises stress [MPa] in deep drawing simulation by using the orthotropic orientation data of 212 texture components: (a) Compression step by holder force, (b)-(d) different deformation states. .	83
7.1	Forming limit diagrams (Keeler and Backofen, 1963; Goodwin, 1968; Viatkina et al., 2005). . . . .	85
7.2	Interpretation of different strain paths depending on $\rho$ . . . . .	86
7.3	Localization analysis based on two criteria: (left) Criterion 1: Maximum principal force $P$ and (right) Criterion 2: Maximum principal tension $T$ . . . . .	87
7.4	Forming limit curves calculated for DC04 steel with orthotropic texture data rotated by $0^\circ$ ( $\times$ ), $10^\circ$ ( $+$ ), $20^\circ$ ( $\square$ ), $30^\circ$ ( $\nabla$ ), $40^\circ$ ( $\triangle$ ), $50^\circ$ ( $\bullet$ ), $60^\circ$ ( $\triangleleft$ ), $70^\circ$ ( $\triangleright$ ), $80^\circ$ ( $\diamond$ ), $90^\circ$ ( $*$ ) to the rolling direction. . . . .	88
7.5	Predicted lowest bound of FLD ( $\bullet$ ) for DC04 steel. . . . .	89
7.6	Forming limit diagrams for the heat treated DC04 steel (experiment by IFU, Stuttgart), Experimental FLD 1 ( $\bullet$ ), Experimental FLD 2 ( $\bullet$ ), Experimental FLD 3 ( $\bullet$ ) and Experimental mean FLD ( $\bullet$ ). . . . .	89

# List of Tables

2.1	12 BCC slip systems of $\{110\}\langle 111 \rangle$ (Paquin et al., 2001). . . . .	16
2.2	12 BCC slip systems of $\{112\}\langle 111 \rangle$ (Yalcinkaya et al., 2008). . . . .	16
2.3	24 BCC slip systems of $\{123\}\langle 111 \rangle$ (Nemat-Nasser, 2002). . . . .	16
3.1	The EBSD data set of the tensile experiment before tensile test including 22641 rows and 12 columns (experiment by Project A6). . . . .	21
3.2	File format of the EBSD data set of the heat treated DC04 steel sample (experiment by Project A6). . . . .	23
3.3	The data set for identification of grains in the clustered heat treated specimen of DC04 steel. . . . .	24
3.4	File format of the raw EBSD data set of the experimental sample at the initial state including 105000 rows and 7 columns (experiment by Project A6). . . . .	31
3.5	The clustered EBSD data set (without erroneous measurement points) of the experimental sample at the initial state, including 103671 rows and 6 columns. . . . .	32
4.1	Set of material parameters based on the experimental tensile tests of Project A6. . . . .	44
4.2	Modeled hardening parameters based on the experimental tensile tests of IUL (Dortmund). . . . .	47
4.3	A mean set of hardening parameters. . . . .	47
4.4	Micro-pillar orientations (experiment by Project A6). . . . .	49
4.5	Estimated material parameters based on the experimental micro-pillar compression tests of Project A6. . . . .	55
1	24 elements of the rotational symmetry group of the cubic lattice (Part 1)	93
2	24 elements of the rotational symmetry group of the cubic lattice (Part 2)	94